3-2021

A Reduced Order Model of The Celestial Icosahedron As The Substructure For a Lighter Than Air Vehicle

Torin C. Quick

A REDUCED ORDER MODEL OF THE CELESTIAL ICOSAHEDRON AS THE SUBSTRUCTURE FOR A LIGHTER THAN AIR VEHICLE

THESIS

Torin C. Quick, Captain, USAF

AFIT-ENY-MS-21-M-314

DEPARTMENT OF THE AIR FORCE
AIR UNIVERSITY

AIR FORCE INSTITUTE OF TECHNOLOGY

Wright-Patterson Air Force Base, Ohio

AFIT-ENY-MS-21-M-314

A FINITE ELEMENT APPROACH TO A REDUCED ORDER MODEL OF THE CELESTIAL ICOSAHEDRON AS THE SUBSTRUCTURE FOR A VACUUM LIGHTER THAN AIR VEHICLE

THESIS

Presented to the Faculty

Department of Aeronautics and Astronautics

Graduate School of Engineering and Management

Air Force Institute of Technology

Air University

Air Education and Training Command

In Partial Fulfillment of the Requirements for the

Degree of Master of Science in Aeronautical Engineering

Torin C. Quick, B.S. ME

Captain, USAF

February 2021

AFIT-ENY-MS-21-M-314

A FINITE ELEMENT APPROACH TO A REDUCED ORDER MODEL OF THE CELESTIAL ICOSAHEDRON AS THE SUBSTRUCTURE FOR A VACUUM LIGHTER THAN AIR VEHICLE

Torin C. Quick, BS

Captain, USAF

Committee Membership:

Dr. A. N. Palazotto, PhD
Chair

R. A. Kemnitz, Maj, PhD
Member

J. Brewer, Maj, PhD
Member

AFIT-ENY-MS-21-M-314

Abstract

In the pursuit of producing a vacuum lighter-than-air vehicle of the form skin-over-substructure of the celestial icosahedron shape, a finite element approach was used to investigate a novel reduced order model to determine the minimum structure dimensionality to support the load of vacuum. This modeling technique represented the individual segments of the substructure as curved beams with clamped radially-resisted boundary conditions. The load profiles for the model were developed using a finite element model of a simply supported characteristic triangle surface with a sea level pressure applied. A vector projection was done on the boundary reaction forces of the triangle to determine the forces transferred to the structure in the radial direction only. The full structure was then modeled as a bare structure and structure with skin to validate the results of the reduced order model. The beam geometry for the material Ultem 9085 was determined through this process. The structure was 3-D printed with a Fortus 450mc. The 3-D printed structure was then experimentally tested under uniaxial compression complimented with a FEA model to serve as a basis for validating the model's ability to predict the structure's behavior.

Acknowledgments

I would like to acknowledge my advisor Dr. Palazotto for his guidance and insight into the research that I conducted. He continually pushed me to explore new theories and hypotheses. Along the way I had to learn how to accurately explain my purpose and actions.

Special thanks to Travis Shelton who set up the 3D printing machines and identified the ideal support material configuration that resulted in excellent print quality specimen for experimental testing. I would also like to thank Maj Ryan Kemnitz and Mike Ranft for their assistance in setting up and running the experiments with the MTS machine.

Table of Contents

Contents

Page

Abstract i

Table of Contents iii

List of Figures vi

List of Tables x

1. Introduction 1

1.1. Overview 1

1.2. Objectives 3

1.3. Motivation 4

1.4. Prior Research 6

1.5. Current Research Implications 12

2. Research Methodology 14

2.1. Chapter Overview 14

2.2. Reduced Order Modeling Theory 15

2.2.1. Finite Element Analysis for the Reduced Order Model 18

2.2.2. Boundary Condition Spring Constants 19

2.2.3. Load Profile Determination 26

2.2.4. Beam Geometry and ROM Process 52

2.2.5. Beam Buckling Analysis 57

2.3. Finite Element Analysis for Full Celestial Icosahedron Modeling 58

2.3.1. FEA of Bare Frame Celestial Icosahedron 59

2.3.1. FEA of Celestial Icosahedron and Skin 61

2.3.2. FEA of the Celestial Icosahedron for Compression Testing 63

2.4. Additive Manufacturing 67
2.5. Mechanical Testing of the 3-D Printed Frame 72
2.6. Summary 74
3. Results and Discussion 76
3.1. Chapter Overview 76
3.2. Results of the ROM Technique 76
3.2.1. ROM Results for Load Profile 1 76
3.2.2. ROM Results for Load Profile 2 79
3.3. Results of the Full Celestial Models 81
3.3.1. Full Celestial Models without Skin 82
3.3.2. Full Celestial Models with the Skin 87
3.3.3. ROM Modifications 95
3.4. Mechanical Testing Results 101
3.5. Celestial Icosahedron Compression Modeling 106
3.5.1. Analytical Results Compared to Experimental Results 109
3.5.2. Compression Model with Skin 118
3.6. Summary 123
4. Conclusions and Recommendations 123
4.1. Chapter Overview 123
4.2. Conclusions of Research 124
4.3. Recommendations for Future Research 125
Appendix A: Vector Summed Nodal Reaction Forces vs Nodal Reaction Force Magnitudes 126

Bibliography 128

List of Figures

Page

Figure 1: Celestial Icosahedron 3

Figure 2: Buckled Copper Sphere Under Vacuum [7] 6

Figure 3: Simple Icosahedron Geodesic Shape [9] 8

Figure 4: Experimental Results vs Published Properties for Ultem 9085 [14] 12

Figure 5: Celestial Icosahedron Characteristic Triangle 16

Figure 6: Clamped-Radially Guided BC from Pilkey [23 17

Figure 7: Reduced Order Model Configuration 18

Figure 8: Individual Member Example 21

Figure 9: 4-Ring Intersection Isolation Process 21

Figure 10: Single Member Models for Stiffness Determination 22

Figure 11: Four 2-Segment Arches Identified 24

Figure 12: Example Schematics of 2-Segment Arches, A-A (top), A-C (bottom) 25

Figure 13: Geometric Load Distribution (top) and Greenoe's Model's Loads and BCs (bottom)[14] 28

Figure 14: Load Distribution Orientations for Each Segment 31

Figure 15: Nodal Reaction Forces of Method 1 Load Profile 31

Figure 16: Discrete Load Profiles and Polynomial Fits for Method 1 32

Figure 17: Schematic of Radial Loading Method 33

Figure 18: Superposition of Pressure Loads, Planar Face (left), Curved Face (right) 35

Figure 19: Adjacent Face Vector Representation 36

Figure 20: Snapping Schematic 38
Figure 21: Mesh for Load Profile Method 2 39
Figure 22: Vector Projection Schematic 40
Figure 23: Nodal Reaction Forces of Method 2 Load Profile 41
Figure 24: Discrete Load Profiles and Polynomial Fits for Method 2 42
Figure 25: Deformed State of Flexible Triangle with Wrinkles 43
Figure 26: Combined Load Profiles, Segments A (top), B (middle), and C (bottom) 46
Figure 27: Reference Point Method Coupling 48
Figure 28: RP Load Profiles, Segment A (top), Segment B (mid), Segment C (bot) 51
Figure 29: Celestial Icosahedron Outer Diameter (left), Arch Angles (right) 53
Figure 30: Element Width Representation for Beam Elements 55
Figure 31: Representative Loading Scheme for Curved Beam [23] 57
Figure 32: Bare Celestial with Line Loads and Boundary Conditions 60
Figure 33: Partitioned Skin Mesh 61
Figure 34: Boundary Conditions for Celestial with Skin (left), Close-up of A (right) 63
Figure 35: Celestial Schematic for Compression Loading 64
Figure 36: Coupling Constraint Used for the Compression Analysis 65
Figure 37: Demonstration of the Coupling Constraint 66
Figure 38: Potential Contact Points during Loading 66
Figure 39: Fortus 450mc 3-D Printer 68
Figure 40: 3-D Printing Fill Pattern 69
Figure 41: Printed Celestial with Support Material 70

Figure 42: Printed Celestial with Only Center Support 71

Figure 43: Liberated 3-D Printed Celestial Icosahedron 71

Figure 44: Loading Puck (Left), Nested with Celestial Structure (Right) 73

Figure 45: Acumen Electrodynamic Test Frame with Specimen 74

Figure 46: Deformed ROM Beams for Load Profile 1, Iteration 2 79

Figure 47: Deformed ROM Beams for Load Profile 2, Iteration 3 81

Figure 48: Tracked Intersections During Loading 82

Figure 49: Stress in Celestial Frame with Load Profile 1, 2.38 mm 83

Figure 50: Stress in Celestial Frame with Load Profile 1, 2.64 mm 84

Figure 51: Stress in Celestial Frame with Load Profile 2, 2.99 mm 86

Figure 52: Deformed Celestial with Skin (top), without Skin (bottom), 2.64 mm 89

Figure 53: Deformed Celestial with Skin (top), without Skin (bottom), 2.99 mm 90

Figure 54: Traced Ring Path for Displacement Measurement 92

Figure 55: Symmetry Plots, Ring Type 1 (top), Type 2 (Bottom) 93

Figure 56: ROM of Segment A with Adjusted BC 95

Figure 57: Adjusted ROM Displacements Compared to Full Celestial Displacements ... 98

Figure 58: ROM for Segment A with Modified BC, Case 1 (top) Case 2 (bottom) 99

Figure 59: Segment A Isolated from Celestial Model, 2.99 mm 99

Figure 60: Modified ROM Boundary Conditions 100

Figure 61: Modified ROM Stress Comparison, Original (top), Modified (mid), Modified with New Load (bot) 101

Figure 62: Loading vs Print Orientation, Specimen 1 (left) Specimen 2 (right) 102

Figure 63: Experimental Data for Two Specimens..... 103
Figure 64: Experimental Data: Close-Up of Experiment Prior to Fracture..... 103
Figure 65: Deformed Specimen 2..... 104
Figure 66: Fracture Locations, Specimen 1 (left) Specimen 2 (right)..... 105
Figure 67: Fracture Planes, Specimen 1 (left) Specimen 2 (right)..... 105
Figure 68: Load-Displacement Curve from Compression Model..... 107
Figure 69: Celestial Under Vertical Compressive Loading to Max Stress..... 108
Figure 70: Celestial Under Vertical Compressive Loading to Max Stress in Segment Midsection..... 109
Figure 71: Experimental Results Compared to Original Model..... 110
Figure 72: Print Orientations for Shelton's Experiments [24]..... 111
Figure 73: Deformation Regions of Celestial Under Compression..... 113
Figure 74: Model and Experimental Force vs Displacement, 1.35 GPa..... 114
Figure 75: Failure Location for Specimen 2, Top Trace (top) Bottom Trace (bottom).. 116
Figure 76: Failure Location for Specimen 1, Top Trace (top) Bottom Trace (bottom).. 117
Figure 77: Load Displacement Curve of Frame and Skin, Compressive Loading..... 119
Figure 78: Internal Energy and Kinetic Energy for Quasi-Static Analysis..... 120
Figure 79: Compression Analysis with Skin, Skin Stress (top) Frame Stress (bot, top trace)..... 122

List of Tables

Page

Table 1: Spectra Material Properties [11] 9

Table 2: Material Properties for Moore's Analysis [12] 9

Table 3: Ultem 9085 Material Properties [15] 10

Table 4: Intersection Stiffness Iterations 23

Table 5: 2-Segment Arch Geometries 24

Table 6: 2-Segment Arch Stiffnesses at Each Iteration 25

Table 7: Intersection Comparison to Arch Sums 26

Table 8: Comparison of Polynomial Fit to Nodal Forces 34

Table 9: Comparison of Polynomial Fit to Nodal Forces 44

Table 10: Effect of Element Width on the Total Force on Segment A 54

Table 11: Critical Buckling Loads for Curved Beams 58

Table 12: 2-Segment Arch Stiffnesses for ROM Load 1 Iterations 76

Table 13: ROM Stress Levels for Load Profile 1 77

Table 14: ROM Boundary Displacement by Intersection Load Case 1 78

Table 15: 2-Segment Arch Stiffnesses for ROM Load 2 Iterations 79

Table 16: ROM Stress Results for Load 2 80

Table 17: ROM Boundary Displacement by Intersection, Load Profile 2 80

Table 18: Load Profile 1 Displacement Comparison 85

Table 19: Load Profile 2 Displacement Comparison 87

Table 20: Intersection Displacements (mm) for 2.99mm Celestial with Skin 94

Table 21: Modified Boundary Conditions 96

Table 22: Ultem 9085 Tensile Test Properties [24]..... 111

Table 23: Compressive and Flexural Properties of Ultem 9085 [25] 112

Table 24: Rule of Mixtures Breakout for Modulus Determination 113

A REDUCED ORDER MODEL OF THE CELESTIAL ICOSAHEDRON AS THE SUBSTRUCTURE FOR A LIGHTER THAN AIR VEHICLE

1. Introduction

1.1. Overview

The use of buoyancy as a means of generating lift was the first method of achieving manned flight and dates back to 1783 when the Montgolfière brothers successfully achieved human flight using a hot air inflated balloon [1]. Shortly afterward a hydrogen filled balloon achieved flight which was constructed by the Roberts brothers. These lighter-than-air vehicles (LTAV) were the first of in an era of manned flight that would lead to various types of balloons and airships. The most ideal lifting gases for these types of vehicles are: hot air, diatomic hydrogen, and helium. Hydrogen and helium have the largest density ratio compared to the atmosphere of Earth, which is mainly composed of diatomic nitrogen. Hot air is simply less dense than surrounding colder air due to the molecules being at a higher energy state. Monatomic hydrogen would be the best choice, but it is not stable in this form. The buoyancy is then determined by Archimedes principle which states that the upward force is the difference between the density of the displacing volume and the density of the displaced volume. This relationship can be expressed as a ratio of weight to buoyancy shown in Equation (1.

$$\frac{W}{B} = \frac{V_{gas}\rho_{gas} + W_{structure}}{V_{vehicle}\rho_{air}} \tag{1}$$

Where W is the total weight of the vehicle, $W_{structure}$ is the weight of the vehicle without the gas, B is the buoyancy, V_{gas} is the volume of the lifting gas, ρ_{gas} is the density of the lifting gas, $V_{vehicle}$ is the volume of air that the vehicle displaces, ρ_{air} is the density of the surrounding air. Thus, the greater the difference in density between the lifting gas and the atmospheric gas, the greater the potential lifting force. The primary choice in lifting gases in modern times is helium. This is largely due to its non-flammable nature which make it a safer choice than hydrogen despite being more expensive and harder to acquire. A fourth option of a 'lifting gas' exists in the form of a vacuum; the potential to evacuate a volume and have no gas at all so that the density of the 'gas' is zero or close to zero. Ideally, this would yield the entire density of the displaced gas as the lifting potential instead of the difference in densities. The difficulty in this is compared to using an actual lifting gas is that is generates a negative pressure that is inherent about a vacuum. This negative pressure needs to be resisted in some manner in order to maintain a shape. A helium balloon only needs a thin, air-tight layer to contain the helium since there can be an equal or positive pressure in the balloon to maintain the shape. A vacuum filled vessel of the same construction would collapse upon evacuation. Various designs have been theorized to be able to support the load of a vacuum and still achieve buoyancy. Several of these designs involve a membrane supported by a substructure.

The work described in this thesis builds on the work of prior research in vacuum lighter-than-air vehicles (VLTAV). This work further investigates the viability of the celestial icosahedron as a possible supporting substructure through finite element analysis

(FEA) modeling and experimentation. The celestial icosahedron, shown in Figure 1, consists of nine identical rings that are rotated at 45 degree angles about three different axes with the same center point. This geodesic shape was one of the designs suggested by Cranston as a viable option that could support the vacuum while still being lightweight enough to have a positive buoyancy during his investigation of geodesic shaped structures [2].

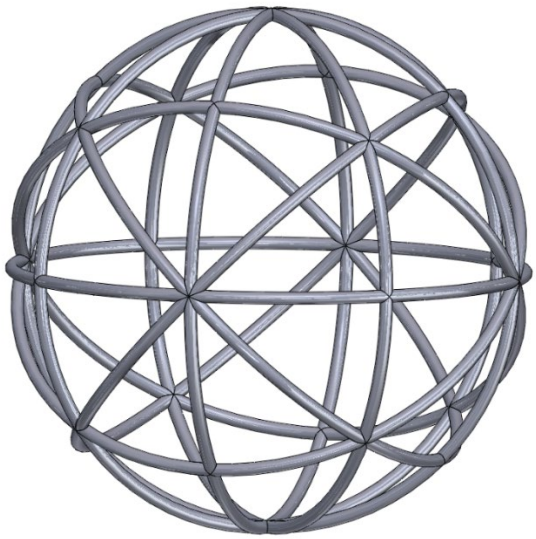

Figure 1: Celestial Icosahedron

1.2. Objectives

The objectives of this thesis are to characterize the behavior of the celestial icosahedron in such a way as to understand its limitations and develop a modeling technique that can be used to expedite future pursuits. The design objectives of the project are as follows:

- Determine the necessary beam cross-sectional diameter to support the load of a vacuum based on a reduced order model (ROM) representing individual members as curved beam members with FEA
- Determine a loading scheme that best represents the loads that a vacuum pressure would exert on the support structure
- Additively manufacture the celestial icosahedron structure with using an FDM method with the material ULTEM 9085
- Experimentally test the printed structure under uniaxial compression and observe deformations and failure
- Model the full celestial icosahedron using FEA to compare to the results of the experiments

1.3. Motivation

The motivations for producing a VLTAV are focused on the rising cost and availability of the helium and the higher lifting potential of a vacuum versus a lifting gas. A report put out by the US Bureau of Land Management show that the price of Helium has risen from $84.40 per thousand cubic feet in 2016 to $210 per thousand cubic feet in 2019 [3][4]. Helium is the still the preferred lifting gas between hydrogen and helium as it is nonflammable. In terms lifting gases, the most ideal lifting gas would by atomic hydrogen with a molecular weight of one compared to diatomic hydrogen or helium with atomic weights of 2. This would provide the best mass difference between the lifting gas and the nitrogen atmosphere; however, hydrogen does not occur nor stay in its atomic

state naturally. The appeal of vacuum is the entire mass of the displaced gas contributes toward the buoyancy of the vehicle. In this way vacuum as a lifting ‘gas’ has a greater lifting potential than anything with mass; albeit a small advantage. Utilizing a vacuum is not without difficulty as the evacuated volume requires support to withstand the atmospheric pressure. This necessitates the vehicle be designed with a rigid structure rather than a flexible containment such as balloons. Rigid bodies themselves are not out of the realm of possibilities as airships such as the Hindenburg were designed with a rigid bodies even though they were filled with a lifting gas. Several applications and advantages of using a vacuum as the lifting ‘gas’ are described by David Noel in a 1983 paper [5]. In this article, Noel suggested application ranging from high altitude rain water collection, solar energy collection, and communications networks. Noel also states that the advantage to using a vacuum, other than the lifting potential, is the ability to combat leaks. Leaks are an inevitable reality that accompany the separation of gases. Leaks in a vacuum structure can be combated by pumping out the excess air to the desired vacuum state [5]. This is a much simpler remedy to leak compared to the requirement of gas filled volumes since the escaped gas needs to be replenished from a source. This also grants the ability to adjust the level of vacuum to suit any level of altitude that could be attained and maintained. The operation of the VLTAV would not be significantly different than any other LTAV so any current application that uses a lifting gas could be replaced with a vacuum alternative.

1.4. Prior Research

The concept of using a vacuum to produce a lifting force has remained just that; a concept. A theory of using vacuum filled spheres for buoyancy dates back to 1663 with Francesco Lana de Terzi [6]. De Terzi's design was that of evacuated thin shelled copper spheres. This idea of using a vacuum filled, single material shell sphere has been proven to be an ineffective way to create a lighter than air vehicle. De Terzi's design itself was disproved in 1981 by Bushnell [7]. These copper spheres experience buckling as shown in Figure 2 and eventually collapse as the vacuum level increases.

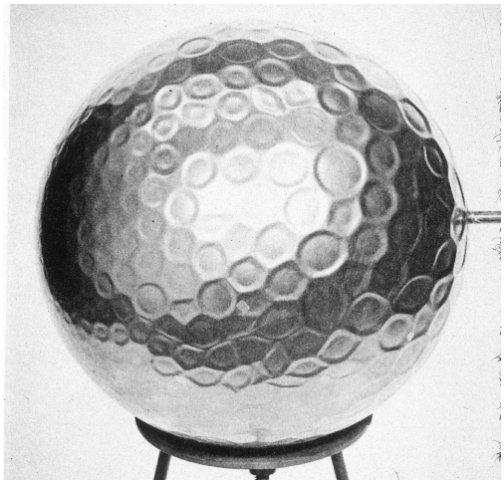

Figure 2: Buckled Copper Sphere Under Vacuum [7]

A single material concept has also been shown to collapse due to buckling by Andrey M Akhemeteli and Andrey V Gavrilin in 2005 [8]. Their calculations are based on sea level air density and the requirements to achieve neutral buoyancy are shown in Equations (2) and (3).

$$P_{cr} = \frac{2Eh^2}{\sqrt{(3(1-\mu^2)}} \frac{1}{R^2} \tag{2}$$

$$\frac{E}{\rho s^2} = \frac{9P_{cr}\sqrt{3(1-\mu^2)}}{2\rho_a^2} \tag{3}$$

This places a requirement for a very stiff and light weight material in order to construct a shelled sphere able to contain a vacuum, one that does not currently exist.

Alternatively, several other concepts have been proposed to generate the needed structural strength while achieving neutral buoyancy. Akhemeteli and Gavrilin proposed a multiple layer sandwich core shell design [8]. Two other concepts were explored by Trent Metlen in 2012; one invloved stiffening a shelled sphere with an isogrid and the other a geodesic sphere structure covered in a membrane [9]. Both methods produced results that could theoretically be manufactured and use materials that are available. Concerns were expressed by Metlen over the scalability of the grid-stiffened method since it relies on continuously wound carbon fibers [9]. The geodesic sphere method seemed to show the most promise for both scalability and ease of manufacture.

The geodesic structure that Metlen explored was a regular icosahedron, shown in Figure 3, which consists of 20 identical equilateral triangles. Several others proceeded to explore the possibility of the icosahedron as a geodesic support structure.

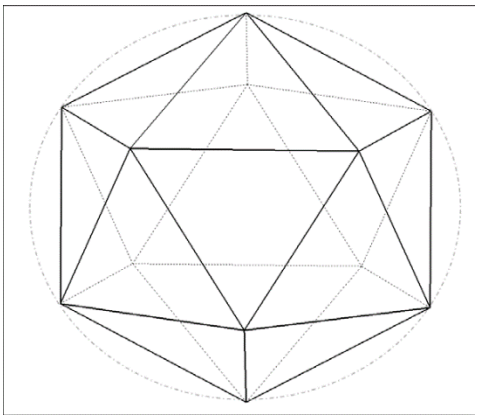

Figure 3: Simple Icosahedron Geodesic Shape [9]

In 2014, Ruben Adorno-Rodriguez modeled the structure with the goal of determining the necessary material properties to enable a 304.8mm in diameter structure to support a vacuum and float [10]. The structures that were capable of floating were analyzed with the mechanical properties of carbon nanotubes which are not at this time readily available in the form required. In 2016 Brian Cranston explored additional geodesic shapes that could be used to support a vacuum and be made of real materials even if the manufacturing method was not mature. Cranston proposed two designs, the hexakis icosahedron and the celestial icosahedron [11]. The hexakis icosahedron is similar to the simple icosahedron in that it is composed of straight members with flat faces; this design however, is much more refined and consists of 120 faces. The celestial icosahedron consists of 9 identical rings at 45 degree angles to each other. The members of this structure remain curved which allows the structure take on a more spherical shape. Cranston's focus was primarily on the hexakis icosahedron, but a brief feasibility analysis was done on the celestial icosahedron. The hexakis icosahedron showed great promise in

being able to support the vacuum loads. The material properties used by Cranston were that of the Spectra® fiber; its properties are shown in Table 1 [11].

Table 1: Spectra Material Properties [11]

	Spectra
Density	970 kg/m^3
Poisson's ratio	0.33
Modulus of Elasticity	172 GPa
Material Strength	3 GPa
Specific Modulus	1.77E+08 E/ρ
Specific Strength	3.09E+08 E/ρ

Cranston acknowledged that the Spectra® fiber was an up-and-coming technology and hadn't yet been manufactured in the method needed to serve as both the structure and the skin. In 2018 Kyle Moore investigated the celestial icosahedron and determined the minimum structure diameter for neutral buoyancy to be 0.8001 meters. This design was based off of the structural members constructed from carbon nanotubes (CNT) and the skin constructed from graphene [12]. These material properties are shown in Table 2.

Table 2: Material Properties for Moore's Analysis [12]

Material	Density (kg/m^3)	Poisson's Ratio	Young's Modulus (GPa)	Yield Stress (GPa)
CNT	1250	0.33	293	3.8
Graphene	2000	0.10	500	50

A second design with and overall diameter of 1.2192 meters had a weight to buoyancy ratio of 0.7257. These designs also were restricted by the availability of the materials

selected in the form of which they were to be applied to the vehicle. The celestial icosahedron design would later be investigated by Dustin Graves for dynamic forces that the vehicle might encounter in an operational setting [13].

All of the designs have proved feasible on paper through FEA and only limited experimentation has been done. Cranston did conduct experiments on the icosahedron and successfully matched the experimental data to the model during an axial compression of the structure [11]. Other experiments have been to investigate the dynamic response of aerodynamic forces on the vehicle. Kevin Greenoe began working towards model validation experiments using 3-D modeling as the method of manufacturing [14]. The material selected for this endeavor was Ultem 9085, a proprietary thermoplastic manufactured by Stratasys. The material properties for this material are shown in Table 3. Although the material chosen for this research did not possess the required strength and stiffness as the past research had determined, Ultem 9085 was one of the strongest thermoplastics available for 3-D printing. The ultimate purpose of the experiments by Greenoe was to validate the models' ability to predict the behavior of the structure under load.

Table 3: Ultem 9085 Material Properties [15]

	XZ Orientation (MPa)	ZX Orientation (MPa)
Tensile Strength (Yield)	47	33
Tensile Strength (Ultimate)	69	42
Tensile Modulus	2150	2270
Flexural Modulus	2300	2050
Compressive Strength (Yield)	100	87
Compressive Strength (Ultimate)	181	90

At this stage of experimentation, the purpose was not to produce a structure that could float but could support a vacuum. Greenoe used a differential equation approach to determine the minimum beam diameter for the circular cross-section beams of a 203.2 mm diameter structure. The analysis assumed straight members between the vertices subjected to an axial compressive force and a transverse triangular load distribution. Ultimately, Greenoe determined that a minimum beam diameter of 5.08mm would support a vacuum [14]. A new element of uncertainty was now introduced along with the method of fabrication; 3-D printing. This manufacturing method is known to produce anisotropy within the printed part. This was acknowledged by Cranston and also investigated by S. Bhandari for thermoplastic extrusion for 3-D printing [16]. This anisotropic behavior would need to be quantified in order for the model to accurately represent the experimental results. Greenoe's experiments explored the effect of print orientation on the material properties as it they pertained to isolated single rings. These rings were printed at three print orientations, 0^o, 45^o, and 90^o relative to the build direction. The results of the experiments are shown in Figure 4 with the modulus determined through FEA comparison to the experimental results. In both cases the

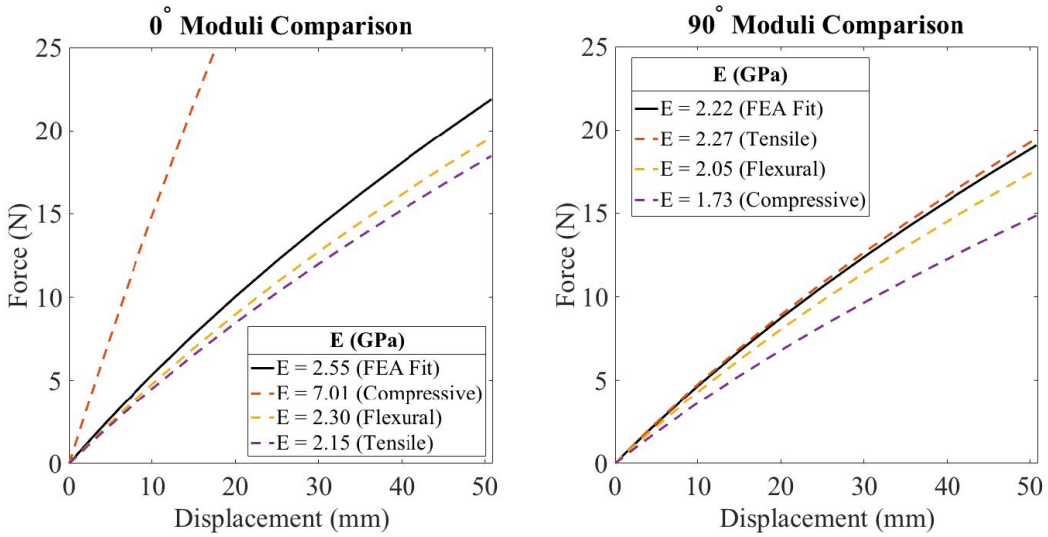

Figure 4: Experimental Results vs Published Properties for Ultem 9085 [14]

The experiments showed a definite difference between the material modulus of elasticity from 0º orientation and the 90º orientation. It was observed that the modulus for the 90º orientation matched most closely to the flexural modulus of the material. It should also be noted that the 90º orientation makes up four of the 9 rings and the 0º orientation is only found in one ring referencing the orientation of the structure in Figure 1. A continuation of Greenoe's work would be to fabricate the full structure and conduct experiments to determine its similarities to the FEA models.

1.5. Current Research Implications

The current research builds on the additive manufacturing experiments conducted by Greenoe. It revisits the analysis for determining the beam geometry for the structure through an FEA model representing the beams as curved members with unique boundary conditions in a ROM. The material properties as determined by Greenoe, specific to the

print orientations, have been taken into consideration for the ROM. The most conservative approach to the material properties was taken between the three tested print orientations. The experiments conducted with a full celestial icosahedron through 3-D printing provide insight into the fidelity of the models. Several studies have been done identifying vehicle designs capable of floating with a vacuum, but these have not been validated with experiments. This is mostly due to the materials selection of the designs and the availability of those materials. A validation of the modeling process, even with a material that is not capable of producing a beneficial weight to buoyancy ratio, will increase the potential of creating a successful vehicle as more capable materials become available. Future designers should have more confidence that their designs are capable of floating under vacuum.

2. Research Methodology

2.1. Chapter Overview

This chapter provides details on how each step of the research was conducted, but does not necessarily provide the results that were obtained by each step. The first step in this project was to evaluate the members of the celestial icosahedron using an FEA approach. This was not only to provide a confirmation of the results obtained from prior researchers for the beam geometry, but would hopefully demonstrate a more ideal geometry since this method would take the members' curvature into consideration. A secondary purpose of this FEA approach was to lay the groundwork for evaluating more complex beam geometries. The second step was to model the full celestial structure using FEA and evaluate its performance under vacuum and under a uniaxial load that will later be complimented with experimentation. The third step was to manufacture the full celestial icosahedron structure with the determined beam geometry. The manufacturing process chosen was fused deposition modeling (FDM) additive manufacturing (AM) with the material Ultem 9085. The fourth step was to mechanically load the printed structure uniaxially. This loading method does not represent a vacuum loading but provides insight into the failure modes of the material. The expectation was that the structure would collapse before any fractures occur as was observed in the single ring experiments. The fifth step was to compare the results of the mechanical testing to the FEA results to determine how well the model matched the behavior of the mechanical test and make adjustments accordingly. The end results of the research should provide valuable insight

into how well the structure performs compared to modeling efforts so that adjustments may be made by subsequent researchers who may endeavor to construct such structures of sizes capable of carrying a payload.

2.2. Reduced Order Modeling Theory

In an effort to further refine the approach taken by Greenoe to represent the members of the celestial icosahedron, a finite element approach was proposed that would evaluate the members as curved beams. This model attempted to represent the interactions of the different members of the structure without modeling the entire structure; in this way the model was considered a reduced order model (ROM). The concept behind the ROM is not a novel approach in itself for doing analysis of these types of structures. Greenoe and Just both used partial models of the full structure to help predict its behavior [14][17]. Greenoe predicted the behavior of a single vertex-to-vertex member simplified as a straight beam with a differential equation solution. Just isolated the characteristic triangle of an icosahedron to perform an analysis and conduct an experiment with. The approach used here more closely matches the approach of Greenoe as the geometry is two-dimensional in nature. The individual members of the celestial icosahedron were isolated with specific boundary conditions and loading schemes. The celestial icosahedron is made up of 48 identical triangles; therefore, there are only three unique vertex-to-vertex members. An example of this is shown in Figure 5. Greenoe's method was solving a differential equation for a beam column while the approach in this research was an FEA approach with curved beams and unique boundary conditions.

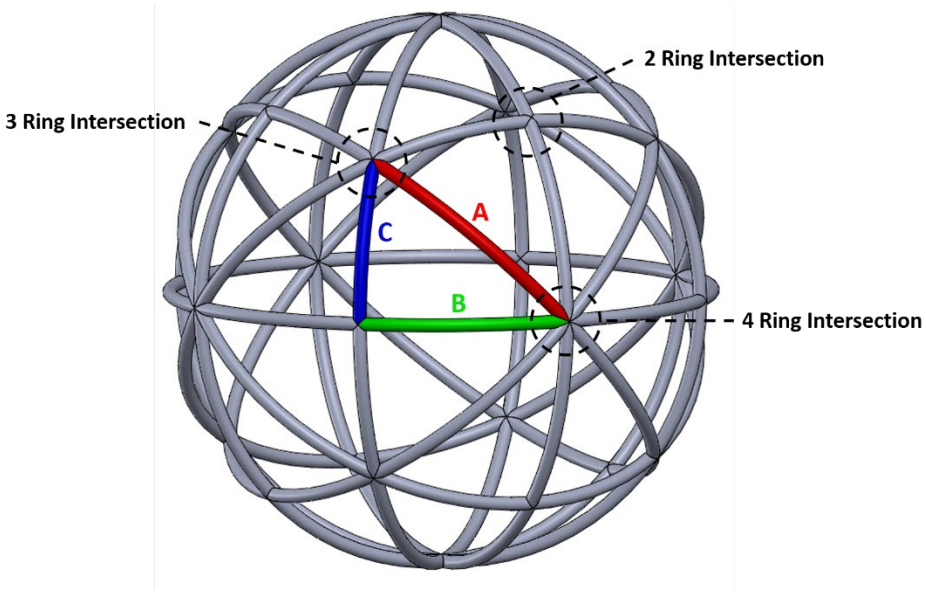

Figure 5: Celestial Icosahedron Characteristic Triangle

The premise of this ROM is that the boundary conditions are something other than fixed or simply supported. It is also based on the understanding that the overall structure is not rigid; when a vacuum is applied to the membrane-covered vehicle, the structure will experience deformation along the length of the members but also at the vertices. This will cause the overall structure to be something other than perfectly spherical. From this basic understanding, some assumptions were made about how the members would be supported. These assumptions were:

- The members' displacement in the tangential direction will be restricted due to symmetrical axial forces
- Each vertex will have a unique stiffness that will resist displacement in the radial direction

- The rotations of the members at the vertices are small and were assumed to be zero; rotations at the boundaries were restricted

The resulting model would represent a single member with clamped rotational degrees of freedom and movement allowed only in the radial direction that is resisted by a spring. This condition could be described as clamped-radially resisted which is slightly modified from the clamped-radially guided condition used by Pilkey to describe a similar set of boundary conditions [23, Table 16-6] shown in Figure 6.

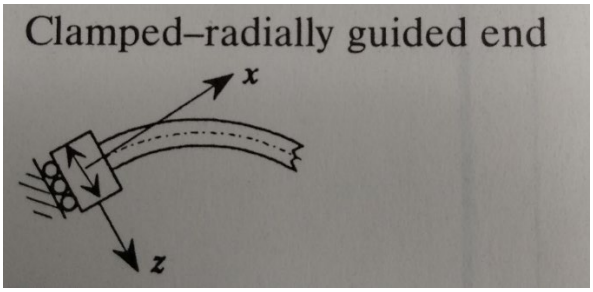

Figure 6: Clamped-Radially Guided BC from Pilkey [23

The resistance comes from a spring oriented in the radial direction. A representation of this model is shown in Figure 7. Three unique models were generated for each of the three segments. The models possessed unique values for the spring constants, K_i, and load profiles.

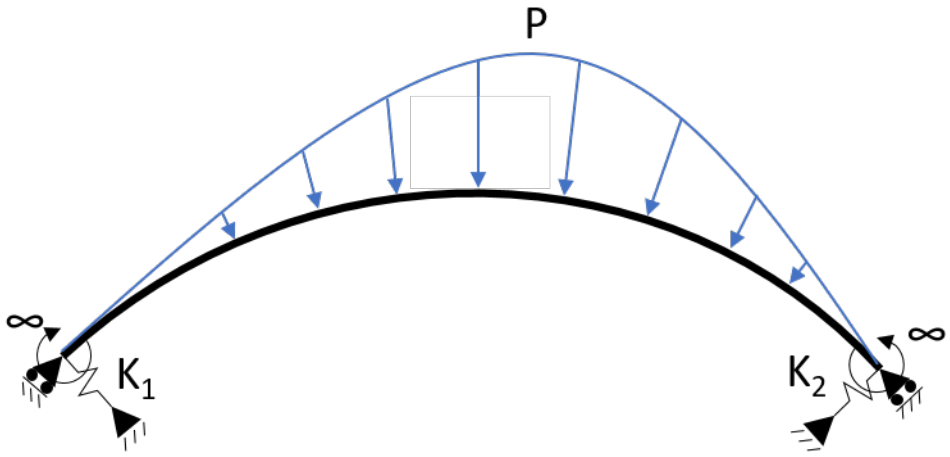

Figure 7: Reduced Order Model Configuration

This model theoretically considers the stiffnesses of the intersections, or vertices, within the celestial icosahedron which should give a more accurate prediction of the members' behavior compared to having rigid supports. The addition of the springs to resist radial displacements at the boundaries adds an amount of pre-work needed to determine the values of the spring constants before the models can be run.

2.2.1. Finite Element Analysis for the Reduced Order Model

The main tool used for evaluating the structural members for this research was finite element analysis. The software used was Abaqus/CAE 2016 [18]. The celestial members were modeled using Abaqus's B32 type beam elements. Beam elements were selected since the members are expected to be long and slender. This reduces the dimensionality of the modeled members as the number of degrees of freedom (DOF) required for the analysis are reduced based on the assumptions of beam theory. The B32 element is a quadratic element with three nodes based on Timeshenko's beam theory.

These elements are capable of handling both axial and transverse loads which is necessary for the ROM due to the loading scheme used to model the structural members [10, pg 55][18]. The analysis of the models used what Abaqus calls a static, general step. This modeling method uses the Newton-Raphson method for solving non-linear equations [19]. Non-linear geometries were also present due to the curvature of the members. In addition, the deflection of the beams may reach an instability point under loading where the curvature inverts to stabilize. This behavior is referred to as snapping which is undesirable for this application as it could result in a structural collapse or at the very least a reduction in the displaced volume and any payload capability. From the experiments conducted by Greenoe [14] it is likely that a structure made from Ultem 9085 will deform rather than fracture so this is an important phenomenon to investigate.

The FEA technique for the modeling process to determine the load profiles required the use of membrane and shell elements. This technique will be discussed in later sections specifically relating to the load profile determination.

2.2.2. Boundary Condition Spring Constants

The spring constants used in the ROM represent the interactions of the total structure on the individual members. Determining these spring constants used in the boundary conditions required a separate study in itself. The purpose of the ROM was to reduce the amount of effort and computing time needed to determine the stresses with the members of the celestial under vacuum. Simplicity was a focus of this method as its purpose was to reduce computational workload and still reflect the behavior of the intersection. If determining these variables proved to be too resource consuming, the

method would lose its usefulness of rapidly establishing the celestial frame dimensionality.

The first step was to determine exactly what the springs represented. The intention was to have the spring represent the interactions of the members at a given intersection with the understanding that the structure will flex and displace in a certain manner. The spring constants were assumed to be the resistance of the intersection as a whole to displace radially. This resistance was interpreted as a loading constant with the units N/m. As an example of the method used to determine this stiffness, a member of interest was chosen from the full structure such as the member highlighted in Figure 8. This member was supported by a 4-ring intersection on one side and a 3-ring intersection on the other. Isolating the members constituting the 4-ring intersection allows for the stiffness of this intersection structure to be determined; this was done by separating the members at their next vertex as shown in Figure 9 by the circles.

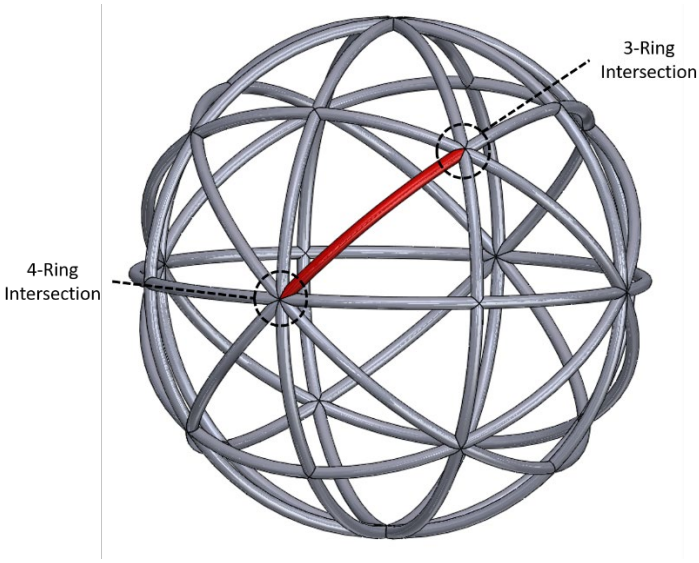

Figure 8: Individual Member Example

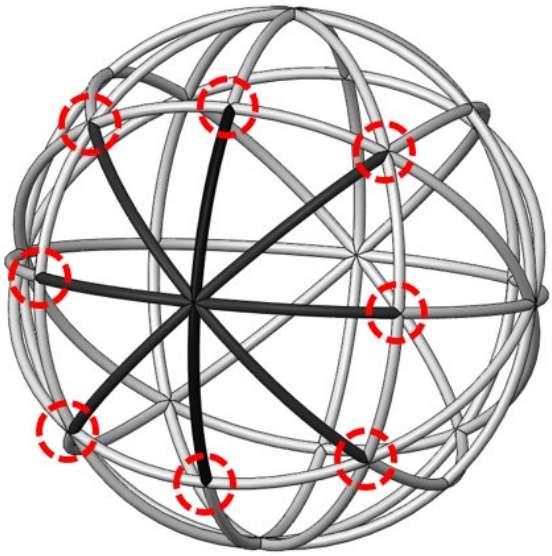

Figure 9: 4-Ring Intersection Isolation Process

For this model, each of the free ends was initially supported with clamped supports. It would be ideal if each of the free ends could be supported in the same way as the ROM, clamped radially resisted. This however, would have created a cyclic type of situation

where the stiffness of any intersection could not be determined without knowing the stiffnesses of all the other intersections. As a result an iterative approach was ued that would converge on the result of the ROM boundary conditions had they been used initially. After the first iteration with clamped supports, the ROM boundary conditions were applied with the stiffnesses determined by the previous step. An arbitrary load was applied as a concentrated force at the intersection as shown in Figure 10. By tracking the displacement of the loading point, the stiffness K_i was determined as it related to the current modeling scheme as shown in Equation 4

$$K_i = \frac{F}{\delta_i} \tag{4}$$

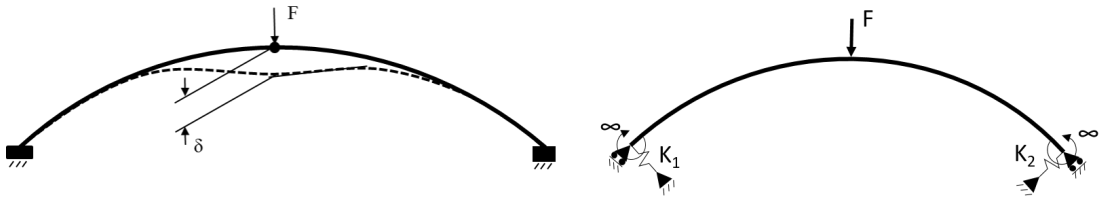

Figure 10: Single Member Models for Stiffness Determination

This was done for the three intersection types. The models were then modified to contain the clamped-radially resisted boundary condition type with the spring constants from the previous step. The load was applied in equal fashion as the prior step and new intersection stiffnesses were determined. After the third iteration, the results appeared to be reaching a level of convergence; the resulting stiffnesses are shown in Table 4.

Table 4: Intersection Stiffness Iterations

Intersection	Iteration 1		Iteration 2		Iteration 3	
	Disp. (mm)	Spring Const. (N/mm)	Disp. (mm)	Spring Const. (N/mm)	Disp. (mm)	Spring Const. (N/mm)
2-Ring	0.0539	127.9	0.0677	101.9	0.0681	101.3
3-Ring	0.0422	163.5	0.0561	122.9	0.0588	117.2
4-Ring	0.0424	162.5	0.0546	126.2	0.0582	118.5

This method proved to be quite time consuming and the models became quite large and required several iterations. Had the structure's geometry been more complex, this process would not likely be saving any computational resources.

In an attempt to reduce the amount of work that went into determining these final spring constants the members that made up the intersections were treated as 2-segment arches. By examining the celestial, it was observed that the entire structure was made up of only four unique 2-segment arches. These arches made up the intersections in various combinations. Referring to the labels in Figure 7, the 2-segment arches were made of the following segment combinations: B-B, C-C, A-C, and A-A. These arches are depicted in Figure 11 as arches 1, 2, 3, and 4 respectively. The left and right sweeping angles of each arch from the intersection point are shown in Table 5.

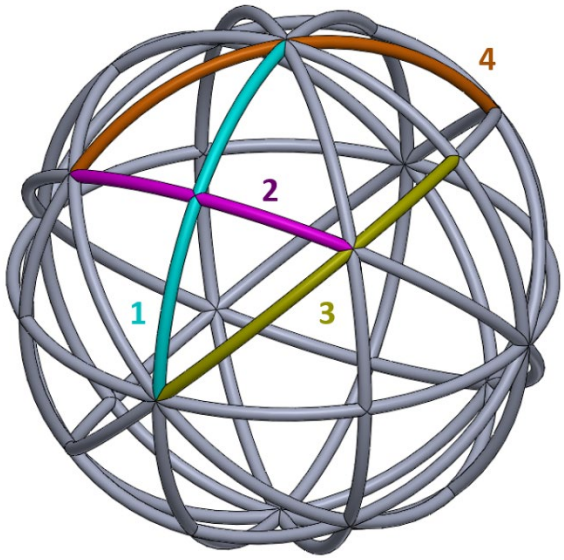

Figure 11: Four 2-Segment Arches Identified

Table 5: 2-Segment Arch Geometries

Arch	Left Angle	Right Angle	Total Sweeping Angle
1	45	45	90
2	35.26	35.26	70.52
3	54.74	35.26	90
4	54.74	54.74	109.48

It was theorized that the intersection stiffnesses could be determined by knowing the stiffnesses of the individual arches that made up the intersection. For instance, in the intersection example used previously, the intersection was made up of two A-A arches and two B-B arches. Four models were built consisting of the 2-segment arches. An arbitrary load was applied as a concentrated force at the location along the arch where the intersection would be. Two sets of models were initially run with the boundary conditions being either clamped-clamped or simple-simple. Subsequent iterations replaced these boundary conditions with the clamped-radially resisted conditions to investigate if

boundary conditions of this type would lead to a more accurate representation of the full intersection. Example schematics of the A-A and A-C 2-segment arches and the load placements is shown in Figure 12. The results from these 2-segment arch models are shown in Table 6.

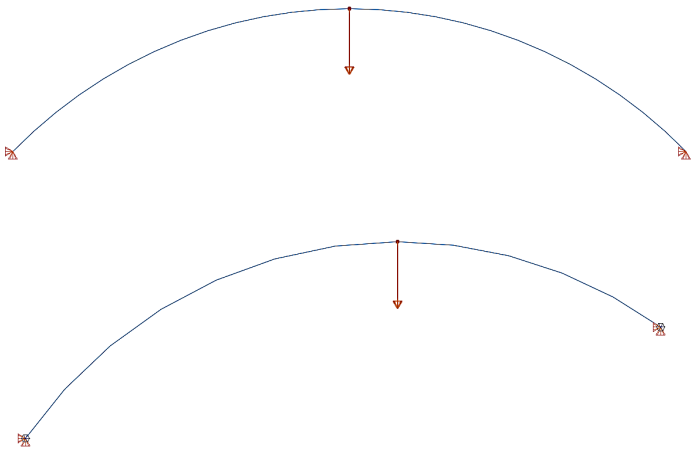

Figure 12: Example Schematics of 2-Segment Arches, A-A (top), A-C (bottom)

Table 6: 2-Segment Arch Stiffnesses at Each Iteration

Arch (N/mm)	Iteration 1		Iteration 2	Iteration 3
	Clamped BC	Pinned BC		
1	50.0	37.4	40.8	39.9
2	77.8	66.2	64.2	61.4
3	37.2	23.5	31.0	29.5
4	31.2	21.7	25.6	24.3

The intersections are made up of the following combinations of arches: the 2-ring intersection is made from a B-B arch and a C-C arch, the 3-ring intersection is made of three A-C arches, and the 4-ring intersection is made of two A-A arches and two B-B arches. Evaluating these combinations of arches and comparing them to the full

intersection models that had been iterated on, it can be seen that a close approximation can be made for the 2 and 4-ring intersections by summing the results of the simply supported arch models from iteration 1. The 3-ring intersection can be closely approximated by summing the result of its components with the fixed supported model. These results are shown in Table 7. This case was ideal since it would not require several iterations to come to a result. The trend of the iterations was toward a result similar to that of the pinned, or simply supported, boundary condition. The method of determining the spring constants in all subsequent analyses would not include iterations on the arch models but would use the simply supported or clamped boundary conditions.

Table 7: Intersection Comparison to Arch Sums

Intersection	Final Stiffness (N/mm)	Sum of Single Arches (N/mm)	% Difference
2-Ring	101.3	103.6	2.27
3-Ring	117.2	111.7	4.69
4-Ring	118.5	118.3	0.17

All the results are within 5% which was deemed good approximation. This method of modeling the four, 2-segment arches would replace the full intersection modeling in order to achieve the spring constants needed for the ROM of the individual segments. In terms of order of operations, this set of 3 models would be the first step in evaluating an alteration to the beam geometry.

2.2.3. Load Profile Determination

The load profile that was to be applied to each of the members during the analysis was a critical component of the overall model. Without modeling the entire structure with the membrane, it is difficult to know exactly what loads the members are experiencing

and how the load is transferred across the structure. The majority of previous research did not focus on the loads applied to single members of the structure, but rather applied the load to the entire structure as a whole. Greenoe's method for determining the load profile was based on geometry. Greenoe used a planar triangle representation of the curved triangular faces. This geometry was divided into three smaller triangles based on the centroid shown in Figure 13 and would represent triangular load distributions. The shortest distance between the triangle segment and the centroid was used to determine the peak load of the triangular load distribution per Equation (5).

$$w_o = 2Pd \tag{5}$$

Where w_o is the peak load rate, P is the pressure applied to the surface, and d is the minimum distance between the centroid and each side. The peak of the triangular distribution is shown in Figure 13 as w_o.

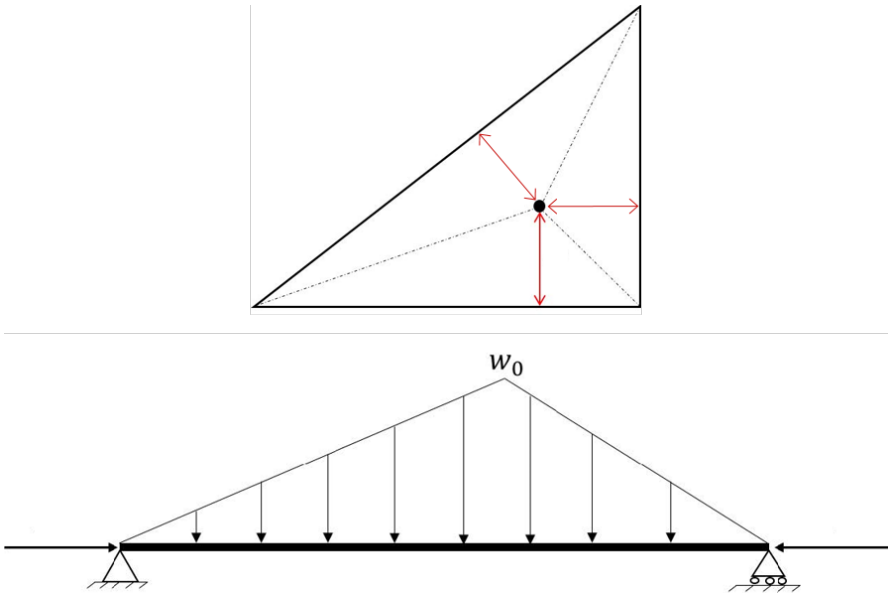

Figure 13: Geometric Load Distribution (top) and Greenoe's Model's Loads and BCs (bottom)[14]

This method assumed that a flat triangle was a good approximation for the curved triangle that it represented.

The load profile methods for this research utilized an FEA model of the curved characteristic triangle. It was assumed that the members that make up the perimeter each characteristic triangle would support the hydrostatic forces experienced by that surface area when the volume is evacuated. This means that each member is carrying the load of a portion of two characteristic triangles. The characteristic triangle was modeled as a stand-alone surface, simply supported along the entire perimeter with a sea level pressure, 101.325 kPa, applied uniformly to the surface. The nodal reaction forces were recorded to determine the load profiles. The load profiles would change based on the total celestial diameter. The total structure diameter for this research was 203.2 mm (8 inches). A

model was built of the characteristic spherical triangle the same diameter of the structure. The type of element to be used was determined partly from the analysis done by Adorno-Rodriguez during his analysis of the simple icosahedron. Adorno-Rodriguez determined that modeling the skin of the structure with either membrane or shell elements did not significantly affect the displacements of the skin for the given analysis as long as the skin was very thin [10]; however, two separate methodologies were used for the load profile determination which will be discussed in detail later. Method 1 utilized shell elements while method 2 utilized membrane elements. The distinction between the two is that membrane elements cannot take transverse loads without non-linear stabilization. Shell elements were better suited for the first instance to determine the load profile based on the starting shape of the triangle. A rigid structure was needed to transfer the load to the substructure. For this case, the shell elements were more appropriate because they carry bending stiffness, unlike membrane elements, which was required for the shape to be maintained [18]; additionally, the rigidity was achieved by increasing the skin thickness. This thick shell would no longer be expected to behave as a thin membrane rendering membrane elements ineffective. The shell elements used were Abaqus's S4R element, a reduced integration linear quadrilateral element. Similar to Adorno-Rodriguez, the other method of load profile determination utilized membrane elements to represent the skin. These elements were linear quadrilateral elements (M3D3R) with reduced integration and linear triangular elements (M3D3). These elements were chosen for method 2 because this model represented the skin as flexible without the ability to carry a bending load. These elements were analyzed with an explicit analysis method that will be discussed

later. For both of these methods, the forces imposed on the supporting structure were determined by the finite element analysis through Abaqus.

2.2.3.1. Load Profile Method 1

Load profile method 1 represented the spherical triangle as rigid such that its deformations were small. This meant that the concavity of the shape would remain unchanged under load representing a perfect sphere. It was necessary to model the surface with elements that could carry a bending load; hence, the shell elements. The surface was modeled as a stand-alone model without any support structure built in to the model. Since the simple supports were placed directly onto the surface, any supporting structure would have been rigid anyway. The nodal reaction forces were taken from all of the nodes along the perimeter of the triangle, these forces are shown in Figure 15 related to their position along each arc. The full surface model contained 741 elements. Segment A had a total of 50 nodes, segment B had a total of 41 nodes, and segment C had a total of 32 nodes. The orientation of these load profiles for all cases in this report will be oriented in the manner shown in Figure 14; the arc endpoint that is closer to the centroid will be oriented to the right. These forces divided by the element width, approximately 2 mm, provided a discretized plot of the load distribution in terms of Newtons per meter. A polynomial was then fit to the curve which would be used to reapply the forces to a set of elements in the ROM. This polynomial would apply the same load profile regardless of the number of elements in the applied model was different from that of the model the profile was taken from. These profiles are shown in Figure 16.

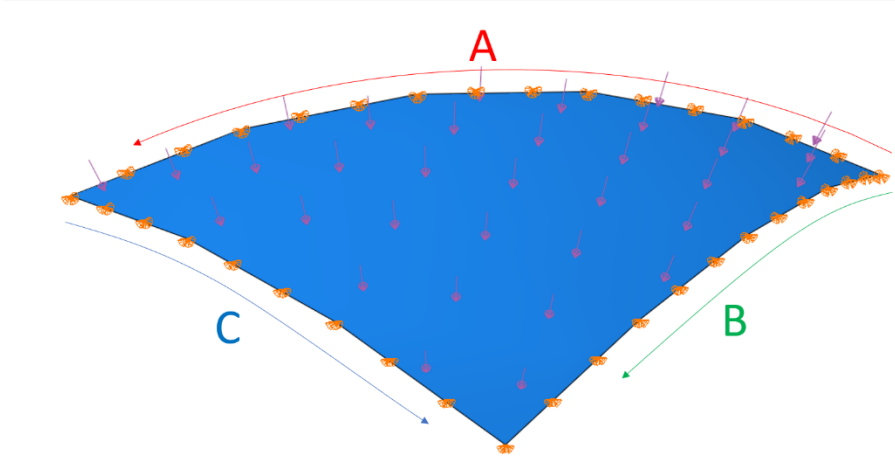

Figure 14: Load Distribution Orientations for Each Segment

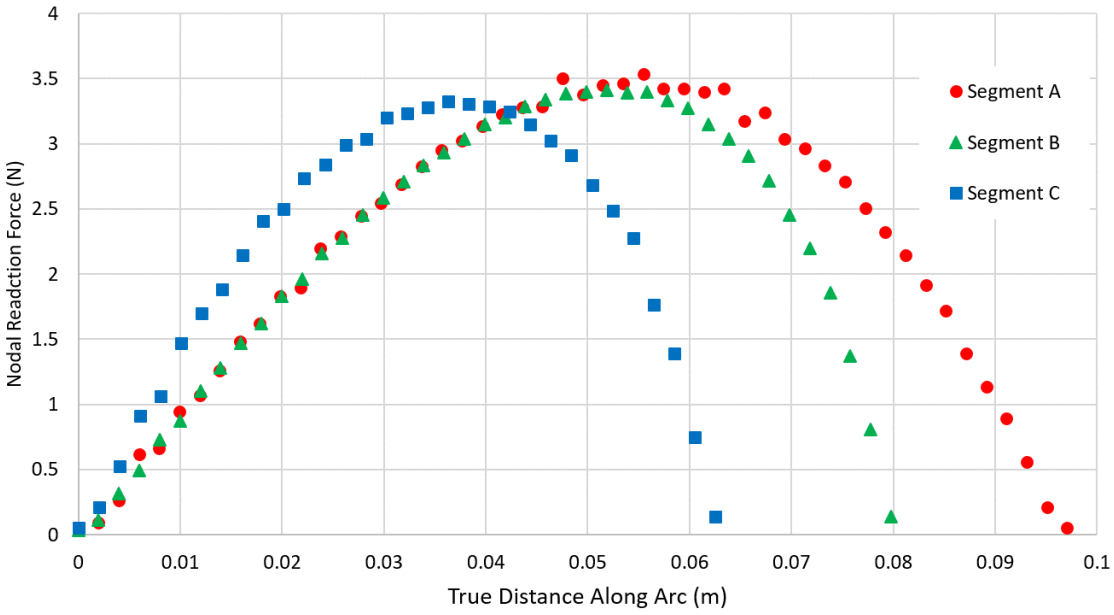

Figure 15: Nodal Reaction Forces of Method 1 Load Profile

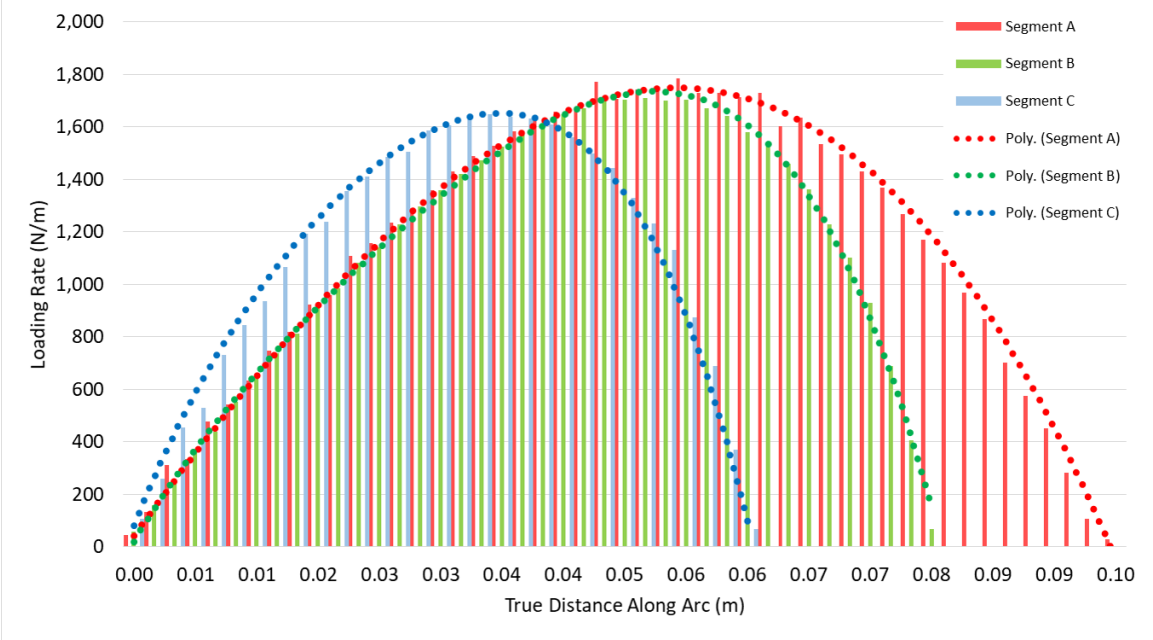

Figure 16: Discrete Load Profiles and Polynomial Fits for Method 1

The curves that were fit to the nodal data were done using Microsoft Excel's trend line tool using a polynomial fit. The equations of the polynomials fit to the load profiles for the rigid approach are shown in Equations (6), (7), and (8) for segments A, B, and C respectively.

$$F_A = -3.90E6x^3 - 1.86E5x^2 + 5.50E4x - 66.4 \quad (6)$$

$$F_B = -2.37E8x^4 + 2.49E7x^3 - 1.31E6x^2 + 6.96E4x - 114 \quad (7)$$

$$F_C = -5.11E8x^4 + 4.82E7x^3 - 2.67E6x^2 + 1.06E5x - 123 \quad (8)$$

These load profiles were then adjusted to be based on a spherical coordinates of radius and angle, θ, instead of a true distance along the curve so that they could more easily be applied with a spherical coordinate system as a line load to the FEA model. Abaqus does not allow a line load to be applied as a function of arc length which is how the positions of the nodal reaction forces were retrieved. This necessitates that the loading function be

transformed into either Cartesian or spherical coordinates to be reapplied to a model. Transforming the functions into Cartesian coordinates would have presented a significant challenge since the model that the function would be applied to may not necessarily be in the same orientation as the coordinate system of the model that generated the function. A function based on a distance x from an origin would need to be recalculated for each section that is at a different orientation. The simpler approach was to transform the original equations into a spherical coordinate system based on r, θ, and ϕ; with $\phi = 0$ for all loading schemes. This allowed the load to be applied by angle instead of an X-Y-Z coordinate. Each node was assigned a load rate based on its angle along its respective arc, a schematic is shown in Figure 17. This load rate would later be interpreted as a local pressure distributed over the width of the element.

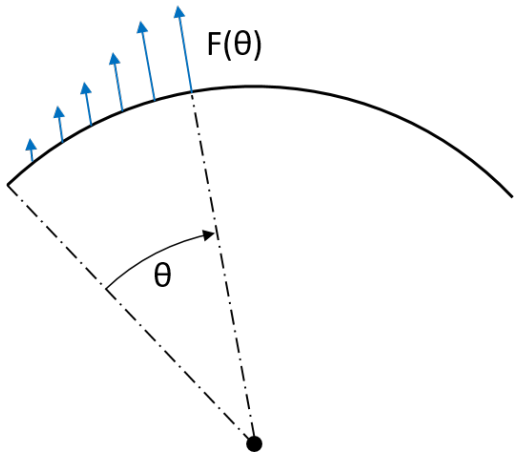

Figure 17: Schematic of Radial Loading Method

This transformation was done by replacing the true distance x in equations (6) through (8) with the equation for the arc length for a circle, θr. The radius in this case was the

structure's radius of 101.6 mm. The resulting equations are shown in Equations (9) through (11) for segments A, B, and C respectively.

$$F_A = -7.09E3\theta^3 - 19.2E3\theta^2 + 5.59E3\theta - 66.4 \quad (9)$$

$$F_B = -25.3E3\theta^4 + 26.1E3\theta^3 - 13.5E3\theta^2 + 7.07E3\theta - 114 \quad (10)$$

$$F_C = -54.4E3\theta^4 + 50.6E3\theta^3 - 27.5E3\theta^2 + 10.8E3\theta - 123 \quad (11)$$

To check the accuracy of the profile, integrating each equation across the respective segment arc length should result in the same value as the sum of the individual nodal forces taken from the original model; the nodal forces should demonstrate a good approximation for the polynomial. An example of this integration calculation is shown in Equation (12). The total of the three segments' integrals should also equal the total of all the nodal reaction forces. The results are shown in Table 8.

$$\int_0^{\frac{\pi}{4}} (-25.3E3\theta^4 + 26.1E3\theta^3 - 13.5E3\theta^2 + 7.07E3\theta - 114)rd\theta = 89.36 \quad (12)$$

Table 8: Comparison of Polynomial Fit to Nodal Forces

	Sum of Nodal Forces	Polynomial Fit	% Difference
Segment A	109.50	109.48	0.01
Segment B	90.00	89.36	0.71
Segment C	69.95	69.68	0.39
Sum	269.45	268.52	0.34

This check provided validation that the total force applied to the member with the polynomial approximation was the same as the sum of the nodal reaction forces. Even though the polynomial fit was applying a slightly lower load than the model's reaction forces total, the result is within half a percent and deemed a good approximation.

Load profile method 2 was based on a vector approach. Refer to Figure 18 as a visual representation of the following. Since the surfaces that the pressure is being applied to are not planar the pressure force acts in all different directions. The previous method simply superimposed the magnitudes of the pressure loads directly onto the structural members, A and B, as concentrated forces at the nodes in the desired direction. This would be an appropriate method if the surface was planar and rigid such that the pressure forces were all acting in the same direction, see Figure 18 (left). In reality the skin of the structure will be curved in a concave manner when the pressure is applied. Superimposing the pressure load onto the supporting structure as a concentrated force would likely result in a vector (shown in red) that is not necessarily in the radial direction (represented as dashed blue). This method also assumes that the superimposed force from the adjacent face will be equivalent and the resultant vector of the two vectors from adjacent faces will act in the radial direction, a representation of the adjacent face's force vector is shown in Figure 19.

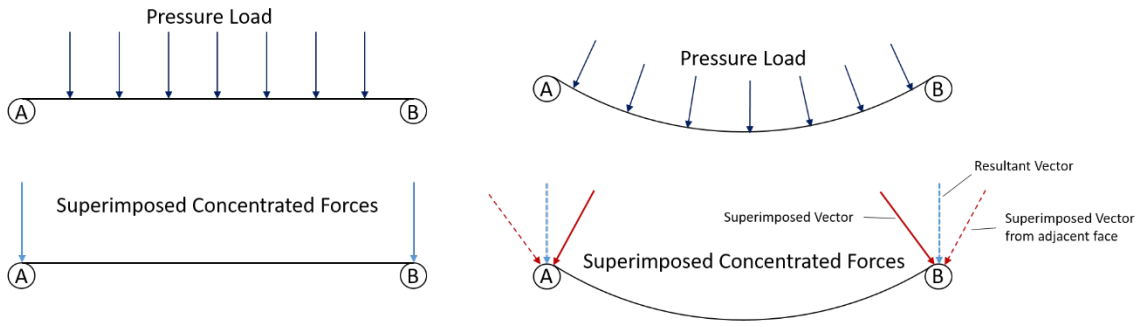

Figure 18: Superposition of Pressure Loads, Planar Face (left), Curved Face (right)

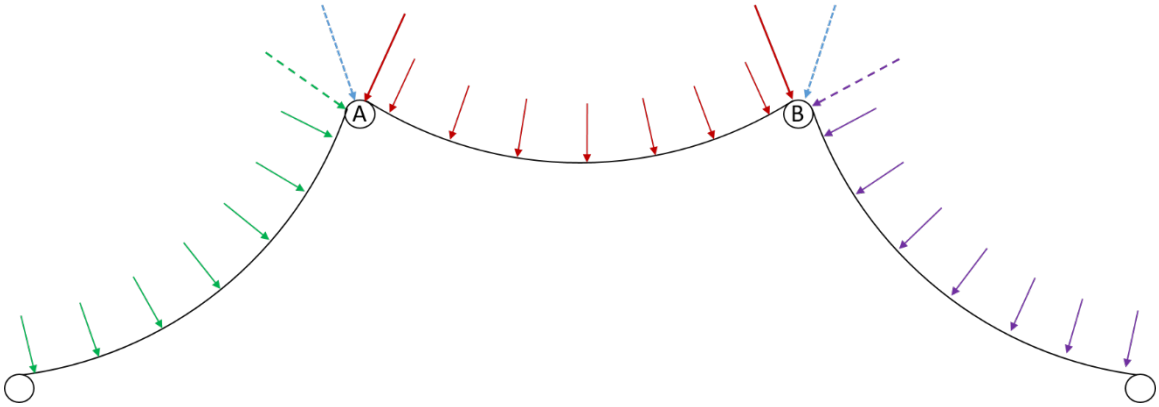

Figure 19: Adjacent Face Vector Representation

It was assumed that the components of the vectors acting against one another from adjacent faces would not significantly affect the structural members. This vector approach could have also been applied to the rigid triangle load profile method as the faces were also curved, this was not done as that method was created as a simple method. Likewise, the flexible membrane analysis could have been conducted with the magnitudes of the nodal reaction forces instead of taking the vector sums. To compare the difference between the vector sum and magnitude, plots of the load profiles taken both ways are included in Appendix A. If the original reaction forces had been in the radial direction, the two plots would be identical. Method 1 is based on the assumption that the analysis of the sphere is linear based on the original geometry. The actual behavior may be non-linear which requires a different approach to the problem. The results of the flexible triangle used in method 2 load profile versus the rigid triangle profile of method 1 will be discussed in Chapter 3.

2.2.3.2. Load Profile Method 2

The FEA for method 2 represented the flexible spherical triangle with membrane elements. This membrane was given the material properties of Mylar as this was a potential material of choice for the skin of the vehicle. Mylar films have a modulus of 5.001 GPa [20]. The thickness of the skin for the model was based on material availability. Three mil films (0.118 mm) were the thinnest film readily available. Unlike the previous model, the skin in this model was expected to deform such that the concavity of the triangular surface would snap to the inverse orientation. To accommodate this non-linear behavior, the type of analysis selected was a dynamic, explicit type. Although past researchers have successfully analyzed the nonlinear behavior of the skin in full celestial models with the use of the non-linear geometry selection and stabilization [12], the computational requirement began to become quite cumbersome as the minimum time increment used was 10^{-36} for a maximum of 10^{8} increments [21]. Attempts to run the analysis with slightly larger increments often resulted in errors citing a lack of convergence or requirement for a smaller step size. Alternative methods, such as explicit methods, were explored that could better handle the large non-linear displacements of the skin. The explicit dynamic analysis is described as follows by the Abaqus manual:

> An explicit central-difference time integration rule is used; each increment is relatively inexpensive because there is no solution for a set of simultaneous equations. The explicit central-difference operator satisfies the dynamic equilibrium equations at the beginning of the increment, t; the accelerations

calculated at time t are used to advance the velocity solution to time $t + \frac{\Delta t}{2}$ and the displacement solution to time $t + \Delta t$. [18, 6.3.3-1]

The explicit analysis can better handle the non-linear behavior that is exhibited by the snapping behavior of the skin since it does not seek convergence at every increment. The displacements are known quantities at the beginning of each increment and are not solved for during each increment. This method was expected to produce results in a much shorter time frame than using the implicit technique with stabilization. To account for the dynamic effects of the loading, the analysis was run for 3 seconds with the load being applied as a ramp input over 1 second. The snapping behavior describes the rapid switch in concavity of the curved members. This phenomenon is described in Figure 20 where if the force, F, becomes great enough the curvature of the shape will switch from position A to B. This can occur in beams as well as surfaces such as the skin applied to this structure.

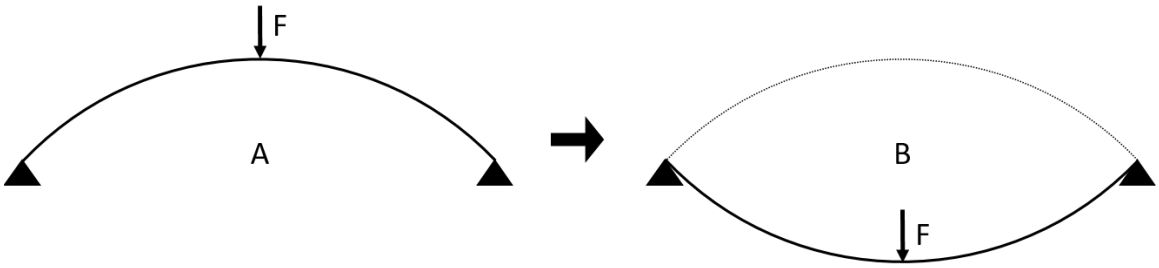

Figure 20: Snapping Schematic

The mesh for this analysis consisted of linear quadrilateral membrane elements (M3D4R) seeded with an element size of 1 mm. This produced a mesh of 2854 elements

with 2975 nodes shown in Figure 21. This model was also simply supported along the perimeter with a sea-level pressure of 101.325 kPa applied to the surface.

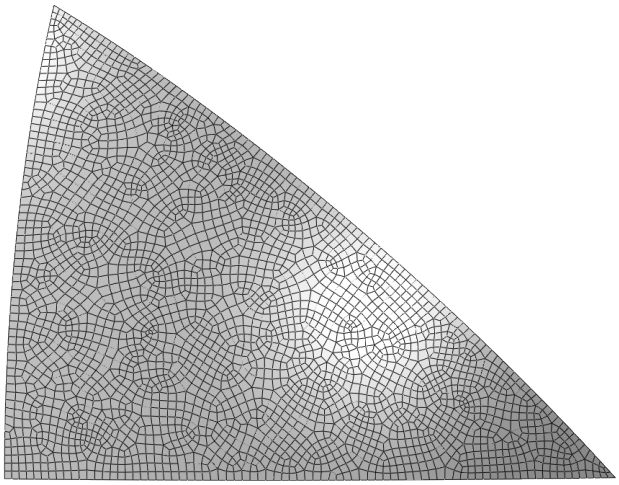

Figure 21: Mesh for Load Profile Method 2

The nodal reaction forces were taken as the three Cartesian directional components RF1, RF2, and RF3. These forces were used since the interface to visualize the deformed model was restricted to using a Cartesian coordinate system. If the forces could have been resolved directly into a spherical coordinate system the following vector discussion would not have been necessary as the radial forces could have been taken directly. The Cartesian forces make up the three vector components of the magnitude force vector, F. As discussed previously, the skin's surface is curved and the pressure forces act as follower forces that move with the deformations to remain perpendicular to the surface; therefore, the reaction forces acting on the nodes are not necessarily going to be in the radial direction and could be in any direction necessary to reach equilibrium. This

reaction force F has a complimentary force from the adjacent triangular surface. The symmetry for this geometry assumes that the resultant vector from the sum of the reaction force vectors will be directed in the radial direction. Instead of modeling both faces adjacent to any given member, the force vector from one face was projected onto the radial position vector to determine half of the resultant vector in the radial direction; this is the direction the loads would later be applied to the structural members. This force vector would have to be doubled later to account for the contributions of both faces. The vector projection can be found by taking the dot product of the force vector with the position unit vector or the dot product of the force vector with the position vector divided by the magnitude of the position vector. The vector projection is described in Equations (13) and (14) and represented in Figure 22.

$$f_r = F \cdot \hat{u} = \frac{F \cdot u}{\|u\|} \tag{13}$$

$$f_r = \frac{x * RF1 + y * RF2 + z * RF3}{\sqrt{x^2 + y^2 + z^2}} \tag{14}$$

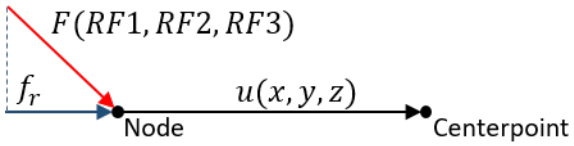

Figure 22: Vector Projection Schematic

Where f_r is the nodal radial force, F is the reaction force vector, $\hat{u}$ is the positional unit vector of u with components x, y, and z from the origin as the center of the sphere. Once the radial forces were determined, the process for developing the load profile polynomial was the similar to the method previously discussed. The benefits of this method will be

discussed in Chapter 3. The radial nodal reaction forces are shown in Figure 23 and along with the load profiles and polynomial fits in Figure 24.

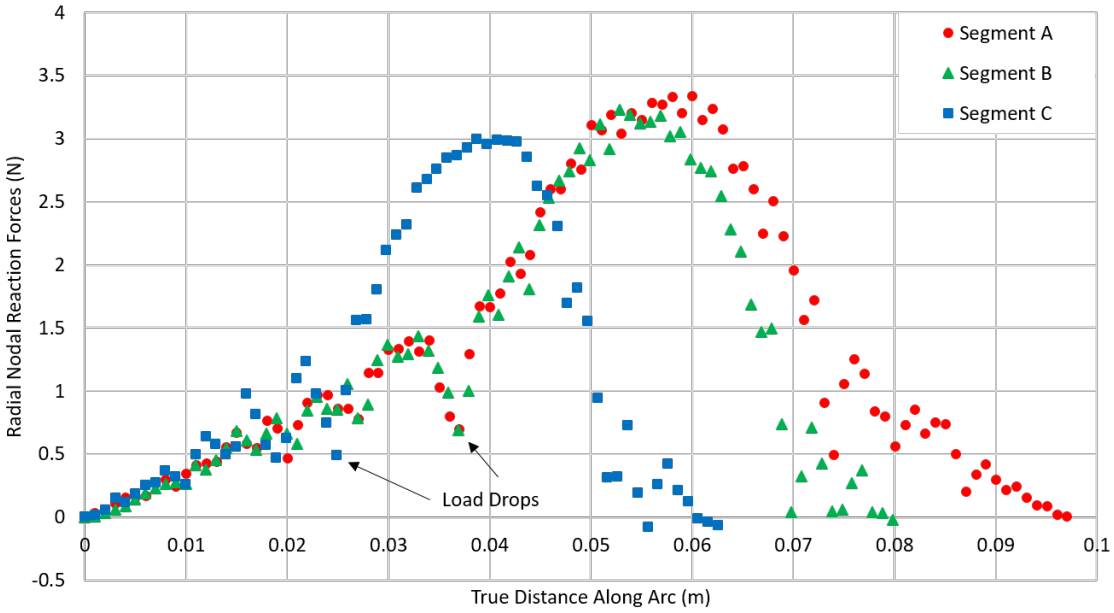

Figure 23: Nodal Reaction Forces of Method 2 Load Profile

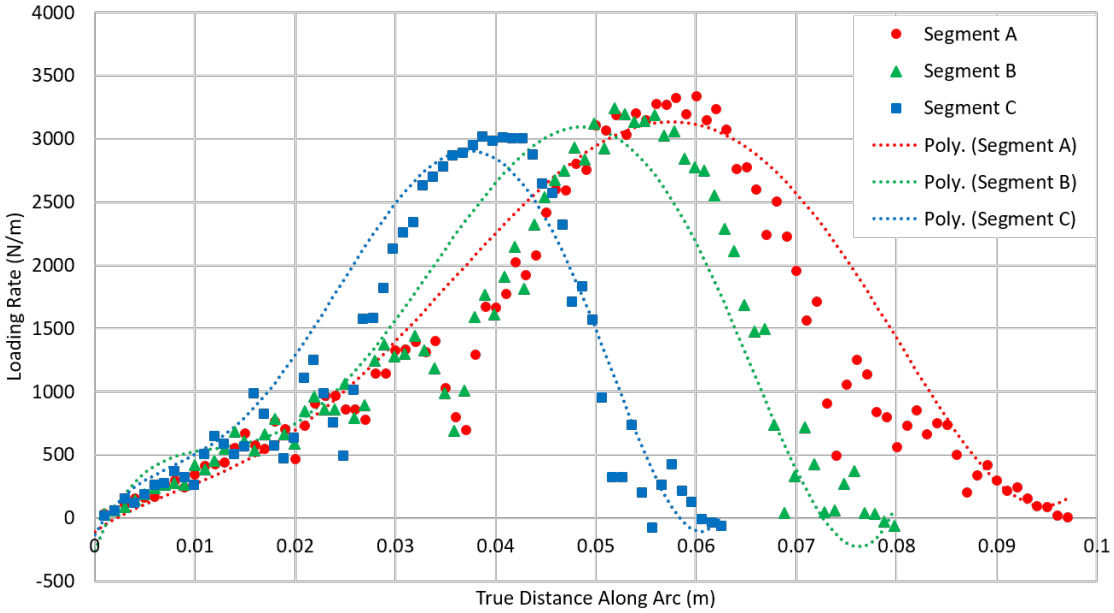

Figure 24: Discrete Load Profiles and Polynomial Fits for Method 2

The polynomial fits to the curves were determined by first applying a smoothing algorithm to the data. This algorithm consisted of a 4-point average using 1 prior and 2 ahead of the given data point. A key point of interest in the reaction forces is the sudden drops in the reaction forces on the slopes of the arcs as identified in Figure 23. These drops in load correspond to wrinkles in the surface of the membrane that can be seen in Figure 25.

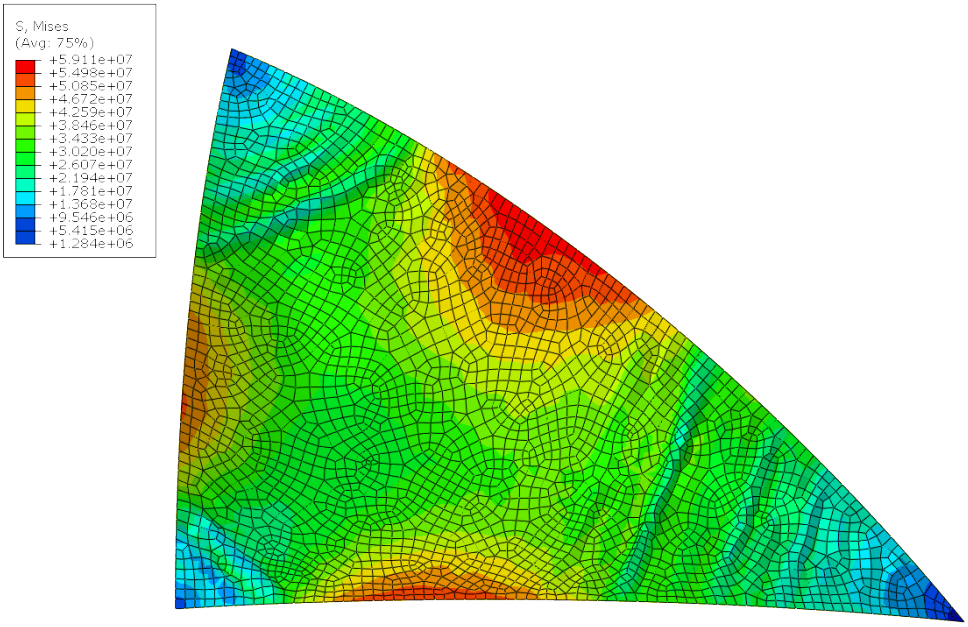

Figure 25: Deformed State of Flexible Triangle with Wrinkles

It is unclear if the wrinkles were an artefact of the modeling process or a real product of the geometry, but in either case these drops were smoothed over for the purposes of the load profile. The equations for the load profiles developed using this method in terms of true distance along the arc are shown in Equations (15) through (17).

$$F_A = 1.44E10x^5 - 2.98E9x^4 + 1.83E8x^3 - 3.44E6x^2 + 5.72E4x - 111 \quad (15)$$

$$F_B = 7.20E10x^5 - 1.34E10x^4 + 8.13E8x^3 - 1.90E7x^2 + 1.99E5x - 258 \quad (16)$$

$$F_C = 1.61E11x^5 - 2.25E10x^4 + 9.94E8x^3 - 1.57E7x^2 + 1.43E5x - 132 \quad (17)$$

In the same fashion that was discussed for the rigid triangle of load profile method 1, the original polynomial equations based on arc length were transformed to be based on the angle theta of a spherical coordinate system. This was done by replacing x with $r\theta$ with r

being the structure radius of 101.6 mm. The resulting equations are shown as Equations (18) through (20).

$$F_A = 1.55E5\theta^5 - 3.17E5\theta^4 + 1.92E5\theta^3 - 3.54E4\theta^2 + 5.81E3\theta - 111.4 \quad (18)$$

$$F_B = 7.80E5\theta^5 - 1.42E6\theta^4 + 8.53E5\theta^3 - 1.96E5\theta^2 + 2.025E4\theta - 257.6 \quad (19)$$

$$F_C = 1.75E6\theta^5 - 2.40E6\theta^4 + 1.04E6\theta^3 - 1.62E5\theta^2 + 1.45E4\theta - 131.9 \quad (20)$$

These equations can be similarly integrated as in Equation (12) to determine the total radial force to be applied through the load profile compared to the total radial nodal forces of the model. These results are shown in Table 9.

Table 9: Comparison of Polynomial Fit to Nodal Forces

	Sum of Nodal Forces	Polynomial Fit	% Difference
Segment A	129.0	149.6	15.57
Segment B	103.6	108.2	4.39
Segment C	75.9	85.1	12.04
Total	308.6	334.2	8.31

The polynomial fits for this case add a significant amount of load compared to the nodal forces from the model, over 8%. Much of this difference can be attributed to the wrinkles causing load drops. Ideally there would not be wrinkles in the skin of the vehicle as this would have negative aerodynamic effects as well as the potential to damage the skin. A smoother polynomial fit is assumed to adequately represent the load distribution for this case. It will be shown in later sections that this stresses produced by this load profile applied to the full celestial structure more closely matches the stresses from the skin-and-structure model.

To compare differences in the three load profiles discussed they were overlaid on eachother in Figure 26 with segment A in the top plot, segment B in the middle plot, and segment C on the bottom plot. For segments A and B, the geometric method and the rigid triangle method show similar profile while the flexible triangle method produced a much greater peak load. For segment C, the geometric method and flexible triangle method show similar profiles while the rigid triangle method produced a much lower peak load. It is important to point out that these load profiles represent only half of the load to be applied to the members. Since these load profiles are the contribution of a single triangular face onto each triangle segment supporting that face and each segment divides two faces, the load profile must be doubled when applied to a member for analysis.

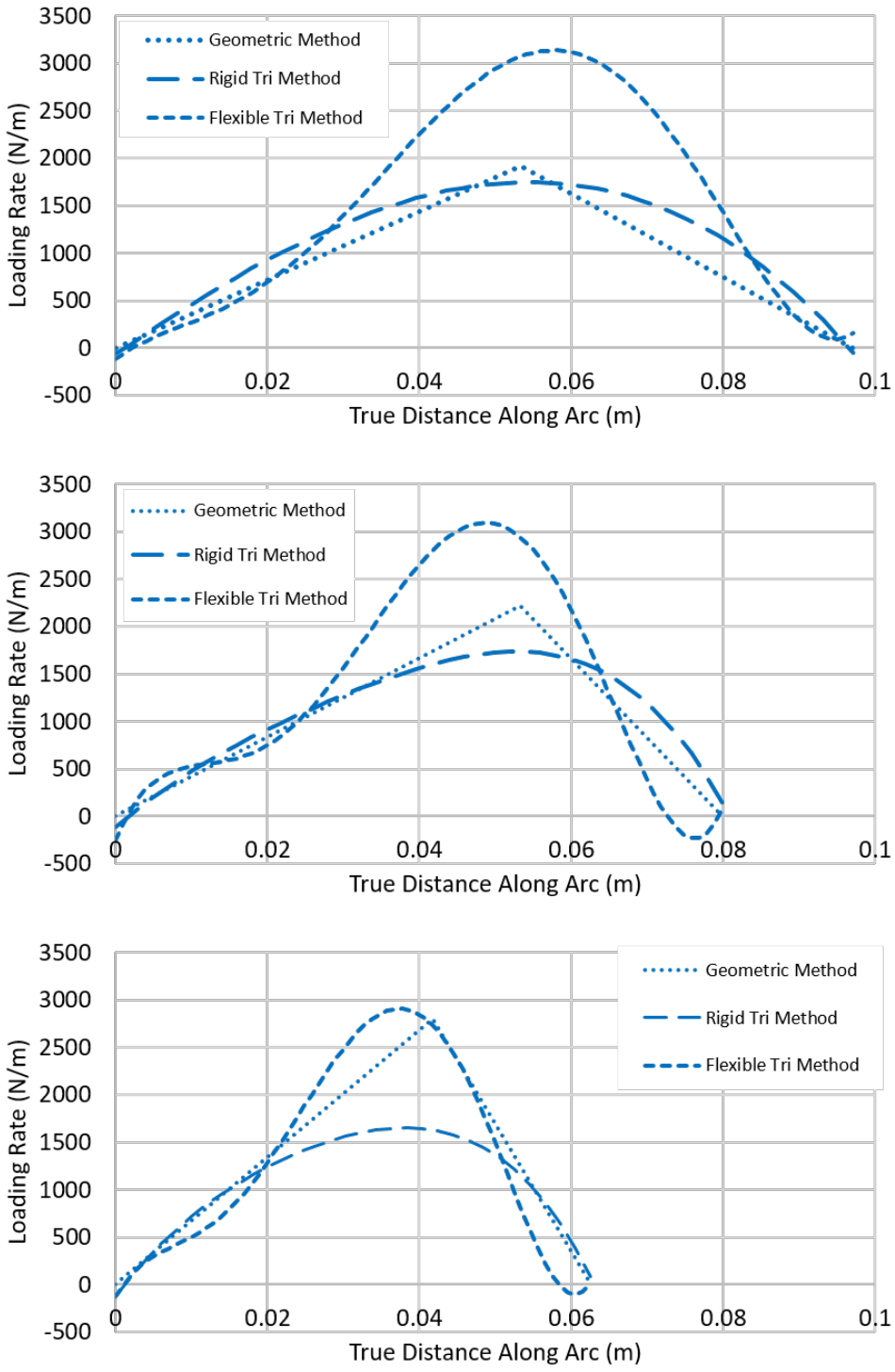

Figure 26: Combined Load Profiles, Segments A (top), B (middle), and C (bottom)

2.2.3.3. Reference Point Load Distribution Method

A method that has been used by past researchers to distribute the pressure loads was the reference point (RP) method. This method uses an equivalent concentrated force positioned at the centroid of a given area along with a coupling constraint in place of a pressure load. This method has the potential of simplifying the load application process. Loading in this manner does not involve the use of a follower function for the load as the skin deforms meaning the load will always be directed toward the center of the structure. This method was first explored in this research when the bare frame celestial model was created. The process of applying a line load to all 72 beam sections individually was proving to be quite tedious. The model was run under different conditions which resulted in the structure collapsing under supposedly the same load as the line load method which did not demonstrate a collapse. This method was investigated to determine the exact loads that were being distributed to the celestial structure; this method was ultimately not used as the load profiles that were generated were fundamentally inconsistent with the other methods. The reason for this is a combination of the geometry and method of load distribution. Abaqus allows the user to choose between uniform, linear, cubic and quadratic distributions. The choice of load distribution method changes how the loads are applied, but are all essentially based on the distance from a reference point. A detailed description of the reference point method can be found in Adorno-Rodriguez' work [10], but for the purposed of this research only the selected parameters will be described. This analysis utilized the same shape as the curved triangular surface, but only represented the perimeter of the triangle as beams and did not model the surface itself. These beams were

directly supported and only served as a structure to attach the constraints to. The reference point was chosen as the centroid of the curved surface and is shown in Figure 27 along with the representation of the constraint. The constraint was a coupling constraint with continuum distributing and all six degrees of freedom constrained. The influence radius was designated to be out to the further point of the model such that the entire shape would be considered for load distribution.

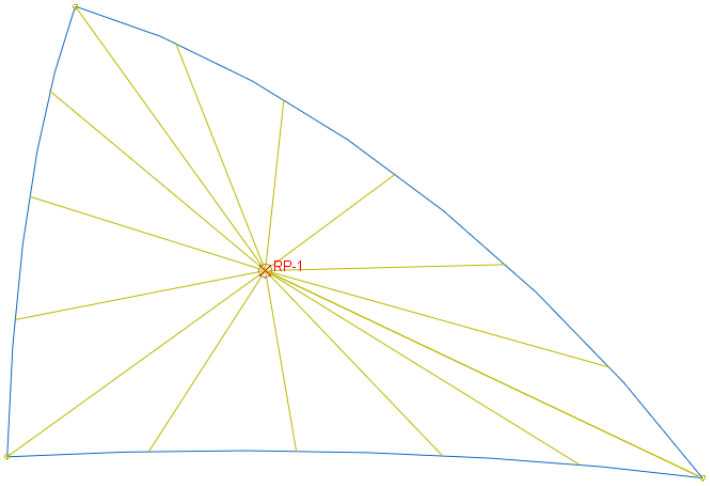

Figure 27: Reference Point Method Coupling

Each of the four load distribution options were each chosen and evaluated with a concentrated force of 273.15 N placed at the reference point directed toward the sphere's center. This force was the equivalent concentrated force resulting from the pressure applied to this surface area. The resulting load distributions are shown in Figure 28. While none of the load distribution methods reached the same peak as the flexible triangle method, this was not the reason for discounting the method as this peak was also much higher than the results from the rigid triangle method. In fact, the load distributions

obtained with the RP method do resemble the distributions obtained with the rigid triangle method with the exception of the loads near the end points. The RP distributing method in Abaqus appears to be based on distance from the reference point, without taking into account the geometry of the coupling. The closest nodes receive the higher loads and the points furthest from the loading point receive loads of zero, or near zero. The exception to this was the uniform distribution method. This means that both vertex points of segment C have non-zero loads for all cases that are as high as 1000 N/m for the quadratic distribution method. This was not observed for either of the cases where a pressure load was applied to the triangular surface. This is an artefact of the loading face being a scalene triangle. In the case of the simple icosahedron where the triangles are equilateral, all the vertices are the same distance from the centroid and would receive zero loads, or near zero loads. In the case of a scalene triangle, there is only one point that is furthest from the loading point. The zero load at the vertices was present for the geometric method and the nodal reaction forces through the FEA methods and is a crucial feature of the load profiles. This zero load is necessary not only because it is where the geometry comes to a point and thus presents a lack of loading surface, but also because it is where other members intersect. The compounding effect of multiple non-zero loads at an intersection can produce an excessively large load where there ought not be. For example, the right side end point loads for segments B and C shown in Figure 28, add up to a loading rate of approximately 3600 N/m at the 2-ring intersection when modeled together. This loading rate is almost double that of any other peak rate within the structure for this analysis. This makes a significant impact on the way the load is applied

to the structure. The polynomial fits from the other load profile schemes did not have exactly zero load rates at the end points, but they were considerably small compared to the peaks of the profiles. Selecting a point that was equidistant from each of the vertices may have produced a better result, however this was not explored.

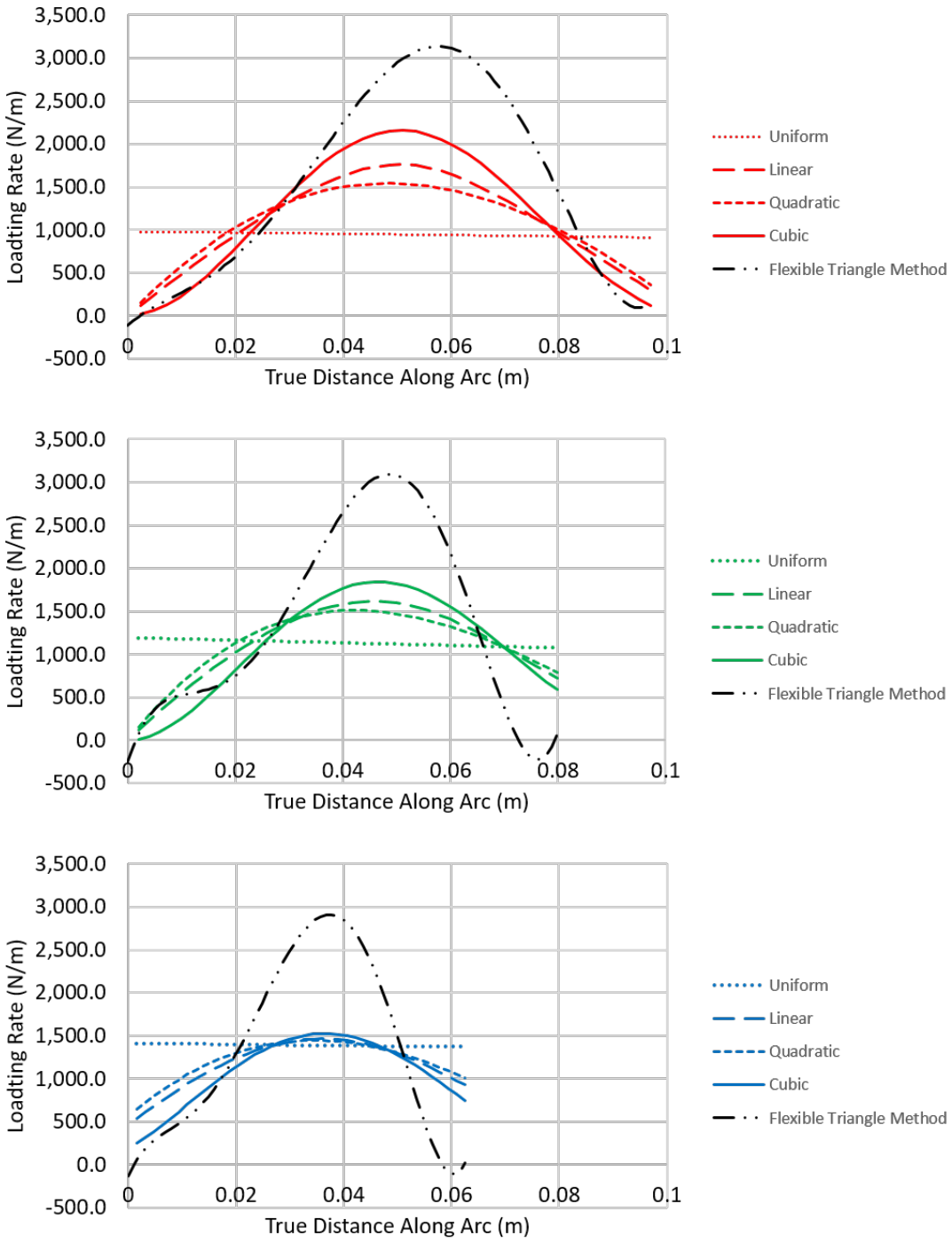

Figure 28: RP Load Profiles, Segment A (top), Segment B (mid), Segment C (bot)

2.2.4. Beam Geometry and ROM Process

The process for determining the celestial icosahedron beam diameter using the ROM method discussed previously is as follows:

1. Select a total structure diameter, and starting beam geometry
2. Model the characteristic triangle as a surface, simply supported along the perimeter and apply an applicable pressure
3. Obtain the nodal reaction forces from the surface model and generate the load profiles
4. Model the three 2-segment arches as discussed in section 2.2.2 to obtain the boundary condition spring constants
5. Model each of the three triangle segments according to the ROM with the determined spring constants and load profiles
6. Evaluate which of the three segments had the largest stress
7. Modify beam geometry based on the maximum allowable stress and repeat steps 4-7 until convergence

This process would hold for any beam geometry that could be designed; however, the design used throughout this research was a solid circular cross-section. The remainder of the ROM discussion are based on the circular cross-section members.

2.2.4.1. Total Structure and Arches

Theoretically, the ROM process could be applied to a celestial icosahedron of any size. The total structure diameter would be selected based on the desired application and payload. Analysis done by Moore showed that a celestial icosahedron shape could reach

neutral buoyancy at a diameter of 0.8001 meters and could have a weight to buoyancy ratio of 0.7257 at 1.2192 diameter [12]. These calculation were done with material properties of carbon nanotubes and graphene. Regardless, a lightweight structure capable of supporting a vacuum and close to neutral buoyancy would be a tremendous step forward for VLTAVs. The total structure diameter is defined as the diameter of the outer mold line of the vehicle if it were a perfect sphere. This dimension is shown in Figure 29; the diameter used for this research was 0.2032 m to meet 3-D printing requirements. The arches that make up the triangular shapes can be defined by their sweeping angle and radius. These arch angles are shown in Figure 29.

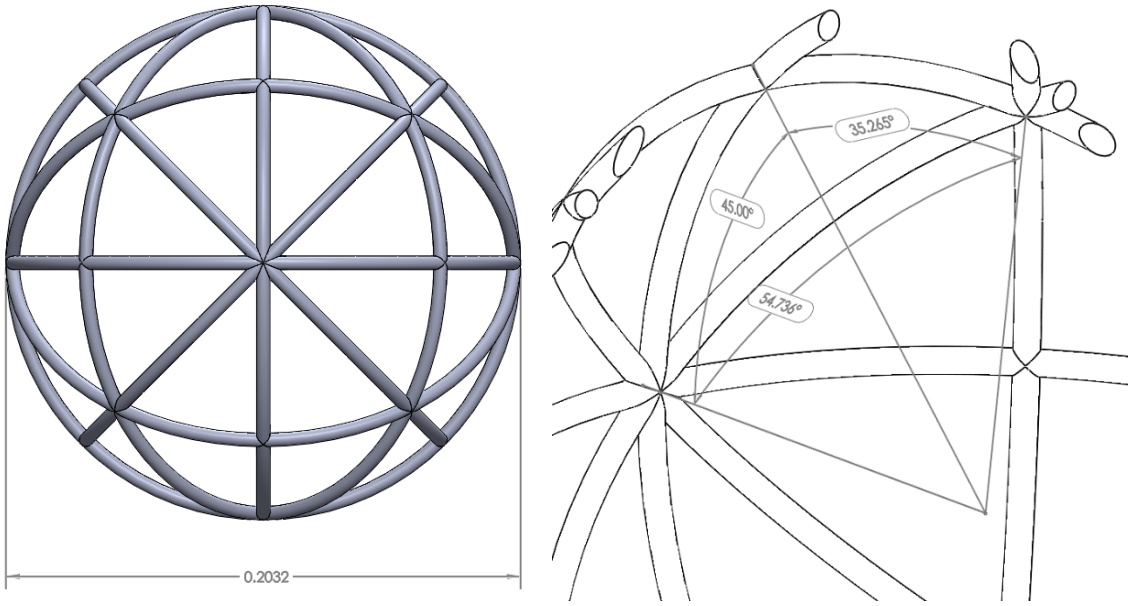

Figure 29: Celestial Icosahedron Outer Diameter (left), Arch Angles (right)

2.2.4.2. ROM Beam Loading Method

The load profiles for the ROMs were based on the load profiles generated by the methods described in section 2.2.3. This produced three distinct load profiles that would

be used for each of the three triangle segments. This load represents the radial force imposed by the pressure load on the individual beams themselves. After the beams were modeled per section 2.2.1 with the required boundary conditions a load was applied as a function of θ, the sweeping angle. This loading equation was entered into Abaqus as a line load with an analytical field. The analytical field describes the equation for the load profile. This load profile was then distributed to each of the nodes in the following fashion: The angular position of each node is determined with respect to the given coordinate system; the loading rate is calculated based on the angle; the loading rate is multiplied by the element width to determine the discrete nodal load. This is described in Equation (21)

$$F_{Node} = P(\theta) * width_{elem} \tag{21}$$

Where P is the loading profile as a function of θ. This method does require that the number of elements across the span of a member be sufficient to accurately map the load profile. An example of how the element width can affect the total load applied is shown in Table 10 for seeded element widths of 20, 10, 5, 2 and 1 mm and the integrated solution.

Table 10: Effect of Element Width on the Total Force on Segment A

Element Width	20 mm	10 mm	5 mm	2 mm	1 mm	Integral
Total Force	101.2	106.4	107.6	110.4	109.4	109.48

The element widths referred to are described in Figure 30. This is the distance that Abaqus attempts to space out the nodes between elements when filling a given geometry with elements if the element width is not an exact multiple of the geometric distance,

adjustment will be made to a few elements to fill the remaining space. The smaller the element width, the more nodes that the profile function has to match the load profile to. It would not be significantly beneficial to have an element size less the 1 mm as this element size very nicely represents the loading profile. The 2 mm element width also provides a good representation of the loading scheme; this element width was used for the ROM and full celestial models.

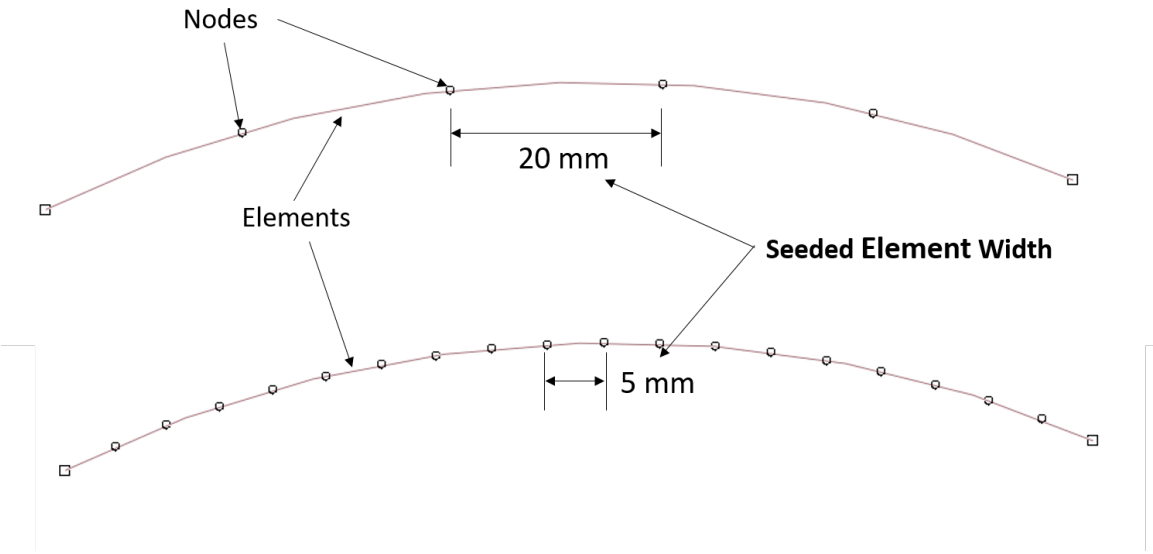

Figure 30: Element Width Representation for Beam Elements

2.2.4.3. Beam Geometry Adjustments

Complex beam geometries can complicate the process of adjusting the beam geometry as there may be more than one variable to adjust such as diameter and thickness for annulus shaped cross-sections. For this research only circular cross-sections were investigated. The ratio of the observed maximum stress to the maximum allowable stress compared to the ratio of the original cross-section to the unknown new cross-section can

be solved to determine the cross-section necessary to produce the maximum allowable stress. This method is shown in equations (22) through (24).

$$\frac{\sigma_{ult}}{\sigma_{max}} = \frac{A_{orig}}{A_{new}} \tag{22}$$

$$\frac{\sigma_{ult}}{\sigma_{max}} = \frac{\pi R_{orig}^2}{\pi R_{new}^2} \tag{23}$$

$$R_{new} = \sqrt{R_{orig}^2 * \frac{\sigma_{max}}{\sigma_{ult}}} \tag{24}$$

Where σ_{ult} is the maximum allowable stress, σ_{max} is the maximum stress that occurred within the model, R_{orig} and A_{orig} are the original cross-sectional radius and area. The A_{new} and R_{new} are the new beam cross-sectional area and radius which are the variables to be solved for. This method assumes the relationship between the beam radius and stress is linear. In the case of a non-linear relationship, the process may need more than one iteration to converge on the required beam diameter.

The type of stress being evaluated for this study is the Von Mises stress which takes into account both the bending stresses and the axial stress shown in Equation (25).

$$\sigma_{mises} = \frac{Mc}{I} + \frac{P}{A} \tag{25}$$

Where M is the bending moment, c is the distance from the neutral axis (beam radius), I is the area moment of inertia, P is the axial force, and A is the cross-sectional area. Depending on the manufacturing process and limitations, it is theoretically possible for each of the members to have a different beam diameter that maximizes the allowable stress to reduce the structure's weight as much as possible. For this research, a single

beam diameter was chosen for the entire structure and a stress of 42 MPa [15] was used for the ultimate stress throughout the structure.

2.2.5. Beam Buckling Analysis

As an additional check on the beam geometry produced by the ROM a buckling analysis was done. The method was taken from the author Pilkey for uniformly loaded curved beams under various support conditions [23]. The support conditions that most closely represent that of the ROM were the clamped-radially guided boundary condition. Equations (26) and (27)(14) were used to determine the critical buckling load for the curved beam.

$$P_{cr} = \frac{EI}{R^3}(K^2 - 1) \tag{26}$$

$$K * \tan\left(\frac{\psi}{2}\right) * \cot\left(\frac{K\psi}{2}\right) = 1 \tag{27}$$

Where E is the material modulus of elasticity, I is the cross-sectional area moment of inertia, R is the arc radius, ψ is the total angle of the arc as illustrated in Figure 31, and K is a constant that must be solved for.

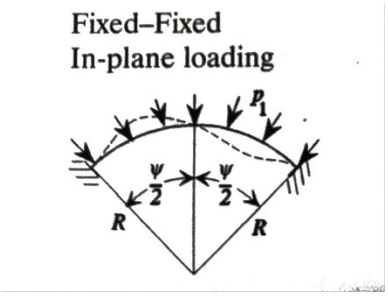

Figure 31: Representative Loading Scheme for Curved Beam [23]

For this analysis, only the dimensions of segment A will be used as this is the longest member and therefore most likely to buckle. The value of K for segment A was determined to be 9.443. The modulus used for this calculation was the flexural modulus for Ultem 9085, 2050 MPa [15]. The results of this equation for various beam radii used throughout this research are shown in Table 11 along with the factors of safety (FS) for each of the load profiles. The load profile peaks are two times the peaks shown previously in Figure 26 on page 46 as this is how they would be applied due to symmetry. These load peaks were 3495 N/m and 6189 N/m for load profile 1 and 2 respectively.

Table 11: Critical Buckling Loads for Curved Beams

Radius (mm)	P_{cr} (N/m)	Load Profile 1 FS	Load Profile 2 FS
2.38	4343	1.24	0.70
2.64	6575	1.88	1.06
2.99	10819	3.10	1.75

Table 11 shows that had load profile 2 been applied to the structure of beam radius 2.38, at least beam segment A would have buckled since the factor of safety (FS) is less than 1. For all other cases, there is a FS greater than 1 for beam buckling.

2.3. Finite Element Analysis for Full Celestial Icosahedron Modeling

Modeling the full celestial icosahedron served two purposes for this research. First, modeling the full structure provides a method of validating the results from the ROM. Second, the full structure model was compared to experimental results to determine the effectiveness of the model. Since the beam geometry chosen was a simple circular cross-section, the model for the full celestial could be made and analyzed without excessive difficulty. The intention was to make sure that ROM was accurately predicting

the stresses and behavior within the members so that a full-scale model with complex beam geometry would not be necessary. These models represent the material as a homogeneous isotropic material, even though this is not the case for 3-D printed Ultem 9085. The full model largely follows the same procedure as Moore did during his analysis of the celestial icosahedron [12]. The full celestial model was evaluated in two parts; with and without the skin. The structure of the celestial was made of B32 beam elements while the skin in the model that included the skin was modeled with M3D3 and M3D4R elements. The M3D3 and M3D4R elements which are are triangular and quadrilateral membrane elements. These elements were used by Adorn-Rodriguez and Moore with great success in their models of the icosahedron and the celestial icosahedron. The modulus used for the model of the full celestial frame was 2.373 GPa, which was the average modulus taken from the experiments of Greenoe [14].

2.3.1. FEA of Bare Frame Celestial Icosahedron

The model without the skin was done similarly to how the analysis of the icosahedron was done by Adorno-Rodriguez; however, the loads were applied as line loads directly onto the structural members as opposed to using a reference point method. The explanation for not using the reference point method for this structure can be found in section 2.2.3.3. The boundary conditions chosen for this analysis was clamped at the bottom vertex preventing both displacements and rotations (U1=U2=U3=UR1=UR2=UR3=0). The boundary at the top vertex allows the structure to deform in the U2 direction but not translate in the U1 or U3 directions (U1=U3=0). The modelled icosahedron bare structure is shown in Figure 32. This model contained 1128 or

2808 B32 elements with a seeded element width of either 5mm or 2mm. The analysis was run as a static, general step with an initial step size of 1E+5, a minimum of 1E+8, for a time step of 1. Ultimately both the rigid and flexible triangle load profiles were used on this model; however, at the time the celestial frame needed to be 3-D printed, only the rigid triangle profile had been fully explored. As a result, the load profile of the rigid triangle method was the one that ultimately determined the beam radius for the 3-D printed model.

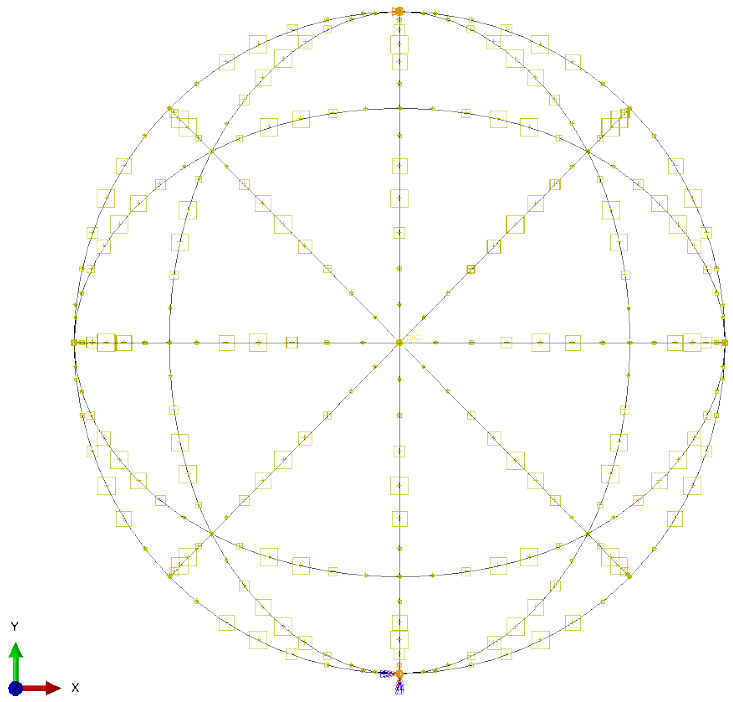

Figure 32: Bare Celestial with Line Loads and Boundary Conditions

2.3.1. FEA of Celestial Icosahedron and Skin

The model of the celestial icosahedron with the skin was generated in the same way as Moore and Graves produced their models [12]. The structure was the same structure used for the bare structure modeling as described in section 2.3.1. The skin was made using a revolve option in the Abaqus CAE part building interface. This option allowed a half-circle to be revolved around an axis to produce a spherical surface. This surface was then partitioned by each of the planes of the nine individual rings. This partitioning allows the mesh to be aligned with the substructure. The element mesh of the skin was generated using a seed width of 4 mm and consisted of 8875 M3D3R and 296 M3D3 elements. The mesh over the partitioned sphere is shown in Figure 33.

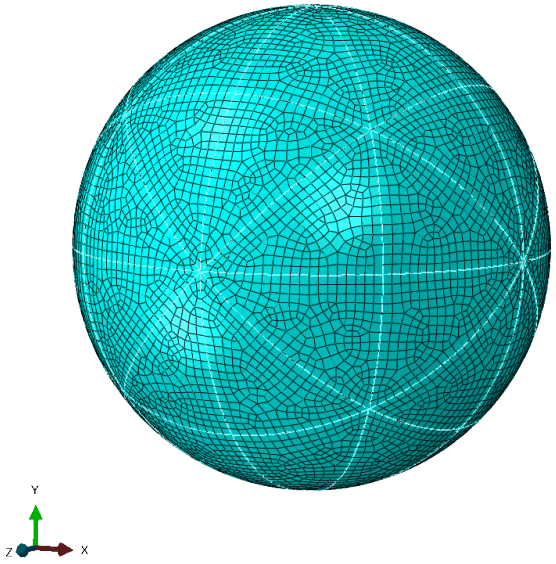

Figure 33: Partitioned Skin Mesh

A tie constraint was used to connect the substructure and skin and only connecting the displacement degrees of freedom. This method of connecting the skin and structure has

been used by previous researchers. A potential drawback to using this method of attachment along with beam elements is the beam profile is not accounted for. For shapes such as the icosahedron this results in a sharp point occurring in the geometry which causes singularities at these points [10]. Similarly, the beams themselves are represented as lines and may cause singularity effects due to a sharp edge. The analysis of the models with the skin were run similar to the flexible triangle analysis for the load determination as there were now 48 of these skin sections undergoing large nonlinear displacements. The analysis was run as a dynamic, explicit step with non-linear geometry as described in section 2.2.3. The load applied to the model was a uniform pressure load of 101.325 kPa applied to the skin's surface, representative of sea level pressure, as a ramp from 0 to 1 seconds. This analysis was done over a 3 second time period to allow the dynamic response to dampen out to a steady state. The boundary conditions were changed for this model to better assess the structure for symmetry. Restricting the movement of the lower vertex prevented the natural displacement of that vertex in the U2 direction. This movement would be manifested by displacing the entire structure upward which distorts the movement caused by the pressure load. To overcome this, boundary conditions were placed at every 4-ring intersection preventing tangential movement. This essentially locked each of these vertices onto an axis and locked the entire sphere onto its center point. These boundary conditions are shown in Figure 34. The vertices along the Y-axis such as point A are constrained in the x and z-directions (U1=U3=0), the vertices along the X-axis such as point B are constrained in the y and z-directions (U2=U3=0), and the vertices along the Z-axis such as point C are constrained in the x and y-directions

(U1=U2=0), reference Figure 34 for the full view and a close-up of the boundary conditions at point A. This configuration allows for the assumed natural movements of the structure without favoring any one direction so that the displacement magnitude data would not be skewed in one direction or another. The load was applied as a uniformly distributed pressure to the surface of the skin.

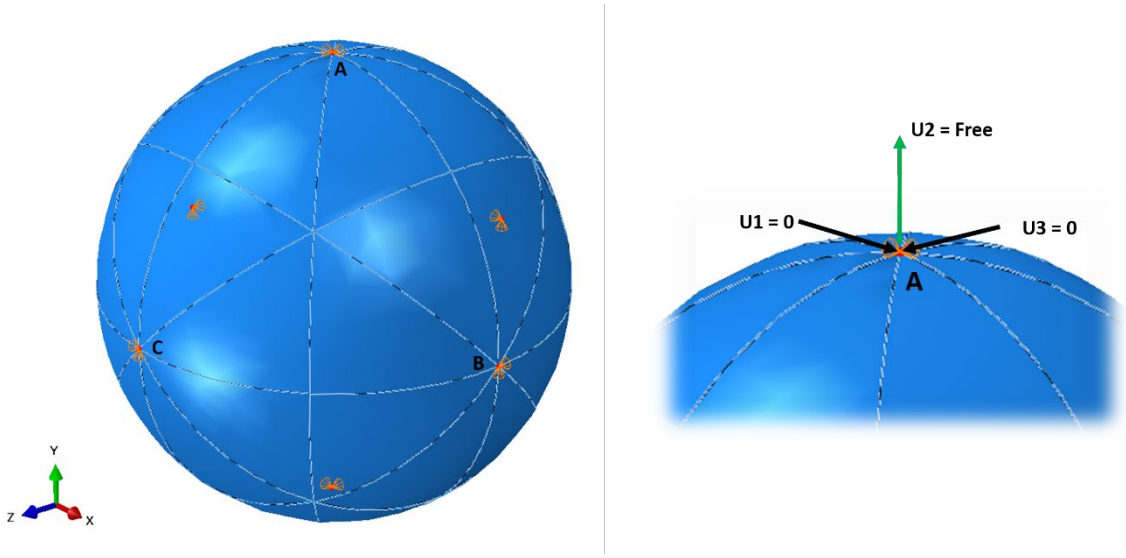

Figure 34: Boundary Conditions for Celestial with Skin (left), Close-up of A (right)

2.3.2. FEA of the Celestial Icosahedron for Compression Testing

The same model that was described in section 2.3.1 was also used with a different loading scheme to serve as a comparison to the experimental testing. This analysis would simply replace the line loads applied to each of the members with a single concentrated load at the top most vertex. The representation is shown in Figure 35 with boundary conditions. The boundary conditions selected for this analysis were clamped at the bottom (U1=U2=U3=UR1=UR2=UR3=0) and clamped rotations and fixed tangential

displacements (U1=U3=UR1=UR2=UR3=0) and the top; vertical displacements were allowed.

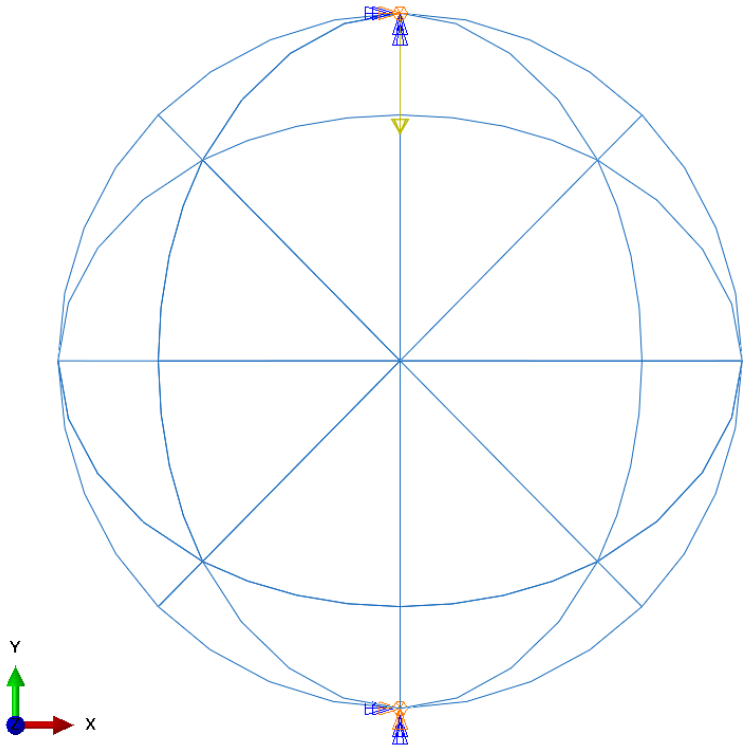

Figure 35: Celestial Schematic for Compression Loading

An additional element that was added to this model was the addition of a coupling to the boundary conditions to the surrounding members. This coupling was used in place of modeling the supporting pucks that were used during the actual experiment to account for the load distribution to the structure. These pucks are discussed in detail in section 2.5, but they allowed the structure to remain upright in the desired orientation during testing and created an offset from the loading platen such that the structure would not make contact with the platens in the case of large deformations. As shown in Figure 38, the model predicted the displacement of the loading vertex to drop causing it to drop below

the level of the other members during loading. Without an offset of the loading point, these members would contact the loading platen and change the loading and support scheme entirely. The coupling constraint was similar to the one described in section 2.2.3.3 which used a reference point. For this case a reference point was placed at the top and bottom vertices of the celestial. A coupling constraint was created with the adjacent members acting as slaves to the reference point as shown in Figure 1.

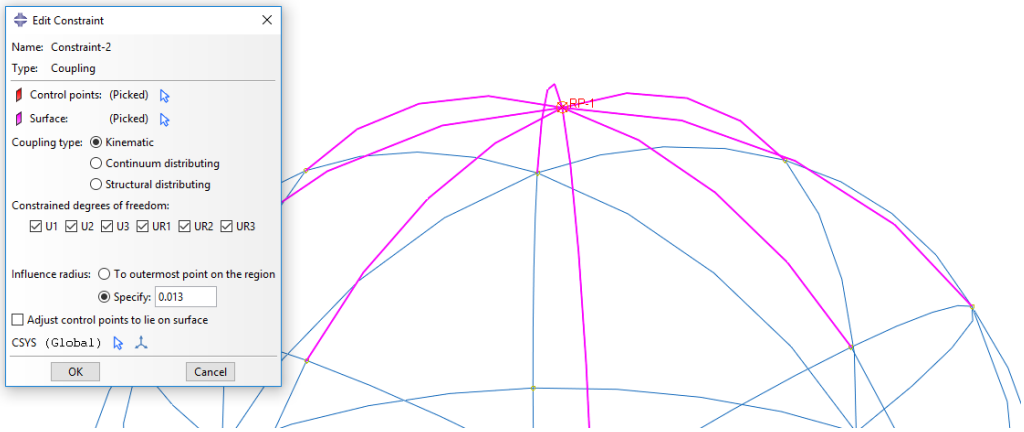

Figure 36: Coupling Constraint Used for the Compression Analysis

The coupling type was kinematic with all three translational degrees of freedom and rotational degrees of freedom constrained. This meant that all of the elements within a certain influence radius were constrained to the movement of the reference point in the degrees of freedom selected. This type of constraint also distributes the load applied as a concentrated force to all the nodes within the influence radius which reduces the stress concentration caused by applying a concentrated force to the model. The influence radius for this constraint was restricted to the radius of the support puck that was in contact with the structure, a radius of 13 mm. The loads and boundary conditions were then assigned

to their respective reference points for the analysis. The result of this constraint is demonstrated in Figure 37 where a circle is evident where the stresses are lower until the influence radius limit is reached due to the additional support.

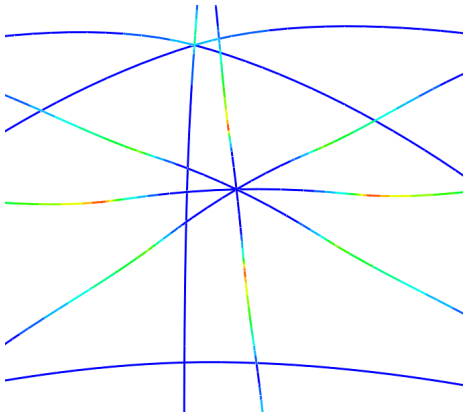

Figure 37: Demonstration of the Coupling Constraint

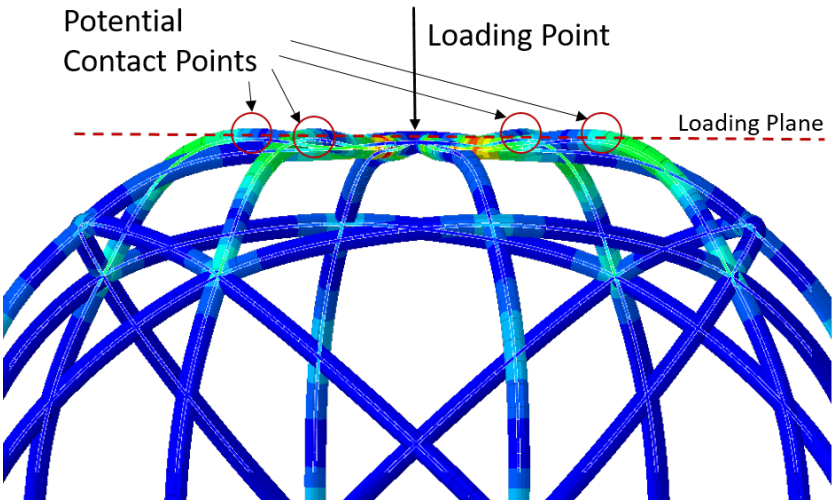

Figure 38: Potential Contact Points during Loading

The overall purpose of the experiment was so see if representing the anisotropic material as a homogeneous isotropic material produces an accurate result. The experiment itself

does not represent the loading scheme that the structure would experience supporting a vacuum.

2.4. Additive Manufacturing

The use of additive manufacturing during this research was for the purpose of model validation experimentation. The manufacturing process of additive manufacturing does not require the use of fasteners, adhesives, or specially designed joinery. The models can be kept simple as such fabrication methods would need to be accurately modeled. This manufacturing method also does not place many constraints on the complexity of the structure built. The size of the structure; however, is constrained by the build volume of the selected machine. A potential drawback to the additive manufacturing process is the inclusion of anisotropy in the material properties. Kevin Greenoe explored this anisotropy in his thesis work involving the material Ultem 9085 [14]. In this work Kevin isolated individual rings from the whole structure at different print orientations. Kevin was able to determine the varying moduli based on print orientation. The same material, Ultem 9085, was used for the experiments conducted during this research from the same printing machine. This printer used was the Fortus 450mc fused deposition modeling (FDM) printer pictured in Figure 39. The full celestial structure was printed for the purposes of mechanical testing.

Figure 39: Fortus 450mc 3-D Printer

2.4.1.1. Material Properties

The material properties of the Ultem 9085 were taken directly from the manufacturer's website and are shown in Table 3 in section 1.4. A deviation from the use of these properties was based on the experiments conducted by Greenoe. In these experiments, an average modulus of elasticity of 2.373 GPa was determined for the three print orientations. This modulus was used for the modeling of the full celestial. The material properties for the XZ orientation were used for the ROMs as this was the most conservative approach. This involved a modulus of 2050 MPa and a maximum stress of 42 MPa [15].

2.4.1.2. Printing Parameters and Support Material

There are several printing parameters that can be varied for an FDM printing process. The parameters of note for this research are print layer height, number of layers, and chamber temperature. As this research is not an exploration of additive manufacturing parameters, the recommended parameters from the manufacturer for this material were used. The characteristics of note were:

Layer Height	0.254 mm
Number of Layers	804
Chamber Temperature	170° C
Ultem 9085 Used	177.4 cm^3
Support Used	457.5 cm^3

The print pattern of the structure consisted of two contours around the perimeter of each of the cross-sectional geometries followed by a rastering pattern to fill the remaining space. The contours each had a width of 0.508mm. A representation of this fill pattern is shown in Figure 40.

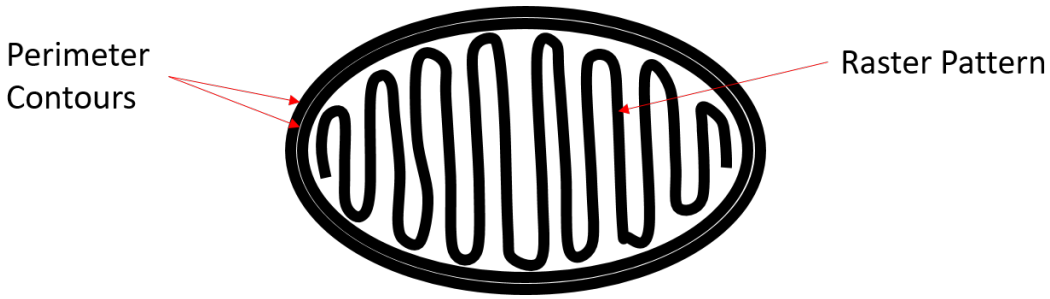

Figure 40: 3-D Printing Fill Pattern

The structure required the use of a lot of support material for the fabrication of the slender cantilevering members; almost three times as much support material was needed compared to the actual structure material. This support material had to be removed from the structure prior to experimentation. The primary method of removing the material was through mechanical means. The as-printed structure with various levels of support material removed are shown in Figure 41 and Figure 42 while to completely liberated structure is shown in Figure 43.

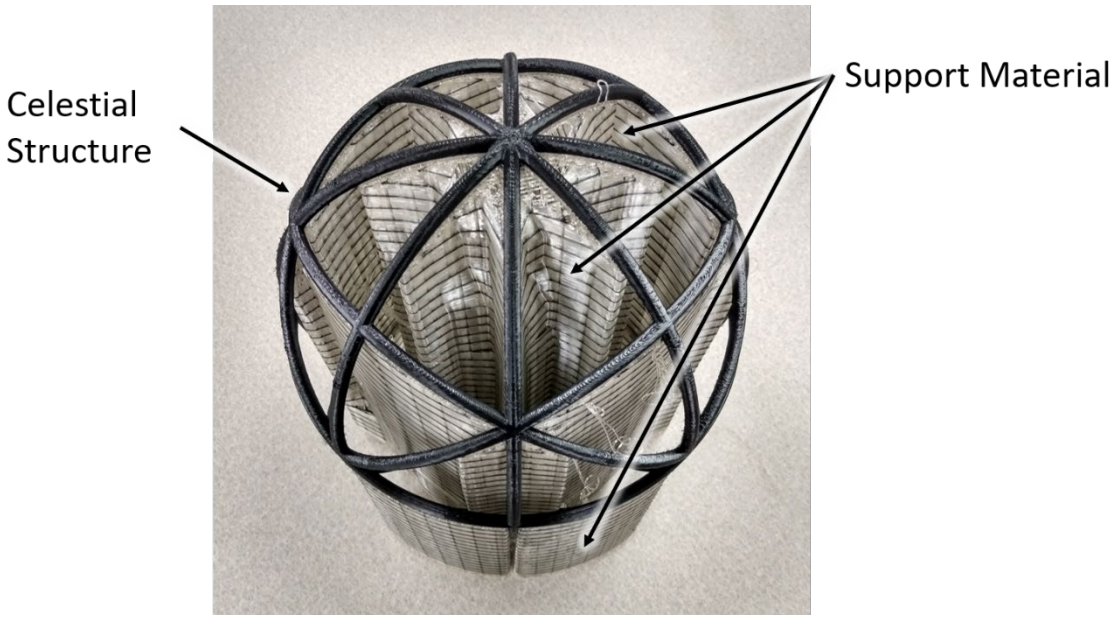

Figure 41: Printed Celestial with Support Material

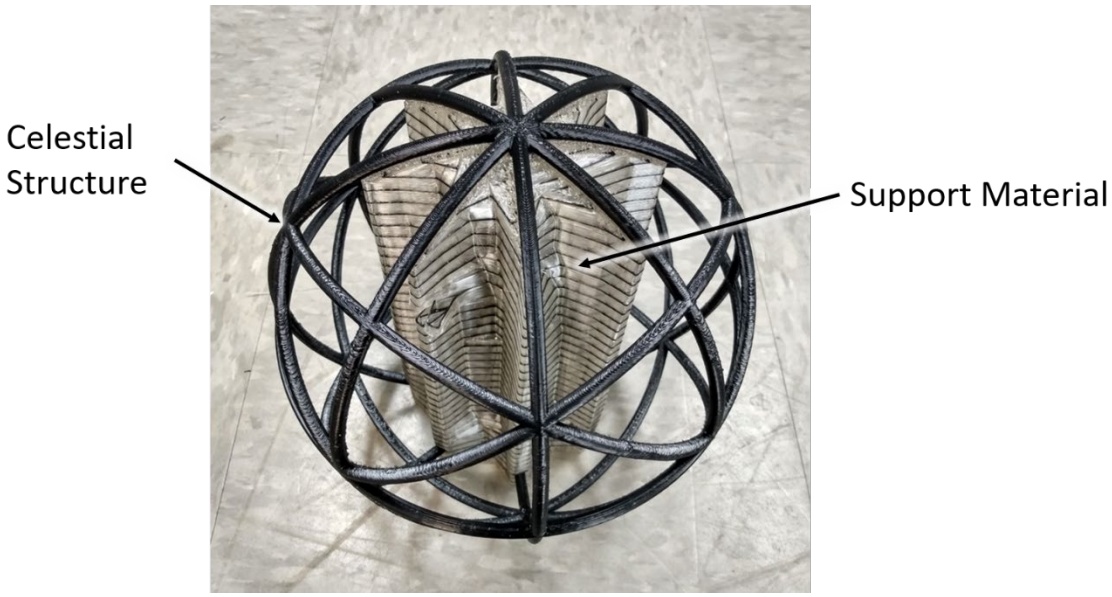

Figure 42: Printed Celestial with Only Center Support

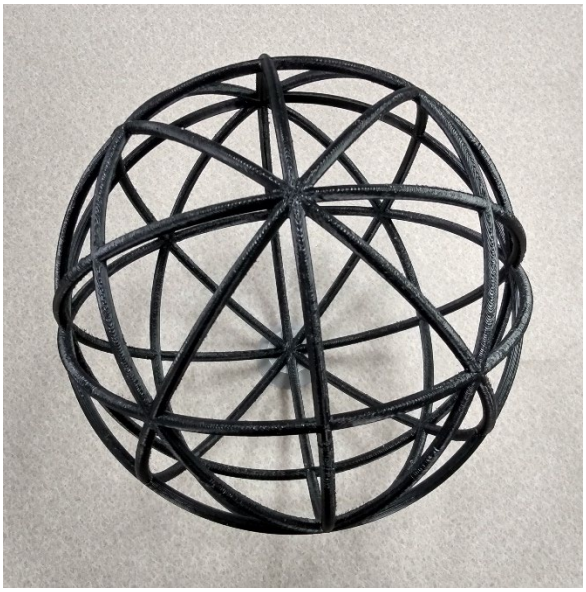

Figure 43: Liberated 3-D Printed Celestial Icosahedron

The celestial structure was also printed in hemispheres to evaluate potential pitfalls during the printing process and determine the necessary support material. Printing

structures with large overhangs can prove difficult for FDM type of printing. To further complicate the process, the presence of tall slender members can be a source of malfunction as the printing head relies on a level of adhesion and resistance in the filament to properly distribute the material. In some printed members, as the members became more and more cantilevered, the printing process displaced the members leading to either printing flaws or complete failure through disconnections. Printing viability is an important consideration for these types of structures; furthermore, removal of the support material is usually done through mechanical means. This places a requirement for a certain level of care placed into separating the support material from the good structure. Fragile structures may be at a greater risk of damage during the support material removal process.

2.5. Mechanical Testing of the 3-D Printed Frame

The mechanical testing of the 3-D printed celestial frame was conducted using an MTS Acumen 3 electrodynamic load frame with a 3 kN load cell, shown in Figure 45. This test frame is a tabletop electrically powered machine that does not use hydraulic pressure. The machine uses pneumatic grips and has a maximum stroke of 70 mm. The testing was conducted under displacement control as a quasi-static uniaxial compression experiment. The celestial frames were held in place with 3-D printed pucks with reliefs cut into them to cradle the rings at the top and bottom vertices. These pucks were printed from the material polylactic acid (PLA). An example of these pucks is shown in Figure 44. The purpose of the pucks was to keep the structure's orientation with respect to the loading direction. Without something to stabilize the rotation of the structure, it was

likely that the geodesic shape would slip and displace to a more stable orientation, balancing on one of the triangular faces. This was not a desirable orientation for testing this structure.

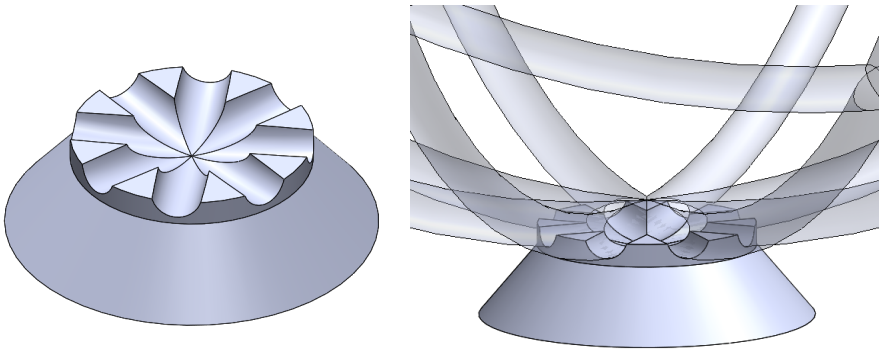

Figure 44: Loading Puck (Left), Nested with Celestial Structure (Right)

The pucks were placed onto flat platens which were gripped by the machines pneumatic wedge grips. The pucks themselves were not secured to the platens in any way and only friction would prevent them from sliding or rotating about the loading axis. The loading was controlled using displacement control at a rate of 1.00 mm/min. This loading rate was slightly slower than the loading rate used by Greenoe during his research of 1.27 mm/min [14]. During his experiments, it was determined that too large of a displacement rate imposed standing waves within the individual rings and caused catastrophic fracture of the rings immediately upon loading; this was to be avoided as the build time of these structures was 27 hours. The load and actuator displacement were recorded at a rate of 5 Hz. A camera was setup to record images of the test at 10 second intervals to capture any structural deformations that occurred during the test.

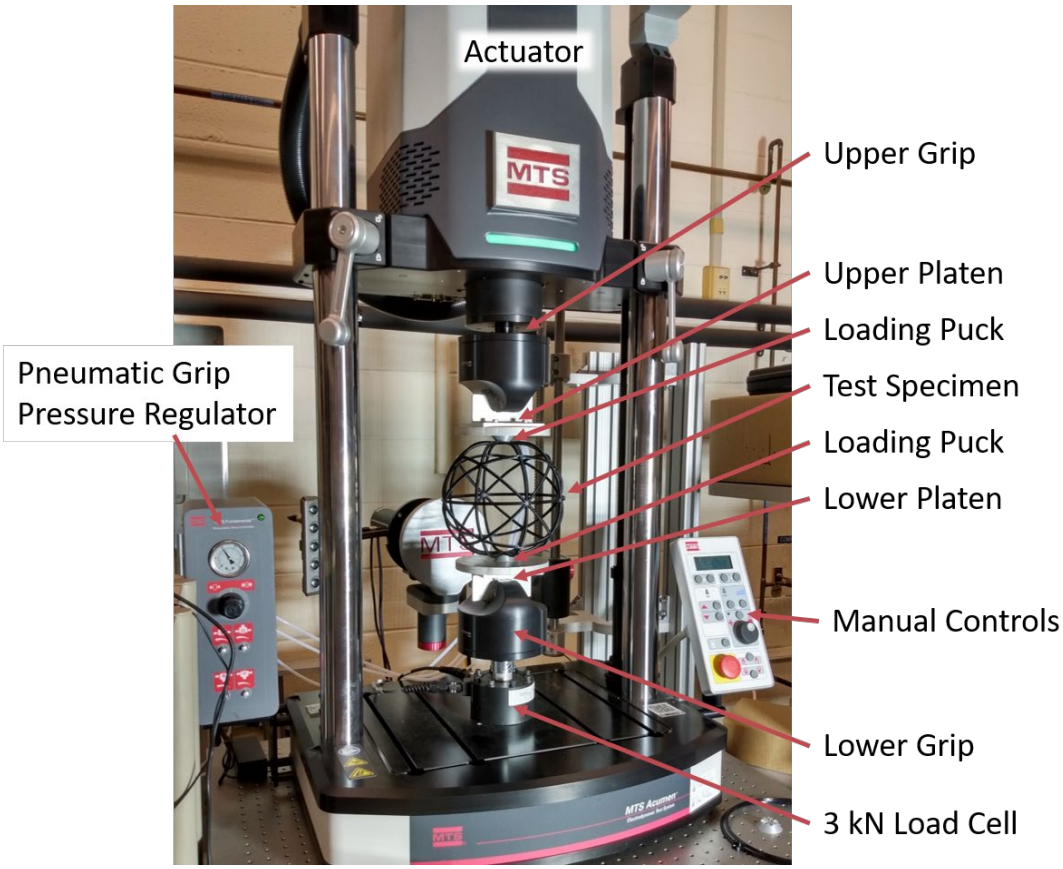

Figure 45: Acumen Electrodynamic Test Frame with Specimen

2.6. Summary

The methodology chapter discussed the fundamental theory of the ROM and the execution of the modeling. Several methods were investigated to determine the best and most accurate load profile that would be applied to the structural members to represent the load transferred from the skin. Ultimately a beam diameter for the celestial structure was determined from the load profile developed using finite element approach to a rigid characteristic triangle. This load profile was similar to the geometric load profile. Several FEA techniques were used including various element types and analysis types that built

off of the work of past researchers. These techniques were used to overcome the challenges of material behavior and nonlinear geometry. Ultimately the structure was able to be manufactured via 3-D printing for the purpose of mechanical testing. These mechanical tests would serve as a validation for the FEA models and serve as an exploration towards the structural behavior of the celestial icosahedron shape.

3. Results and Discussion

3.1. Chapter Overview

This chapter documents the pertinent results from the analysis techniques and experiments discussed in Chapter 2. A large focus is placed on the relationship between the ROM and the full celestial models, both with and without the skin. A comparison will be made about the different load profiles chosen and how they compare to the result of the full celestial model evaluated with and without the skin. Adjustments were made to the ROM methodology in an attempt to better represent the results observed from the full model analysis. The results of two celestial frame experiments showed how the manufacturer's material properties may not be actually realized in the printed components and how the anisotropic material properties influence the failure.

3.2. Results of the ROM Technique

3.2.1. ROM Results for Load Profile 1

The ROM technique was employed as described in section 2.2 for both loading schemes as described in section 2.2.3. The results in this section are from the fixed triangle load profile, method 1. The results of the arch stiffness analysis for the iterations of completed are shown in Table 12, for each case an arbitrary load of 10 N was applied.

Table 12: 2-Segment Arch Stiffnesses for ROM Load 1 Iterations

Arch	Iteration 1		Iteration 2	
	Displacement (mm)	Spring Constant (N/mm)	Displacement (mm)	Spring Constant (N/mm)
1	0.332	30.0	0.434	23.0
2	0.188	53.1	0.241	41.6
3	0.335	29.9	0.435	23.0

4	0.581	17.2	0.754	13.3

The result of the ROM for each of the three segments is shown in Table 13. The beam diameters for each iteration are shown in parentheses next to the iteration callout. For this case, the starting beam radius of 2.54 mm resulted in a smaller stress than the ultimate stress of 42 MPa.

Table 13: ROM Stress Levels for Load Profile 1

	Maximum Stress (MPa)	
Segment	Iteration 1 (2.54 mm)	Iteration 2 (2.37 mm)
A	30.9	35.3
B	36.4	42.2
C	30.6	35.7

After iteration 2, the new beam radius was calculated to be 2.38 mm which would result in a maximum stress of 42 MPa in Segment B. The resulting stress field of iteration 2 is shown for all three segments in Figure 46. These stresses are the von Mises stresses traced along the bottom of each beam. Each of the deformed plots has a deformation scale factor of +5 to exaggerate the displacements. The maximum stresses are located near the boundary conditions. This stress riser is caused by the fixed rotation boundary condition.

The ends of the curved beams of the model did displace in the radial direction. This indicates that a radial reaction force was necessary in order for the model to reach equilibrium. This displacement of the free ends represents the displacement of the intersections and allows these segments of the celestial to behave more like they would if they were part of the full structure rather than locked into a clamped type boundary condition. This displacement is allowed by the spring boundary conditions and is a

product of a forces at the boundaries displacing the springs to achieve equilibrium. This displacement is linearly proportional to the radial reaction force. These end displacements can go either radially inward or outward depending on the direction of the forces. If the ROM was representing the behavior of the intersections accurately, the displacements ought to be the same regardless of the segment being modeled. This was generally not the case. Theses displacements for iteration 2 are shown in Table 14.

Table 14: ROM Boundary Displacement by Intersection Load Case 1

Intersection	Segment A	Segment B	Segment C	Difference
2-Ring		-0.237 mm	-0.269 mm	0.032 mm
3-Ring	+0.090 mm		-0.047 mm	0.137 mm
4-Ring	+0.294 mm	+0.191 mm		0.103 mm

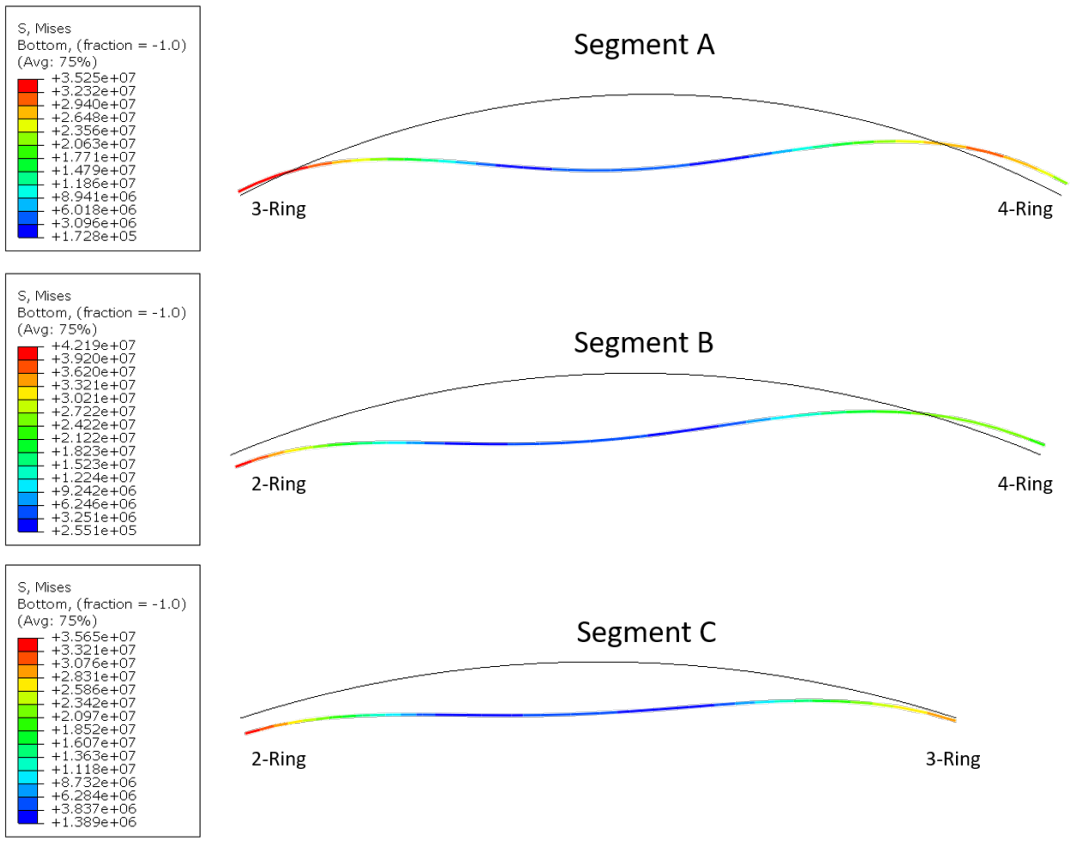

Figure 46: Deformed ROM Beams for Load Profile 1, Iteration 2

3.2.2. ROM Results for Load Profile 2

The same ROM process was repeated with load profile 2 as determined from the flexible triangle method as described in section 2.2.3. This method used the same starting beam radius of 2.54 mm. The results for the arch stiffnesses used in the models are shown in Table 15, for each case a load of 10 N was applied.

Table 15: 2-Segment Arch Stiffnesses for ROM Load 2 Iterations

Arch	Iteration 1		Iteration 2		Iteration 3	
	Disp. (mm)	Spring Const. (N/mm)	Disp. (mm)	Spring Const. (N/mm)	Disp. (mm)	Spring Const. (N/mm)

1	0.332	30.0	0.159	62.9	0.184	54.2
2	0.188	53.1	0.960	104.2	0.110	91.2
3	0.335	29.9	0.161	62.0	0.187	53.6
4	0.581	17.2	0.266	37.6	0.310	32.2

The result of the ROM for each of the three segments is shown in Table 16. The beam diameters for each iteration are shown in parentheses next to the iteration callout. For this case, the starting beam radius of 2.54 mm resulted in a larger stress than the ultimate stress limit of 42 MPa.

Table 16: ROM Stress Results for Load 2

	Maximum Stress (MPa)		
Segment	Iteration 1 (2.54 mm)	Iteration 2 (3.09 mm)	Iteration 3 (2.97 mm)
A	62.1	38.8	42.6
B	49.0	32.5	35.3
C	44.2	28.1	30.9

After iteration 3, the new beam radius was calculated to be 2.99 mm which would result in a maximum stress of 42 MPa in Segment A. The resulting stress field of iteration 3 is shown for all three segments in Figure 47. The maximum stresses for this load profile are also near the boundaries of the arches. The key differences between the results of the two load profiles are the final beam radius determination and the segment which possessed the maximum stress. The boundary displacements did not show any better agreement between segments for this case as shown in Table 17.

Table 17: ROM Boundary Displacement by Intersection, Load Profile 2

Intersection	Segment A	Segment B	Segment C	Difference
2-Ring		-0.046 mm	-0.160 mm	0.114 mm
3-Ring	-0.083 mm		-0.043 mm	0.040 mm
4-Ring	+0.882 mm	+0.081 mm		0.801 mm

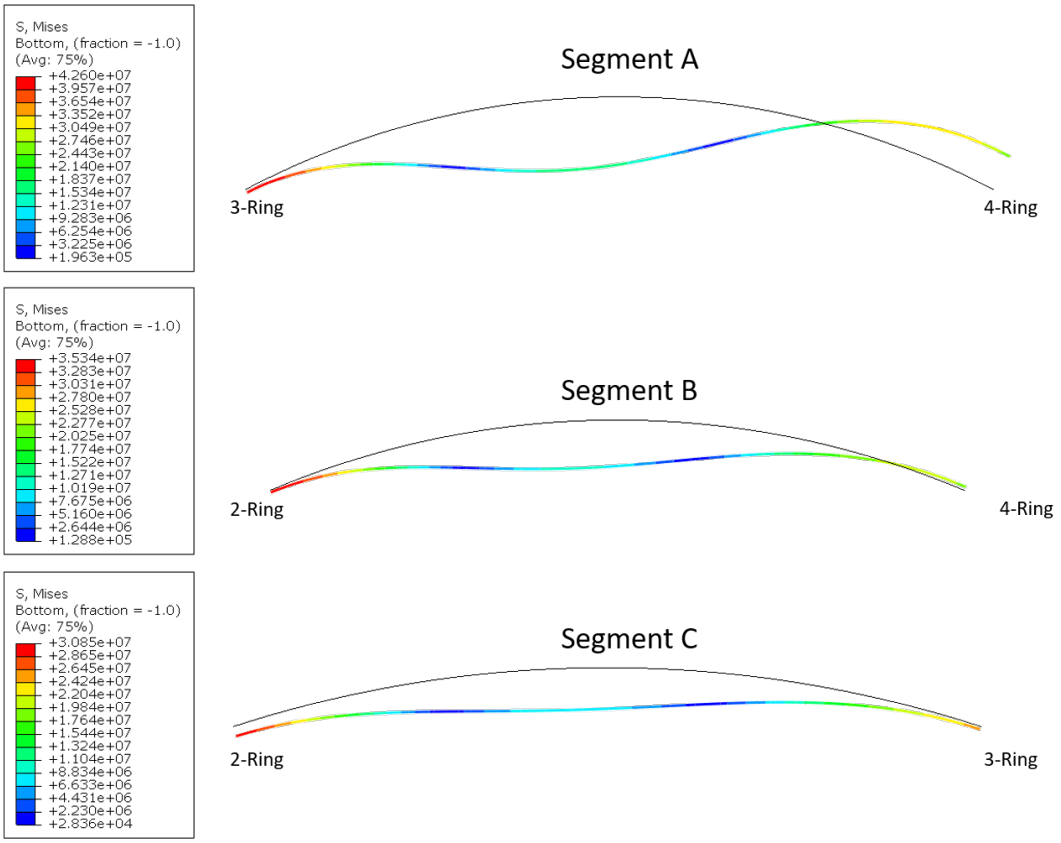

Figure 47: Deformed ROM Beams for Load Profile 2, Iteration 3

3.3. Results of the Full Celestial Models

Overall the full celestial models did not show good agreement with the ROM. Ultimately the ROM were much stiffer than the actual structure and presented a much lower state of stress than the full celestial models in both cases analyzed. The bare-frame celestials with the line loads of load profile 2 showed better correlation to the skin-on celestial results indicating that this load profile method is more representative of the loads

incurred by the pressure loads. Some adjustments were made to the ROM to reduce the stiffness of the boundary conditions while still relating them to the specific geometry.

3.3.1. Full Celestial Models without Skin

The full celestial model was created as described in section 2.3.1 with two different load profiles. Three points' displacements were tracked during loading to compare to the free-end displacements of the ROM segments. The points tracked represent each of the three intersection types as shown in Figure 48.

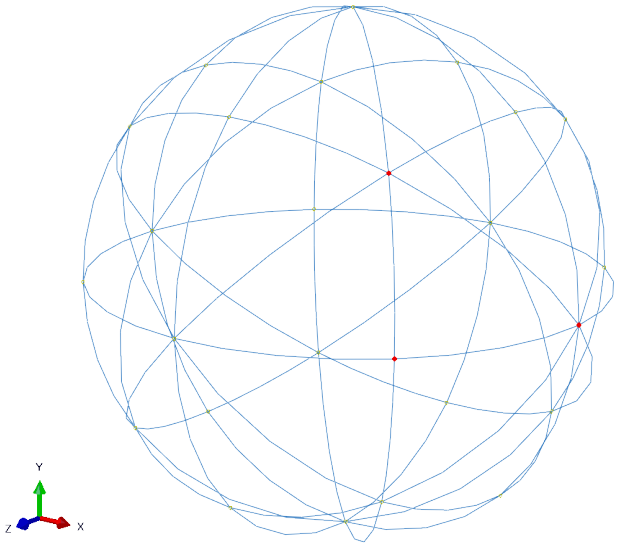

Figure 48: Tracked Intersections During Loading

3.3.1.1. Load Profile 1

Load Profile 1 was applied to the bare structure full celestial model with a beam radius of 2.38 mm. The boundary conditions for this analysis were displacement fixed (U1=U2=U3=0) and rotationally fixed (UR1=UR2=UR3=0) at the bottom vertex and lateral displacement fixed (U1=U3=0) at the top vertex. The results of this analysis are

shown in Figure 49. These stress levels are traced along the sphere's internal radius such that the stress indicated along the midsection of each member is in tension. This is the case unless otherwise described. The deformed celestial models have a deformation scale factor of 1 unless otherwise stated.

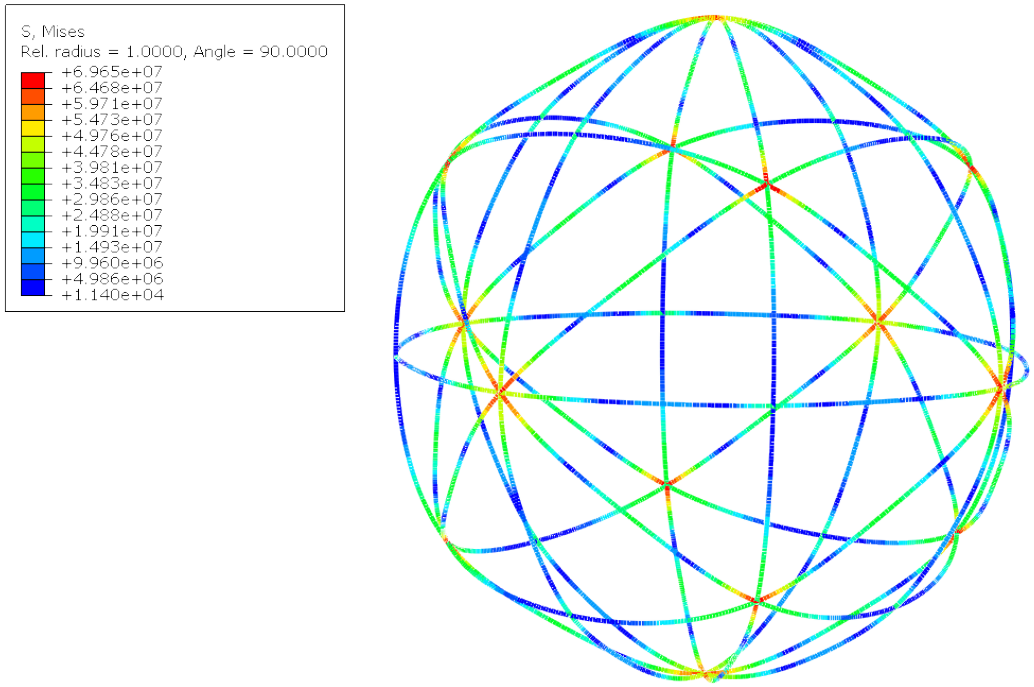

Figure 49: Stress in Celestial Frame with Load Profile 1, 2.38 mm

The maximum stress in this model was found to be 69.65 MPa. This was higher than the expected stress of 42 MPa, the ultimate tensile stress limit on the material, from the ROM analysis; however this stress level was in compression. Since the material was expected to fail in tension, the highest tensile stress level was found to be 42.12 MPa. The stress level was right at the expected maximum failure stress, but at a very different location. This stress occurred at the 4-ring intersection while it was predicted to occur near the 3-

ring intersection. This structure would likely fail when loaded if this geometry was used to create the structure to support the vacuum as there would be no factor of safety (FS). To determine a geometry that would be appropriate for manufacture, the worst case yield stress of 33 MPa [15] was selected to be the maximum allowable stress in the tension mode. Iterations were conducted on the full celestial model to determine the minimum beam radius that would result in stresses below the ultimate material stress. This analysis resulted in a beam radius of 2.64 mm and a maximum tension stress of 30.06 MPa. The deformed celestial icosahedron frame with this beam radius is shown in Figure 50, the deformations of this model were not scaled. This beam radius was selected for the geometry to be 3-D printed. The geometry was expected to fail by fracture and not collapse.

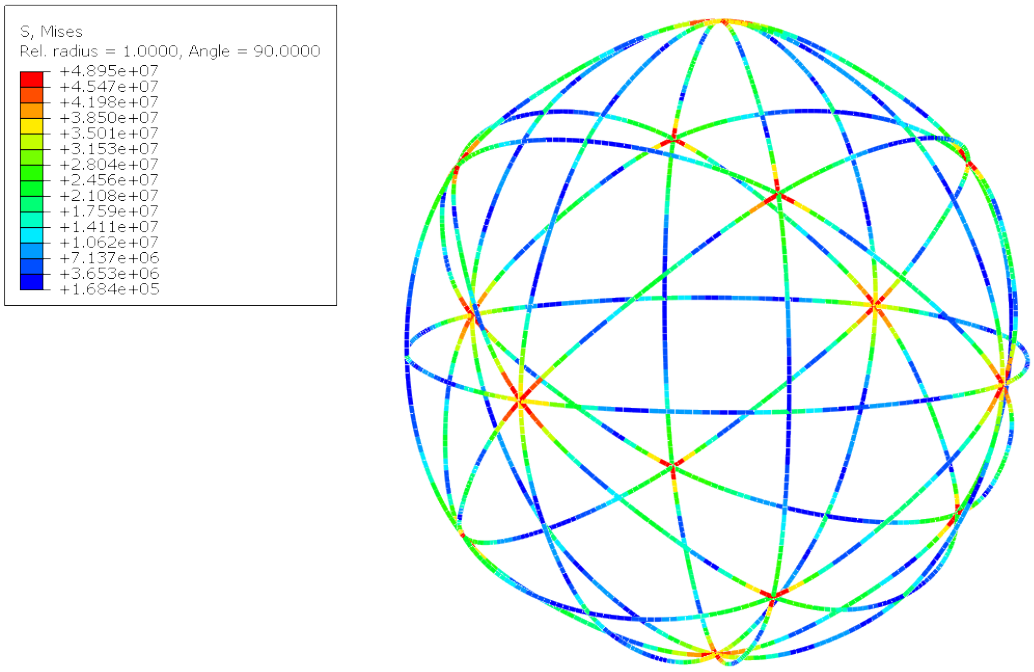

Figure 50: Stress in Celestial Frame with Load Profile 1, 2.64 mm

As stated previously, if the ROM was capable of representing the behavior of the celestial members, the displacements of the free ends of the ROM should be similar to the displacements of the full celestial intersections. This comparison was made by tracking the displacement of each intersection during the full celestial analysis. The displacements from the analysis with load profile 1 and the 2.64mm beam radius is shown in Table 18 along with the result from the ROM.

Table 18: Load Profile 1 Displacement Comparison

Intersection	Full Model	Segment A	Segment B	Segment C
4-Ring	+1.528 mm	+0.294 mm	+0.191 mm	
3-Ring	+0.361 mm	+0.090 mm		-0.047 mm
2-Ring	-1.371 mm		-0.237 mm	-0.269 mm

Many of the displacements from the ROM differ from the full model displacements by an order of magnitude. It is important to note that the ROM displacement shown in Table 18 were taken from the 2.38 mm beam radius analysis. Although there is a difference in geometry, the full model was run with larger diameter beams which would be expected to deflect less. This comparison was meant to observe rough trends and not to act as a definitive validation. Another point of interest is that the displacement of the 3-ring intersection was predicted to move radially inward by the ROM of segment C, but was represented as displacing radially outward in the full structure model and the ROM of segment A. The difference in displacement magnitudes could indicate that the spring constants are too large on the ROM resulting in a model that boundary conditions that are too stiff. This aspect of the ROM will be addressed in section 3.3.3.

3.3.1.2. Load Profile 2

Load profile 2 was applied to the bare structure celestial model with a beam radius of 2.99 mm. This geometry was determined based on the stress levels found in the 2.64 mm beam radius analysis. The boundary conditions for this analysis were displacement fixed (U1=U2=U3=0) and rotationally fixed (UR1=UR2=UR3=0) at the bottom vertex and latera displacement fixed (U1=U3=0) at the top vertex. The results of this analysis are shown in Figure 51.

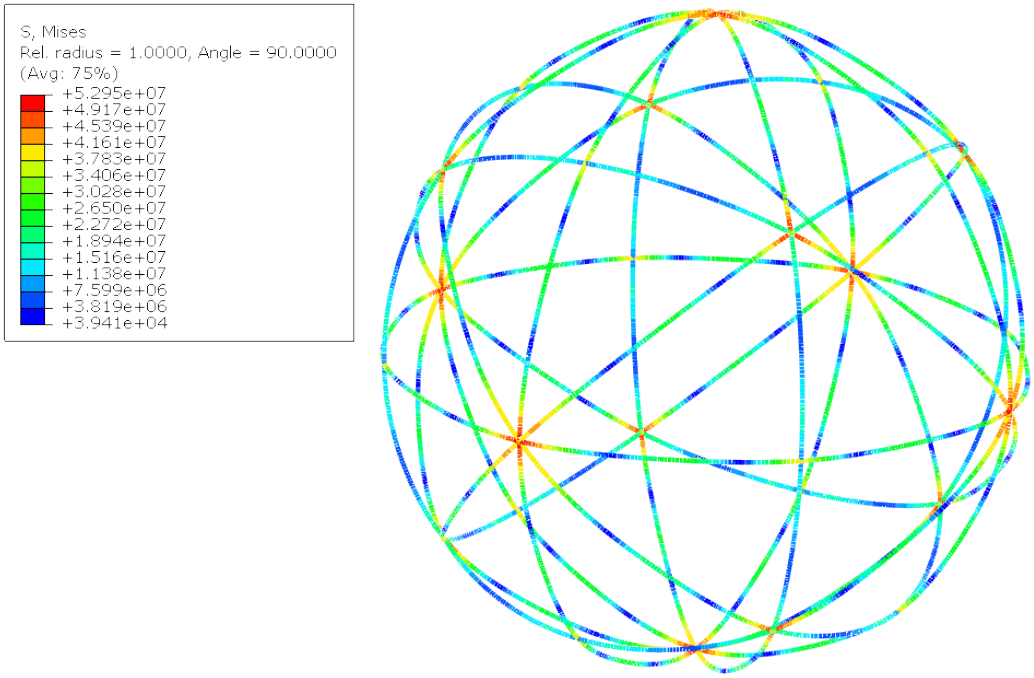

Figure 51: Stress in Celestial Frame with Load Profile 2, 2.99 mm

The maximum stress in this model was found to be 52.95 MPa. This was higher than the expected stress of 42 MPa, the ultimate stress limit on the material, from the ROM

analysis but it is in compression. The highest tensile stress was found to be 38.13 MPa at the 4-ring intersection. For both load profile cases, the full celestial frame identified a higher stress level than the associated reduced models did. The intersection tracking was done on the 2.99 mm beam radius ROM and bare structure analyses as well. The results are shown in Table 19.

Table 19: Load Profile 2 Displacement Comparison

Intersection	Full Model	Segment A	Segment B	Segment C
4-Ring	+1.539 mm	+0.882 mm	+0.081 mm	
3-Ring	-0.299 mm	-0.083 mm		-0.043 mm
2-Ring	-0.564 mm		-0.046 mm	-0.160 mm

Once again the displacements of the ROM are an order of magnitude smaller than the full structure model. Additionally, the ROM of this load profile predicted a radially inward displacement of intersection 3 while the full structure model predicts an outward displacement.

3.3.2. Full Celestial Models with the Skin

In continuation with model complexity, the skin was added to the model such that a pressure load could be applied to the combined structure and skin instead of using a load representation. This model was run with both the 2.64 mm and 2.99 mm structure beam radii as opposed to 2.38 mm as obtained from the ROM of load profile 1. The results for the 2.64mm structure are shown in Figure 52 and the results from the 2.99 mm structure are shown in Figure 53. The stress fields of the skin show close similarities as would be expected since the parameters of the skin remain unchanged between the two analyses. There are stress risers that appear in the skin along the mid sections of the B and C

segments with only a small increase in stress along the midsection of A segments. The stress fields in the skin near the vertices are generally lower than anywhere else on the structure. The stress in the skin was evaluated by any failure criteria as it was not the focus of this study. Looking at the substructure alone, both cases show stress risers near the vertices spanned by the A segments but is more significant in the model with 2.64mm radius members. The maximum stress level in the structure of the 2.64 mm radius beams was 105.8 MPa while the 2.99 mm beam radius structure had a maximum stress of 71.8 MPa in the structure.

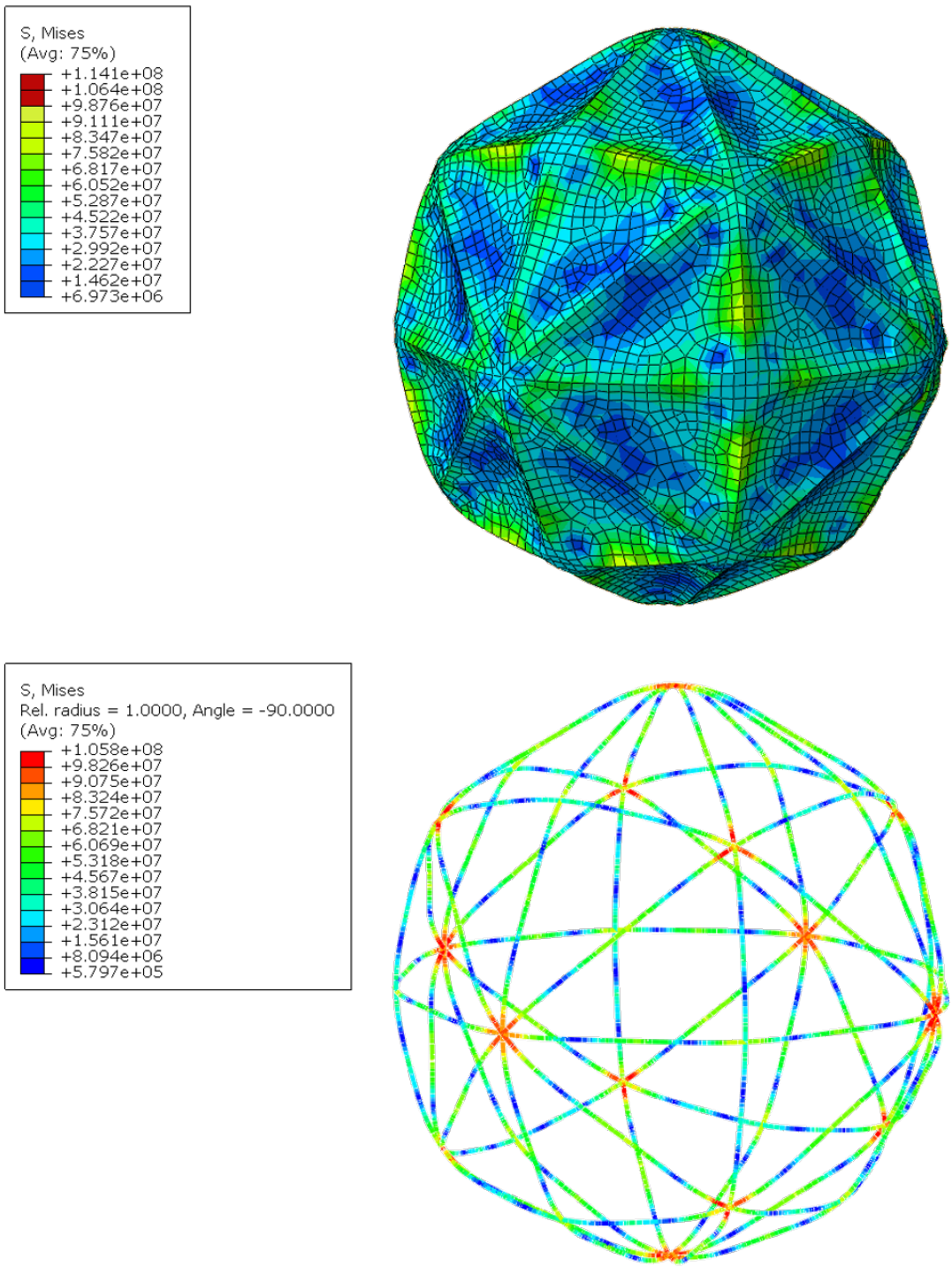

Figure 52: Deformed Celestial with Skin (top), without Skin (bottom), 2.64 mm

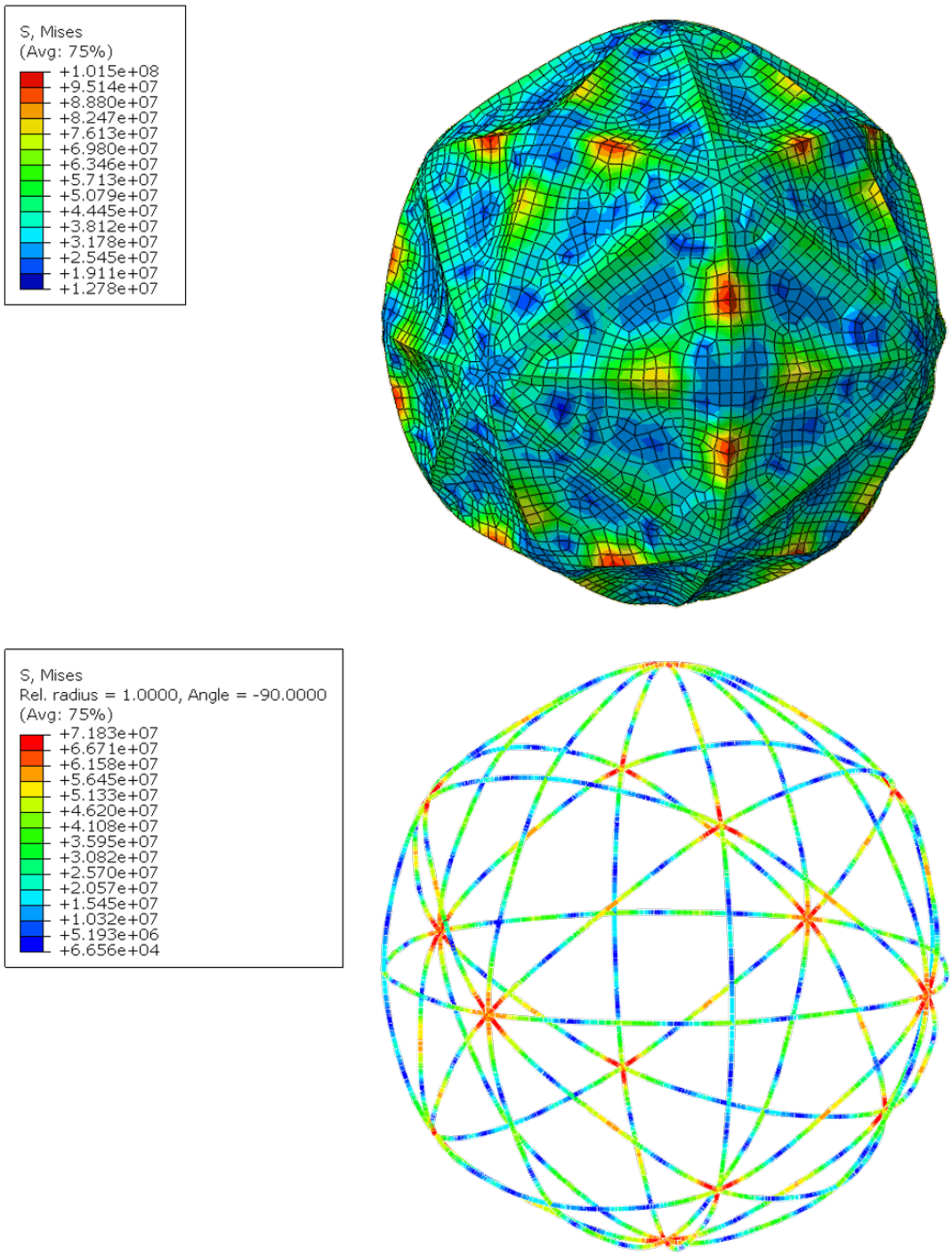

Figure 53: Deformed Celestial with Skin (top), without Skin (bottom), 2.99 mm

The results of the skin-and-frame analysis were more closely represented by the bare frame analysis with the load profile 2 than with load profile 1. Inspecting the 2.64 mm bare frame loaded with profile 1, the maximum von Mises stress in the midsection of segment A was 46.62 MPa in compression and 24.53 MPa in tension; referring to the two sides of the bending curve. Comparing this to the maximum stress along the midsection of segment A from the skin-on analysis, a stress of 83.57 MPa in compression and 69.39 MPa in tension. Inspecting the 2.99 mm bare frame loaded with profile 2, the maximum stress in the midsection of segment A was 39.92 MPa in compression and 26.30 MPa in tension. The skin on analysis produced a stress of 68.47 MPa in compression and 57.89 MPa in tension. This comparison shows that load profile 2 was closer to the results of the skin-on analysis, but was still off by a factor of about 2 indicating there is an interaction between the skin and frame that is not captured in the model of just the frame.

The results of the full celestial and skin analysis were evaluated for symmetry across the entire structure. The case being investigated was if each of the same type of intersections displaced in the same way regardless of where it was located on the celestial. For example, the 4-ring intersection located at the top of the celestial should have displaced the same as the 4-ring intersections located along the equator of the celestial if the reaction was symmetrical. The same would be expected of the 3 and 2-ring intersections. If the structure demonstrates adequate symmetrical behavior throughout the structure, shortcuts in modeling could be done that would reduce the analysis time. For instance if the top and bottom halves behave the same, the top alone could be modeled with a symmetry boundary condition at the symmetry plane. The

method of assessing the symmetry was taken from the boundary condition analysis done by Moore for the celestial icosahedron. The method employed by Moore was to trace each ring as a path and plot the displacement of each point along the path [12]. The data accumulated from this analysis could be overlain to compare overall displacement differences between rings of the same archetype. An example of the ring paths is shown in Figure 54.

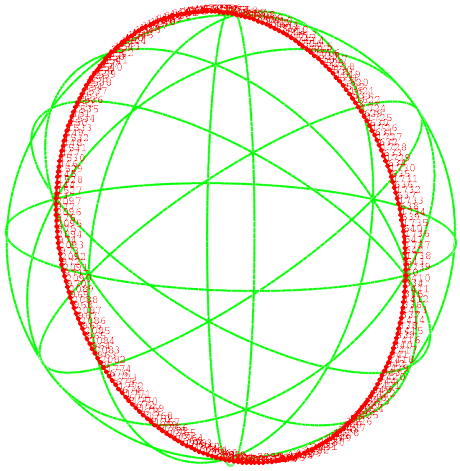

Figure 54: Traced Ring Path for Displacement Measurement

The celestial contains rings of only two variation types. Type 1 only contains B segments with 2 and 4-ring intersections; there are three type 1 rings within the celestial. Type 2 contains only A and C segments with all three intersections; there are six type 2 rings within the celestial. If the ring's response to load is symmetrical, the displacement paths of each ring of the same type should overlap. There should also be patterns within the plots themselves mimicking the periodic geometric symmetry of the celestial. These plots for the 2.99 mm radius celestial are shown in Figure 55.

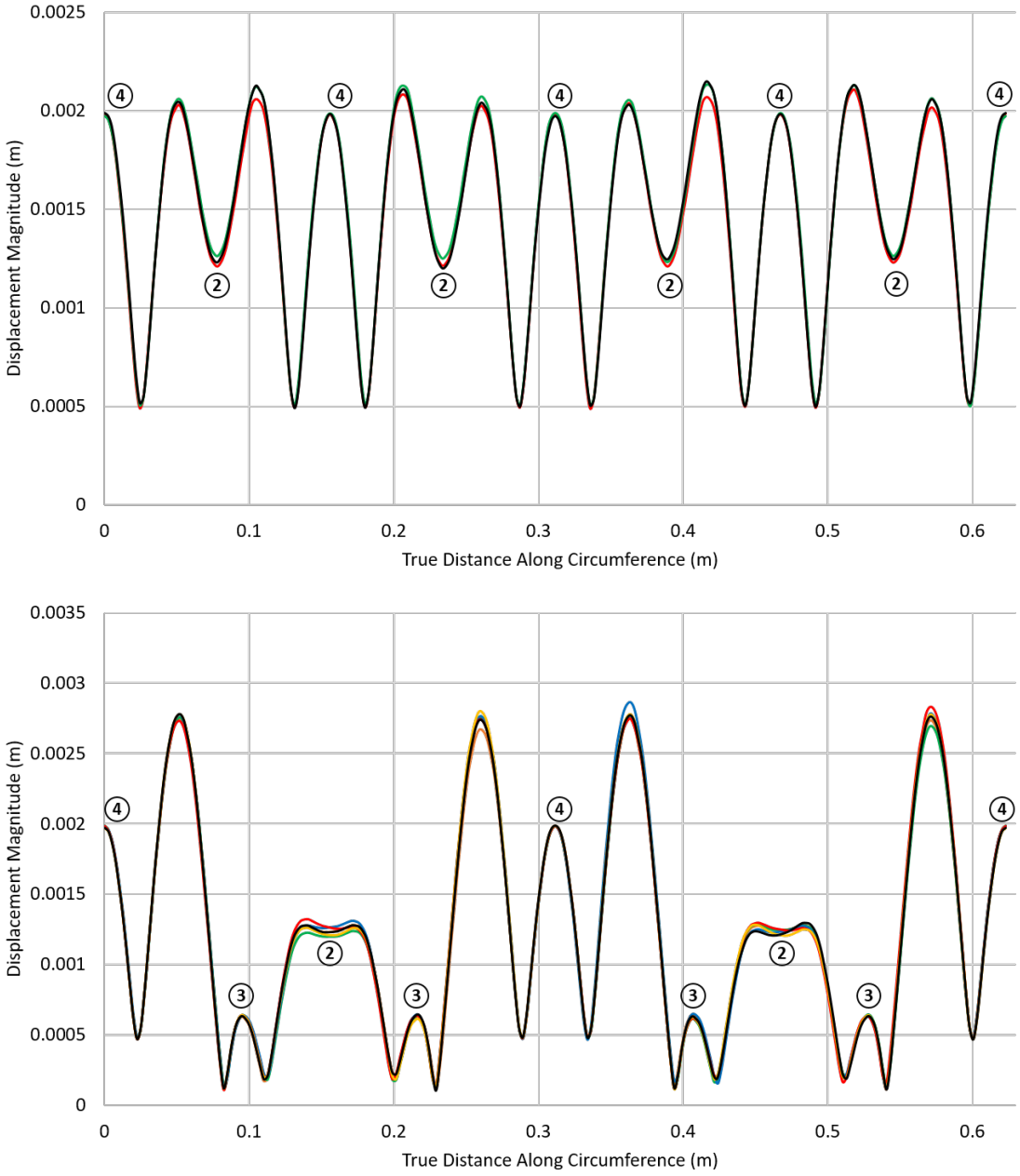

Figure 55: Symmetry Plots, Ring Type 1 (top), Type 2 (Bottom)

The vertices are labeled by the number of rings constituting the intersection, 2, 3, or 4. The displacement plots demonstrate good agreement overall with the peaks and valleys occurring at the same locations along each ring and with relatively equal magnitude. The

displacement curves for rings of type 1 and type 2 demonstrate a periodic symmetry about both the 2 and 4-ring intersections. These intersections are located at 90 degree increments from each other. It is also important to note that even though the plots are of the displacement magnitudes and do not show direction, the 3 and 4-ring intersections displaced in a radially outward direction while the 2-ring intersection moved in a radially inward direction. The specific displacements at each of the vertices are shown in Table 20.

Table 20: Intersection Displacements (mm) for 2.99mm Celestial with Skin

Int. Type	I	II	III	IV	V	VI	VII	VIII	IX	X	XI	XII
4	1.99	1.98	1.97	1.99	1.98	1.98						
3	0.63	0.63	0.63	0.63	0.64	0.63	0.62	0.65				
2	1.21	1.21	1.21	1.23	1.26	1.25	1.23	1.26	1.23	1.20	1.25	1.25

The difference between the largest and smallest displacement of each intersection types were 0.7%, 4.9%, and 5.3% for the 4, 3, and 2-ring intersections respectively. The magnitudes of these differences were 0.02 mm, 0.03 mm and 0.06 mm respectively. The structure has demonstrated symmetry that could be described as quadrant symmetry. This is symmetry about all three Cartesian planes at the same time. If exploited completely, the only need to be $1/8^{th}$ of the sphere would need to be actually modeled to assess the behavior of the full sphere.

Comparing the displacement magnitudes at the vertices of the skin-on model to the bare frame models, the magnitudes of these displacements were found to be larger in the skin-on models than the bare frame. It was expected that the skin would have a stiffening effect on the structure which is seen in section 3.5.2 when the skin is added to

the model. Since this was observed, it is logical to surmise that there is a load distribution variance between the two models. It is possible that the tie constraint used to join the skin to the substructure alters the load distribution compared to the bare frame load profiles.

3.3.3. ROM Modifications

The results from the analysis of the bare frame celestial with the line loads and the skin-on structure indicate that the original boundary conditions may be excessively stiff compared to the true structure. A modification was then made to the ROM boundary conditions to reduce the resistance of the springs in a logical manner. Previously, the stiffness of the whole intersection was used in supporting a single contributing member of the intersection. In reality, this total intersection stiffness is supporting 4, 6, or 8 members at the same time. This means that its stiffness could be assumed to be divided by 4, 6, or 8 depending on how many rings were intersecting at the particular intersection. The ROM modification analysis was conducted for segment A with the beam radius of 2.99 mm with reduced boundary condition spring constants. The new spring constants were 2.75E+4 N/m and 7.77E+4 N/m for the left and right boundaries respectively. The results from this analysis are shown in Figure 56; the deformations are scaled by a factor of 5 for this figure.

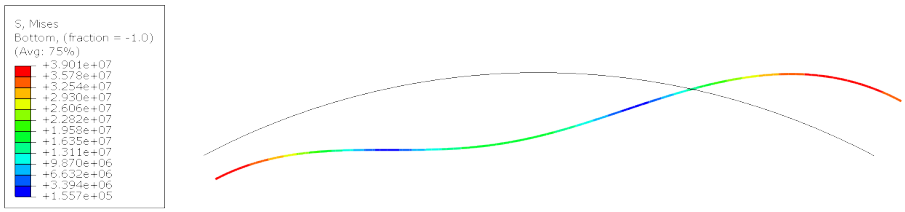

Figure 56: ROM of Segment A with Adjusted BC

This condition still indicated a radial displacement of the left end to be inward instead of outward. In an attempt to reverse this displacement direction, the rotational degree of freedom was released for that end, the 3-ring intersection end, allowing it to freely rotate. This resulted in the direction of the displacement to outward as it did for the full celestial model. The displacement magnitudes from the ROM were overlaid onto the same segment from the full celestial analysis. This showed that the overall displacement pattern that the ROM was generating was similar to the full model. The boundary condition spring constants were altered to see how close the ROM could get to the full celestial model without significant rework. The best boundary conditions ended up being as described in Table 21. The spring constants correspond to the one third the full intersection stiffness of intersection 3 and one eighth the intersection stiffness of intersection 4. These fractions were chosen because they could be logically linked to the intersection as either the number of segments or the number of rings that the total stiffness was divided into.

Table 21: Modified Boundary Conditions

	Spring Constant	Tangential Disp.	Rotation
Left	55.0 N/mm	Fixed	Free
Right	77.7 N/mm	Fixed	Fixed

The largest difference between the ROM prediction and the full celestial results were the magnitude of the peak in the midsection of the segment. It was decided to apply the force magnitude from load profile method 2 instead of using a vector projection approach. This would create a load profile peak increase of approximately 30% compared to the vector

projection approach. The best boundary conditions that were found for this load profile was the same as previously described except the right side spring constant was doubled; representing one fourth the total intersection stiffness. This provided a consistent approach to how the total intersection stiffness was divided. The results of the two adjusted boundary and load conditions compared to the full celestial displacements are shown in Figure 57. The force magnitude case resulted in a good comparison between peak displacement magnitudes along the midsection; however, their location of the peak differs which was also observed in the polynomial fits to the nodal reaction forces in Figure 24. The right side boundary conditions resulted in a similar end condition as the full celestial model produced where the slope of the displacement magnitude curve appears to go to zero. The opposite end which allowed for free rotation did not demonstrate this same behavior and has a steep slope.

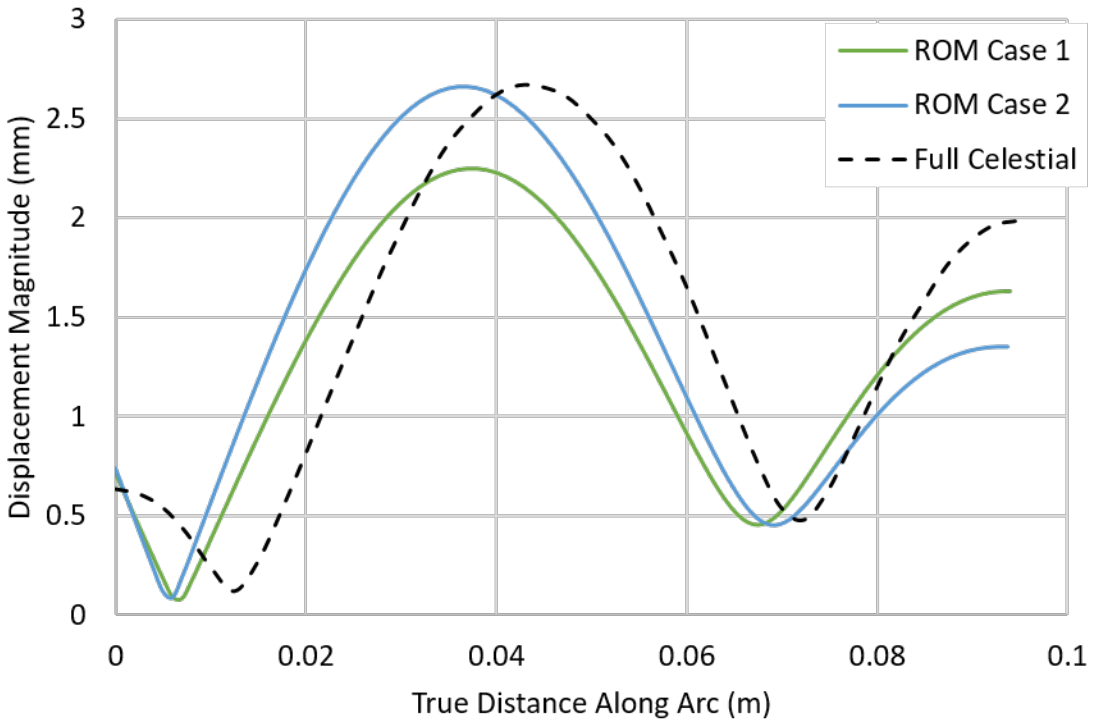

Figure 57: Adjusted ROM Displacements Compared to Full Celestial Displacements

Despite the similarities in the displacement profiles of the segment, the load profiles still remain very different. The load profiles for case 1 and case 2 are shown in Figure 58. The peak stresses still occur near the 4-ring intersection, right side, as they did in the original models. The peak stress for case 2 with the altered load profile is slightly higher than in case 1 at 46.3 MPa, but is still significantly lower than the stresses found in the full celestial structure as shown Figure 59 with segment A isolated. There essentially two stress fields that are present within all of the segments A throughout the celestial. This variation in the stress field coincides with the small variations in the displacements.

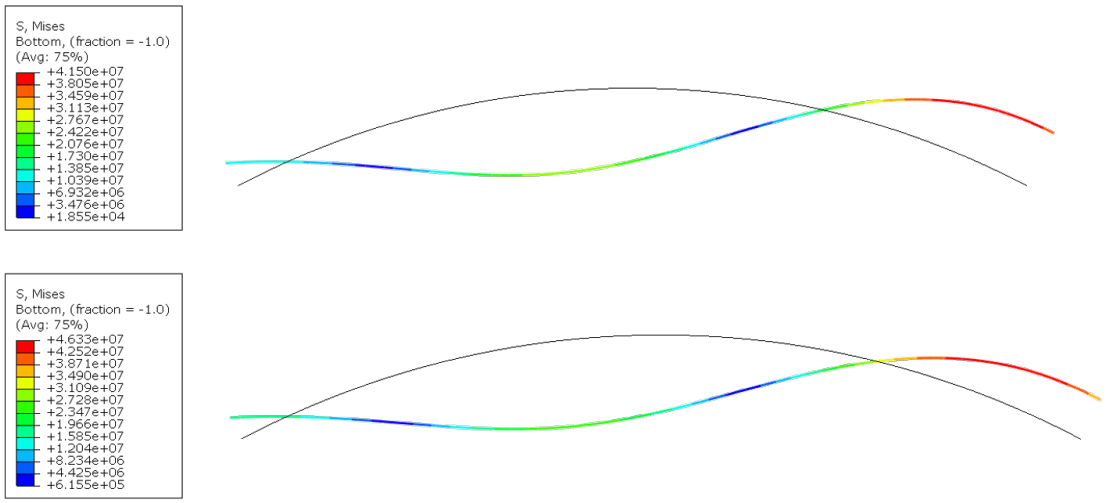

Figure 58: ROM for Segment A with Modified BC, Case 1 (top) Case 2 (bottom)

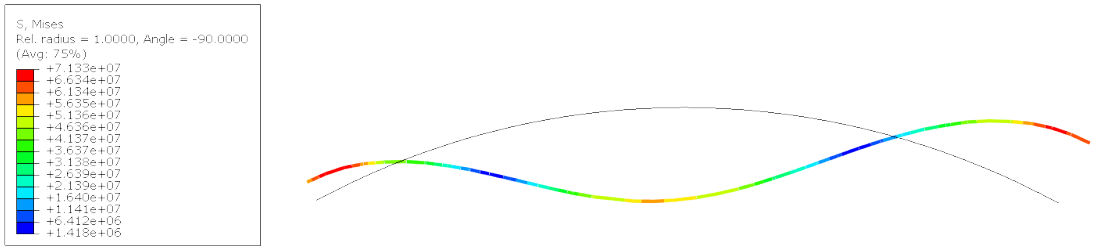

Figure 59: Segment A Isolated from Celestial Model, 2.99 mm

The stress field correlates fairly well to the ROM in terms of pattern. The maximum stresses located near the end points with lower peak stress in the midsection. The magnitude of the stress of segment A taken from the celestial is still much higher than the stresses in the ROM.

Modifying the ROM parameters did enable a closer representation of the deflection of segment A compared to the full celestial model. It may be possible to make further adjustments to the ROM to force the results closer together. These modifications might include torsion springs placed at the boundaries instead of simply allowing the

rotation to be free or fixed. This type of end condition could allow the slope of the displacement curve to be zero at the left free end instead of having a steep slope as discussed previously. These new boundary conditions are represented in Figure 60 where R_1 and R_2 are torsion spring constants.

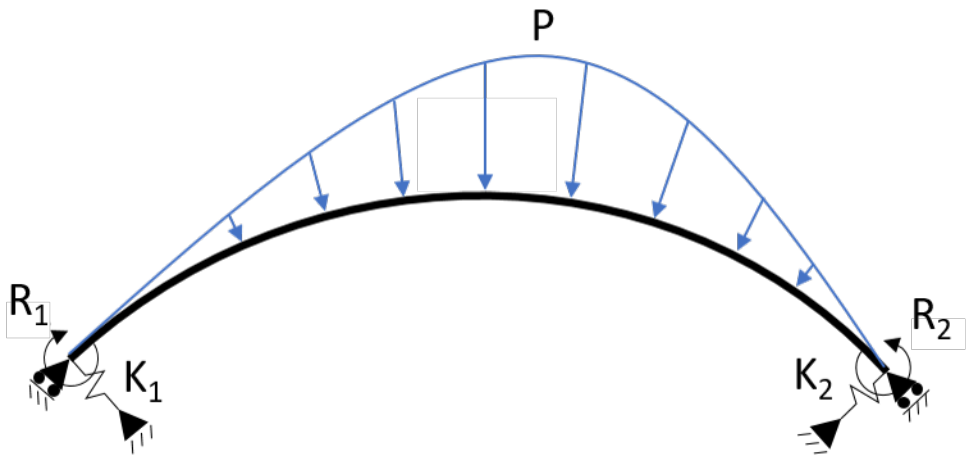

Figure 60: Modified ROM Boundary Conditions

The difference in the stress fields compared to the original is shown FIGURE with the original stress field shown in the top image, the stress field with the modified boundary conditions in the middle image, and the stress field with the modified boundary conditions and the higher load profile shown in the bottom image. The modified boundary conditions actually lowers the maximum stress level found in the segment.

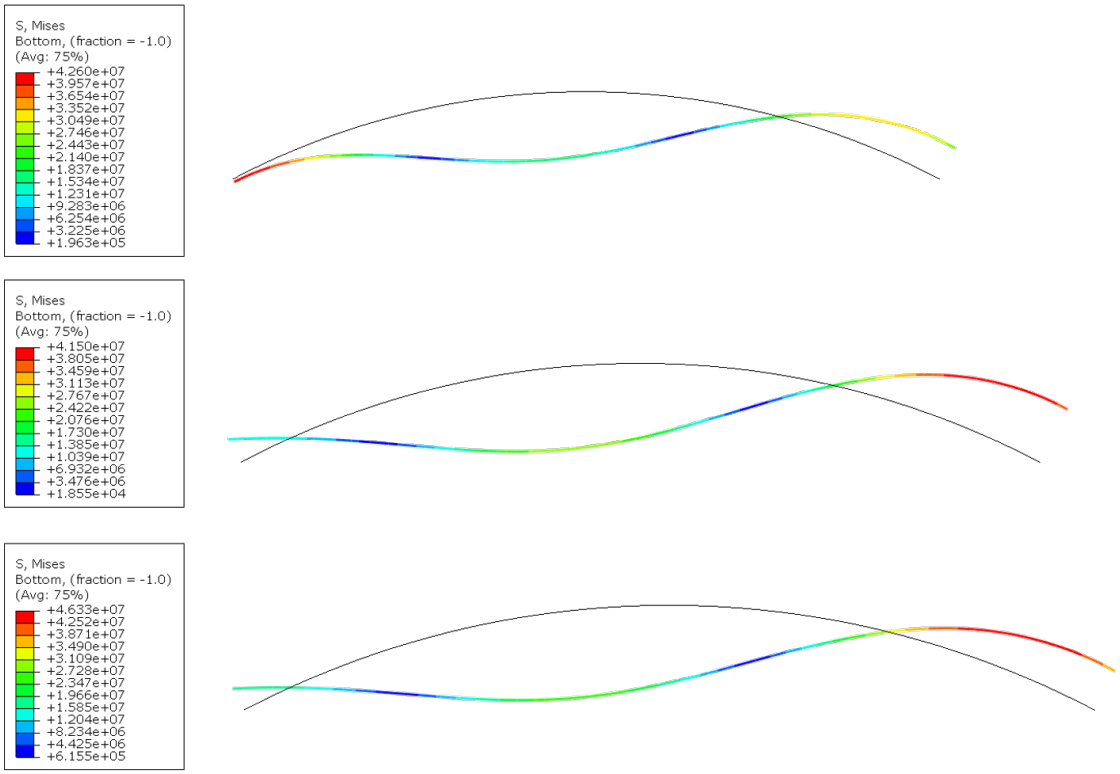

Figure 61: Modified ROM Stress Comparison, Original (top), Modified (mid), Modified with New Load (bot)

It may be worth exploring using different values for the material elastic modulus. The results from the mechanical testing and the corresponding models will show that the material properties of the printed celestial are not so clear.

3.4. Mechanical Testing Results

The mechanical testing of the full celestial frame was done as a uniaxial quasi-static compression under displacement control at a rate of 1 mm/min. Two specimens were tested with overall diameter of 203.2 mm and a beam radius of 2.64 mm. The specimens were loaded in along the vertical axis in compression until fracture occurred. In both

cases the structure began to collapse prior to the actual fracture occurring. This collapse was indicated by a drop in the load required to continue pushing on the specimen. This was preceded by a significant nonlinear behavior demonstrated by the structure. Two specimen were tested under the same test conditions, but at different orientations to their print orientations. Specimen 1 was tested in the same orientation as it was printed while specimen 2 was rotated 90 degrees to its print orientation. These orientations are represented in Figure 62 with respect to the build direction.

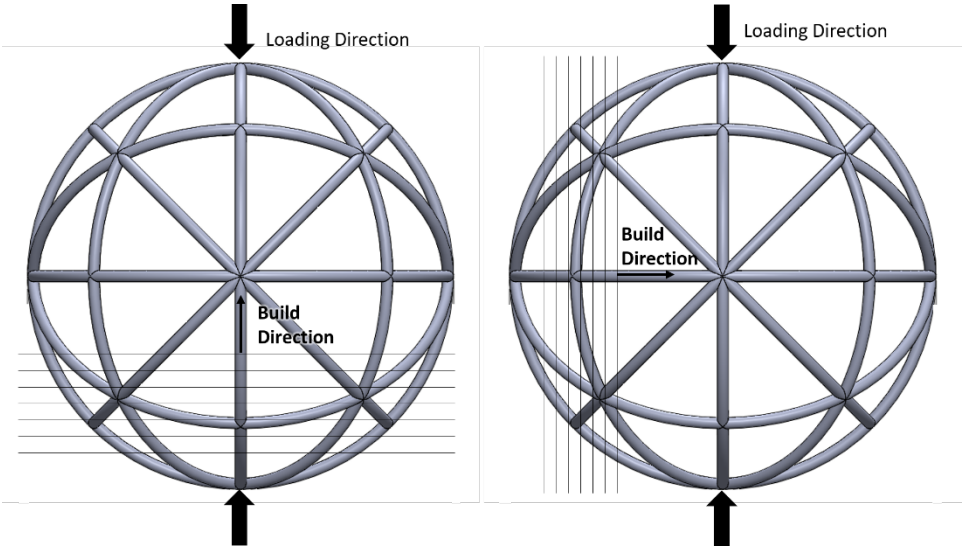

Figure 62: Loading vs Print Orientation, Specimen 1 (left) Specimen 2 (right)

The load-displacement curves produced by the experiments are shown in Figure 63. Close-ups of the curves near the failure point shows that the loads began to drop slightly before the fracture occurred (Figure 64.)

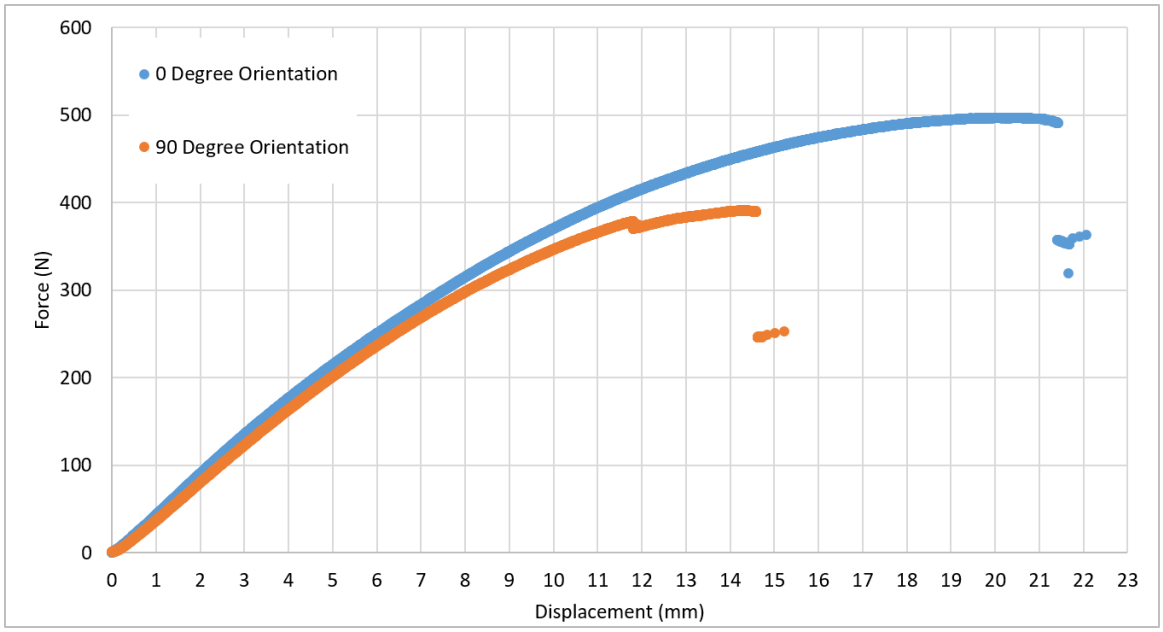

Figure 63: Experimental Data for Two Specimens

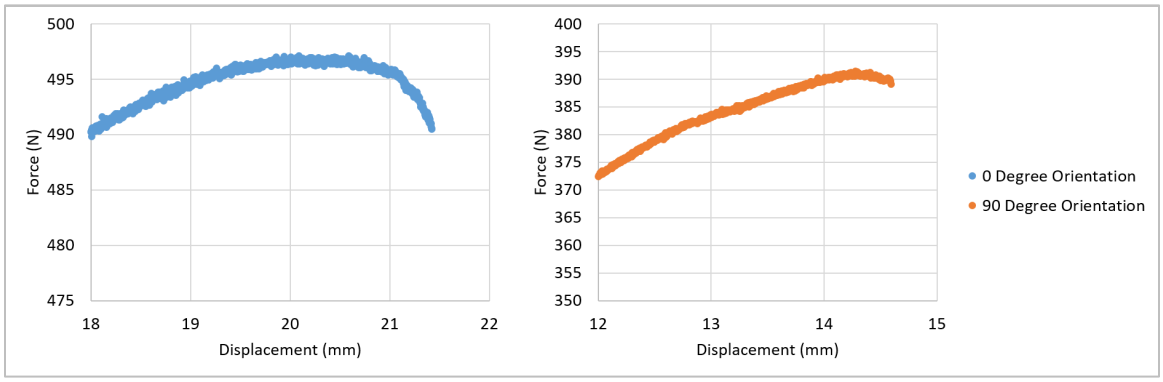

Figure 64: Experimental Data: Close-Up of Experiment Prior to Fracture

The large deformations that occurred are evident in the members of the celestial structure shown in Figure 65. The majority of the displacement for this loading scheme occurred in the top and bottom portions before the 45 degree rings make contact with the primary upright rings. As expected from the modeling, the loading point of the celestial displaced below the level of the flexing members (reference Figure 38). Without the presence of the

loading pucks, these members would have made contact with the loading platen and altered the load application and the support mechanism of the experiment.

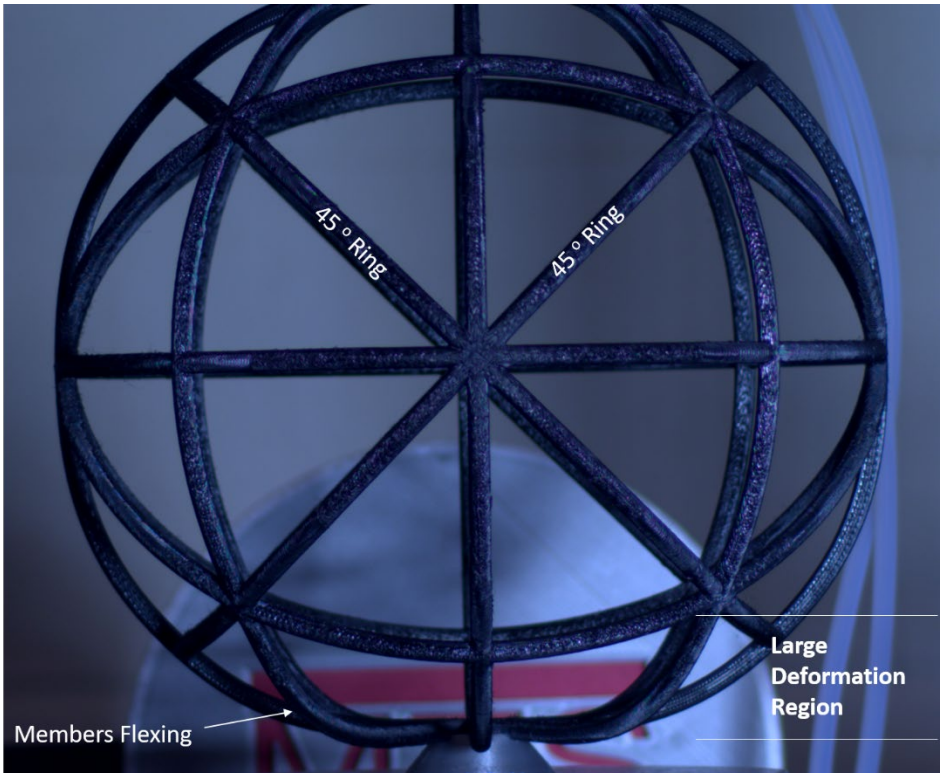

Figure 65: Deformed Specimen 2

The failure locations of the specimen are identified in Figure 66. The fracture of the segment in specimen 1 caused a portion to become removed after it fractured in two locations. Specimen 2 fractured in 2 locations and cracked in several other locations not shown.

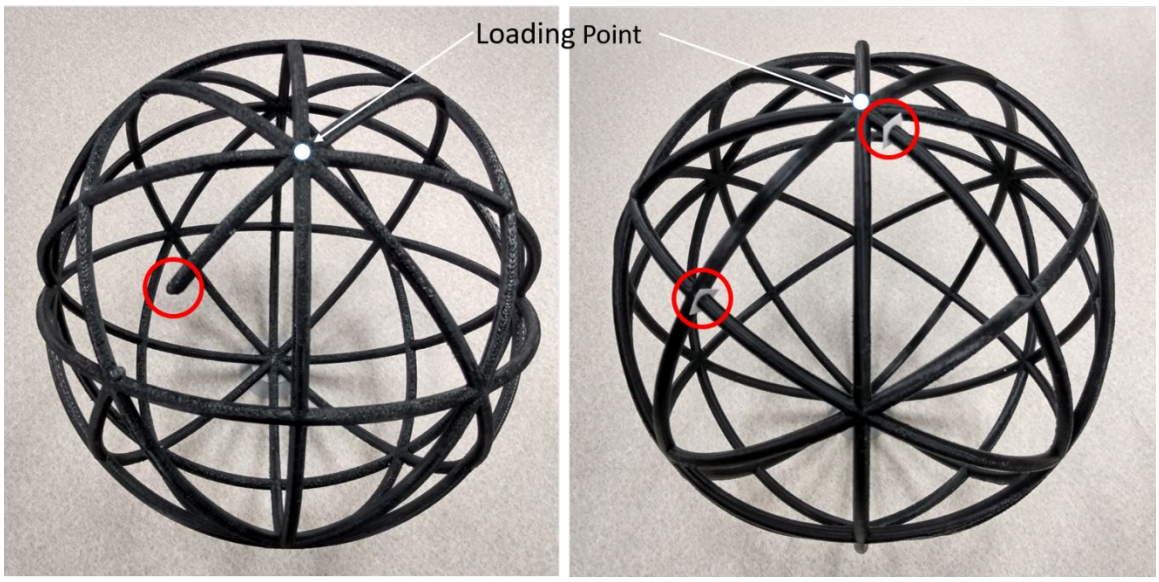

Figure 66: Fracture Locations, Specimen 1 (left) Specimen 2 (right)

In both specimen, the failures propagated between the printed layers; that is, the fracture planes were parallel to the printing planes. This is shown in Figure 67.

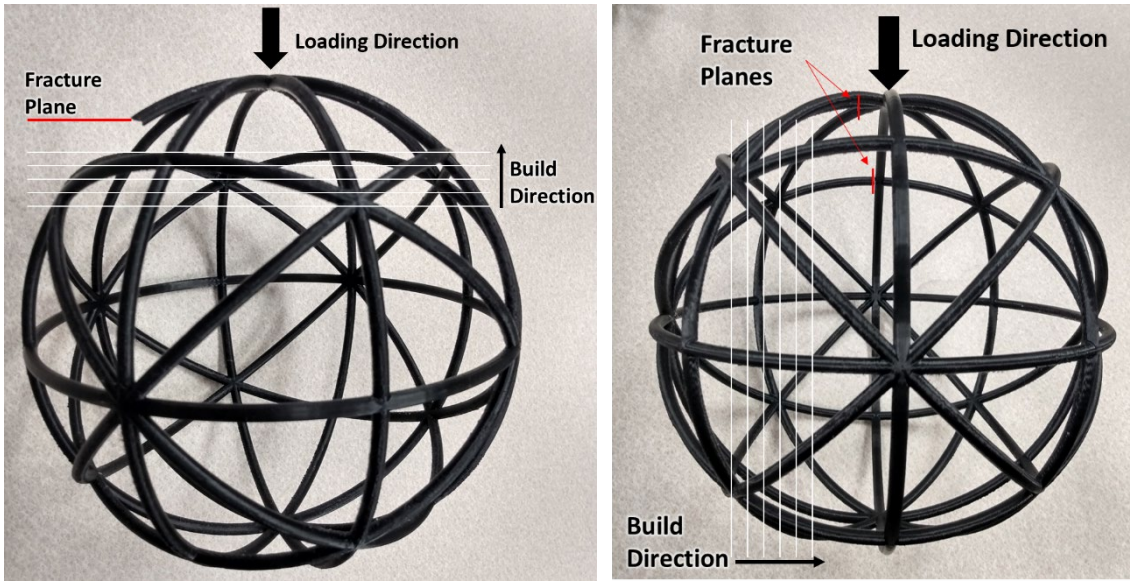

Figure 67: Fracture Planes, Specimen 1 (left) Specimen 2 (right)

In specimen 2 the fractures occurred between two layers printed in the ZX orientation such that the fracture surface was 90 degrees to the beam tangent. The fracture in specimen 1 occurred between print layers that were approximately 45 degrees to the beam tangent. These fracture locations are indicative of the anisotropic material properties, specifically the weaker ZX orientation's maximum stress limit. All fracture locations were dominated by this print orientation.

3.5. Celestial Icosahedron Compression Modeling

Prior to the mechanical testing of the 3-D printed celestial icosahedron, a model of the structure was produced and evaluated to determine the needed testing capabilities and test parameters. This model is discussed in detail in section 2.3.2, but the dimensions were the same and the experimental sample and the modulus used was 2.373 GPa. A load was applied to the model until collapse was observed indicated by the slope of the load displacement curve going to zero as shown in Figure 68. The displacement obtained for this figure was that of the loading point.

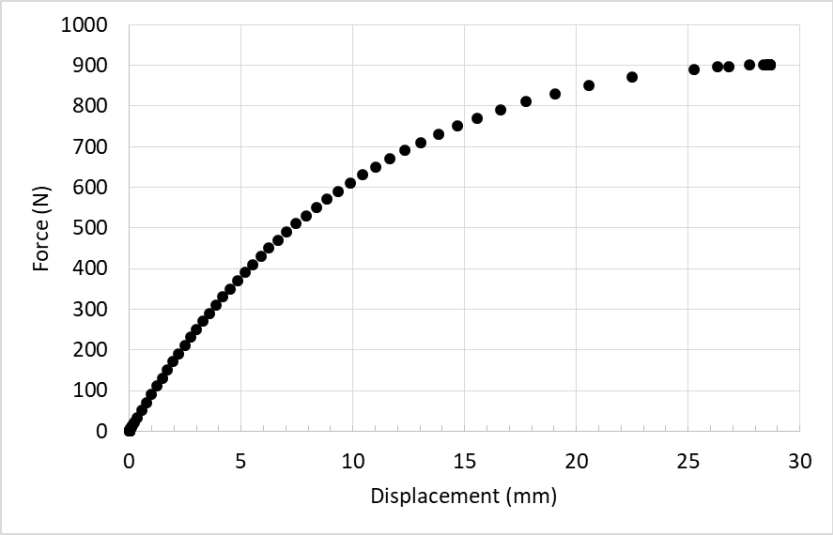

Figure 68: Load-Displacement Curve from Compression Model

The structure was predicted to collapse at a load of approximately 823 N after a displacement of approximately 27.4 mm; however, this did not take any failure criteria such as stress into account. Using the ultimate tensile stress limit of 42 MPa, the first time this tensile stress level was observed exceeding 42 MPa in the member was at a load of 330.5 N after a displacement of 4.67 mm. This location of this stress is near the boundary of the kinematic constraint used to represent the support puck, see Figure 69. If the stress concentration at that location is not as severe as predicted, the next location to inspect is along the midsections of the members where the stress is also rising.

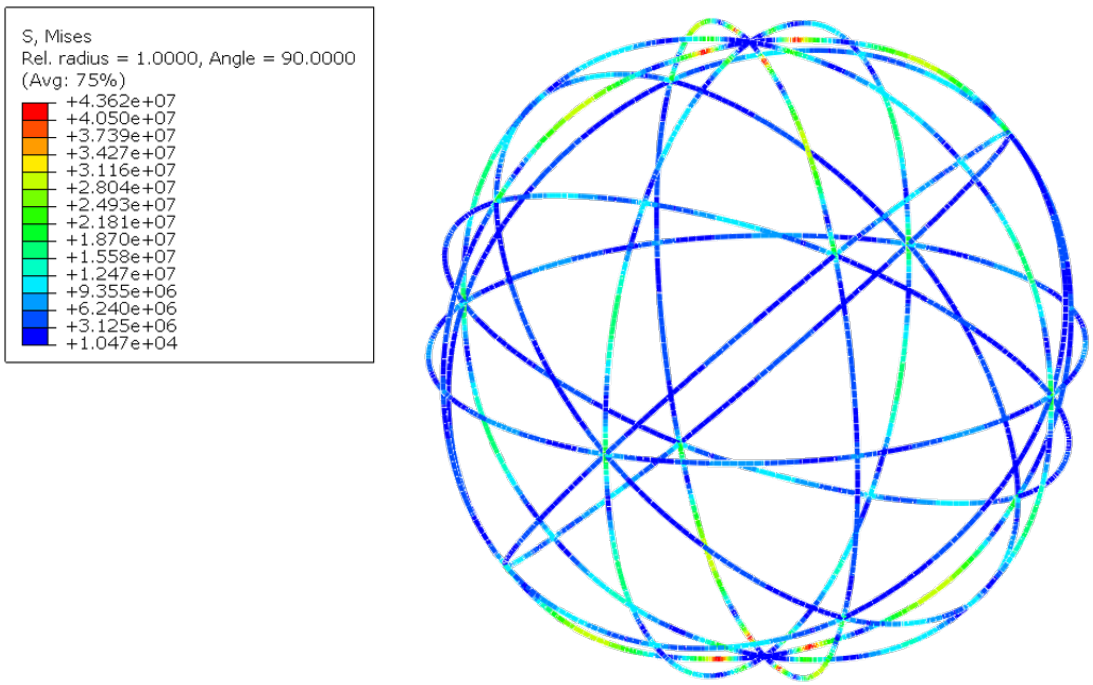

Figure 69: Celestial Under Vertical Compressive Loading to Max Stress

Continuing the analysis until the maximum stress in the members away from the stress concentration reaches 42 MPa produces a maximum load of 530.5 N with a displacement of 9.06 mm. This result is shown in Figure 70 with the stress location circled. This stress occurred in segment A.

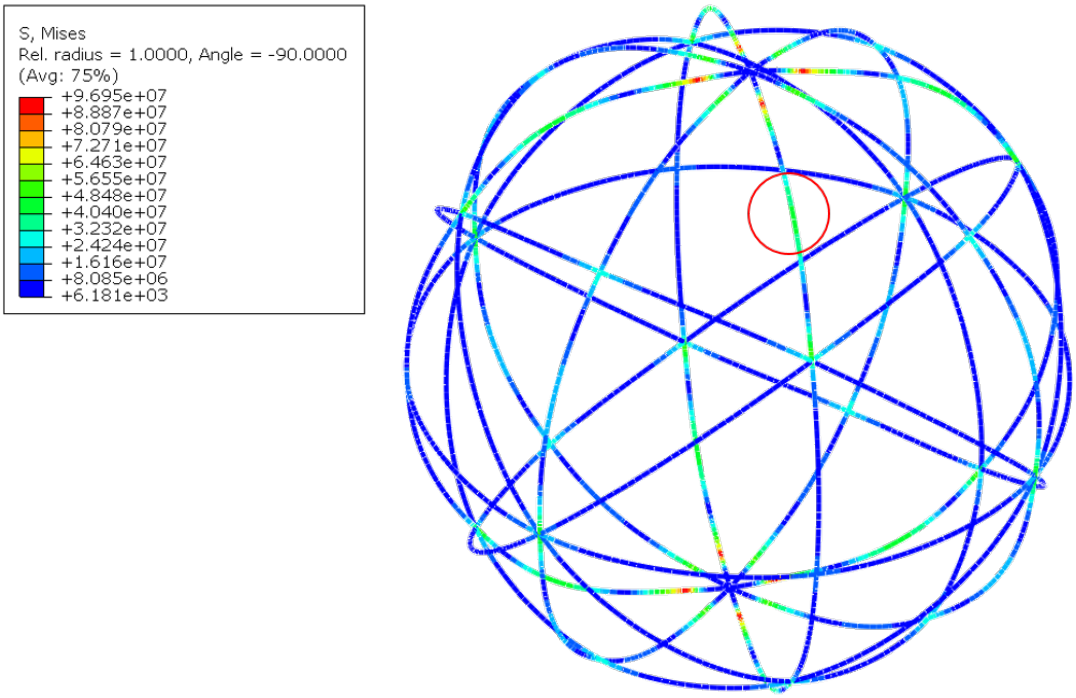

Figure 70: Celestial Under Vertical Compressive Loading to Max Stress in Segment Midsection

3.5.1. Analytical Results Compared to Experimental Results

The results from the experiment were compared to the analytical results from the FEA model with the presumed material modulus of elasticity of 2,373 MPa. A comparison of the force versus displacement curves is shown in Figure 71. The model prediction does not represent the experimental observations. The model prediction has a much steeper slope indicating that the model was much stiffer than the experiments which would indicate that the printed material properties did not match the expected material properties that were used in the model. The model used a modulus of elasticity of 2,373 MPa which was taken from the experiments of Greenoe [14]. These experiments

were of a single ring which demonstrated a high degree of flexibility. Greenoe's results closely correlated to the material's flexural modulus for both material orientations. This was expected since there was a large degree of bending and this was the primary method of load transfer throughout the entire rings for those experiments.

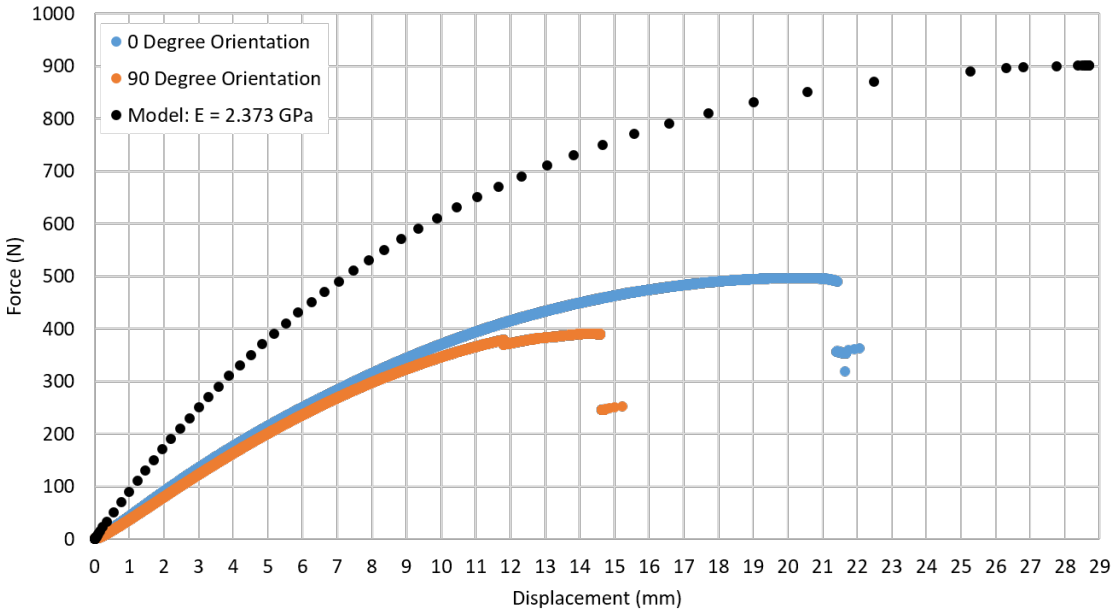

Figure 71: Experimental Results Compared to Original Model

The stiffened spherical shape of the celestial could reasonably be expected to perform more like a tensile specimen placed under compression due to its collectively reinforcing rings which resulted in much more rigid structure with less bending. Additionally, the as printed material properties may not match the manufacturer's specifications. To investigate this a study was found conducted by Travis Shelton et al. that explored the behavior of Ultem 9085 printed samples varying different print parameters [24]. In their baseline experiments, the material properties for samples printed at different orientations were found. These samples were printed under similar printing conditions as the

specimens tested for this research. These material properties are shown in Table 22 for the print orientations depicted in Figure 72.

Table 22: Ultem 9085 Tensile Test Properties [24]

Print Direction	XY	YX	ZX
Ultimate Tensile Strength (MPa)	58.9 ± 1.1	87.1 ± 0.4	44.2 ± 3.3
Yield Stress (MPa)	29.8 ± 0.7	36.6 ± 3.1	28.3 ± 0.5
Elastic Modulus (GPa)	1.03 ± 0.04	1.53 ± 0.29	1.03 ± 0.01

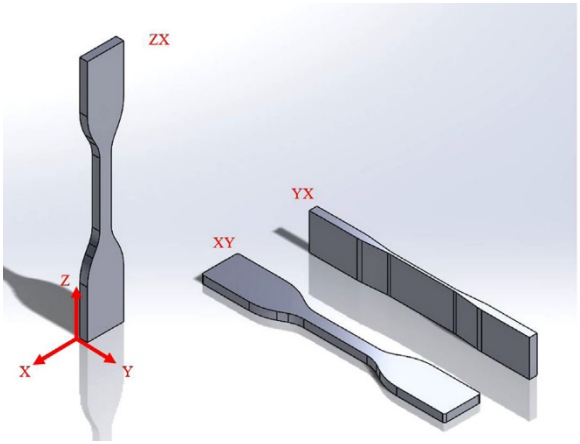

Figure 72: Print Orientations for Shelton's Experiments [24]

The moduli observed in Shelton's experiments were significantly lower than the manufacturer's specification which reports the tensile modulus to be over 2.1 GPa for both the XY and ZX orientations. Furthermore a graduate student from Missouri University of Science and Technology, Krishna Prasanth Motaparti, performed his thesis on the mechanical properties of Ultem 9085 printed through FDM [25]. This research examined printed parts under compression and 3-point bending. Some of the applicable results from those experiments are shown in Table 23.

Table 23: Compressive and Flexural Properties of Ultem 9085 [25]

Orientation	Compressive Properties		Flexural Properties	
	Yield Strength	Modulus	Yield Strength	Modulus
Horizontal	84.3 MPa	833 MPa	64.7 MPa	1875 MPa
Vertical	63.5 MPa	828 MPa	87.1 MPa	2384 MPa

These values found by experimentation were also lower than the manufacturer's reported values. The appropriate material elastic modulus for this application may be a combination of the compressive, flexural, and tensile moduli since all three modes of loading are found within the same structure. A composite modulus was hypothesized to be a rule of mixtures combination based on the percentage of each ring's circumference that was dominated by a specific type of loading. This would enable a single elastic modulus to describe the global material behavior. Examining the deformation pattern of the celestial under compression three regions were identified. These regions can be describe as regions that experience a lot of load-direction displacement that was dominated by a flexural behavior, that did not demonstrate significant displacement and was dominated by compressive behavior, and the equator ring that was dominated by tensile behavior due to the poison's effect. These regions are displayed in Figure 73.

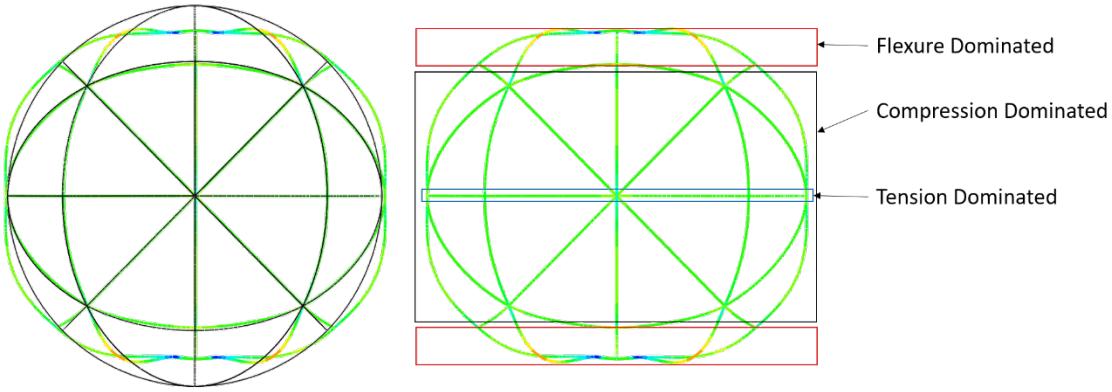

Figure 73: Deformation Regions of Celestial Under Compression

By identifying how much of each ring was part of each region three-dimensionally, a rule of mixtures calculation was done based on these regional behavior assumptions to determine a good elastic modulus that could represent the global material behavior. The breakout for the rule of mixtures calculation is shown in Table 24. The values for the flexural and compressive moduli were taken from the work of Motaparti for the horizontal orientation as this orientation is most predominant within the printed structure. The tensile modulus came from Shelton's work for the YX orientation as this best characterized the print orientation of the equator ring being placed in tension.

Table 24: Rule of Mixtures Breakout for Modulus Determination

# Rings	Flexural % (1875 MPa)	Compressive % (833 MPa)	Tensile % (1530 MPa)	Composite Modulus
2	50	50	0	300.89
2	60	40	0	324.04
4	40	60	0	555.47
1	0	0	100	170.00
Totals	42.22	46.67	11.11	1350.4

The final value for the modulus from the rule of mixtures calculation was 1350 MPa.

The comparison of the analysis with the 1.35 GPa modulus to the experimental results is shown in Figure 74. This load-displacement curve of this model closely represents the experimental results.

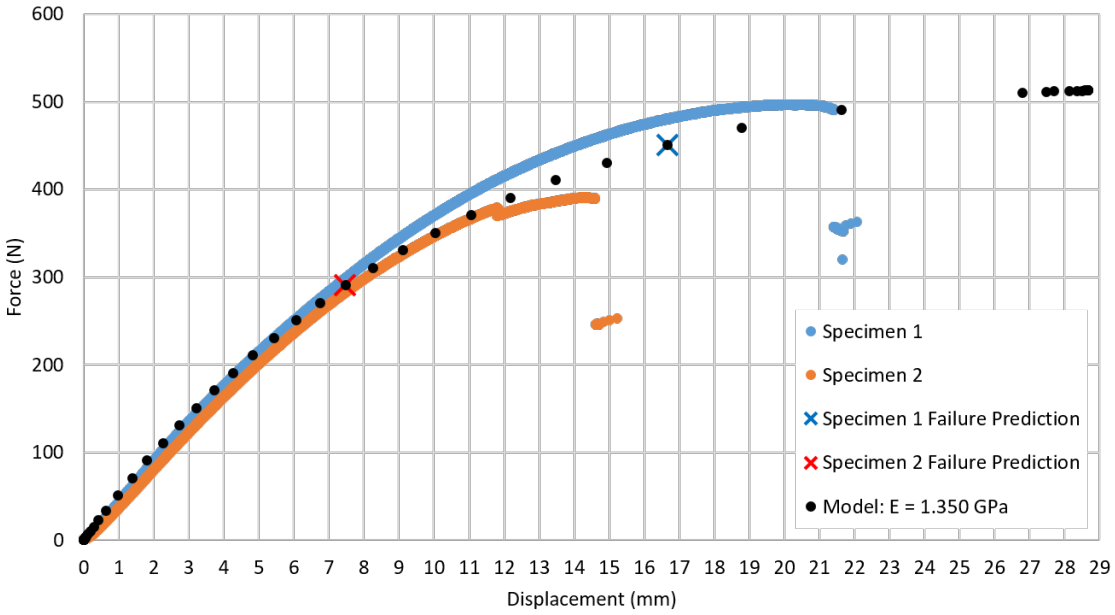

Figure 74: Model and Experimental Force vs Displacement, 1.35 GPa

Previously, the failure criteria was simply assumed to be 42 MPa; however, when comparing the results of the 1.35 GPa model to the experimental results, the anisotropy of the experimental specimen must be considered. Based on the results from Shelton's study the failure stress could be expected to be around either 44, 59, or 87 MPa depending on orientation. The rule of mixtures approach was not used for the maximum stress determination because the individual print orientations for each member could be discretely identified. The modulus property was global and needed to describe the celestial structure behavior as a whole whereas the failure criteria can be applied to

members individually. The first occurrence of a stress above 44 MPa was at a load of 270.5 N. This stress occurred in the failure point A location for specimen 2. Upon examination it was determined that this von-mises stress was located on the compressive side of the bending curve. The tensile side of the bending curve only had a stress of 38.1 MPa at this load. The maximum tensile and compressive stresses as determined by their location on either the outside or inside of the bending curvature was determined by a top or bottom trace of the model geometry. The top trace in this case refers to the outside surface of the sphere while the bottom trace refers to the inside surface of the sphere. This location on specimen 1 had a print orientation closer to the YX orientation which had an ultimate stress of 87.1 MPa while this location on specimen 2 had a print orientation closer to the ZX orientation with an ultimate stress of 44.2 MPa. The load where the tensile stress exceeded 44.2 MPa at this point was found at a load of 290.5 N and a displacement of 7.46 mm. This was relatively close to the failure conditions of specimen 2 during the experiment of 389.1 N at a displacement of 14.6 mm. This stress point is identified in Figure 75 with a tensile stress of 46.0 MPa. The compressive side of the bend at this point was 54.7 MPa. The top and bottom traces of this stress location are shown in Figure 75.

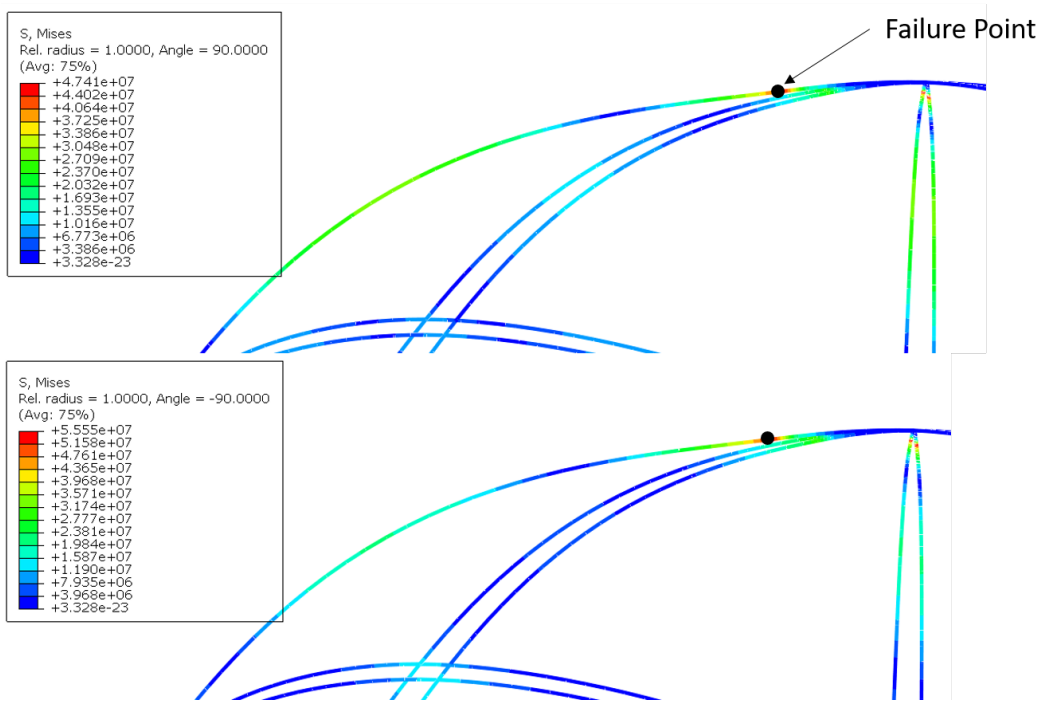

Figure 75: Failure Location for Specimen 2, Top Trace (top) Bottom Trace (bottom)

A tensile stress of 46.7 MPa was found at a load of 450.5 N at the failure location of specimen 1 after a displacement of 16.7 mm. This location has a print orientation that was progressing toward the ZX orientation from the XY orientation. The compressive side of the bend at this point was 59.2 MPa. The top and bottom traces for this load are shown in Figure 76. This load value was also close to the experimental results from specimen 1, a failure load of 490.6 N at a displacement of 21.4 mm.

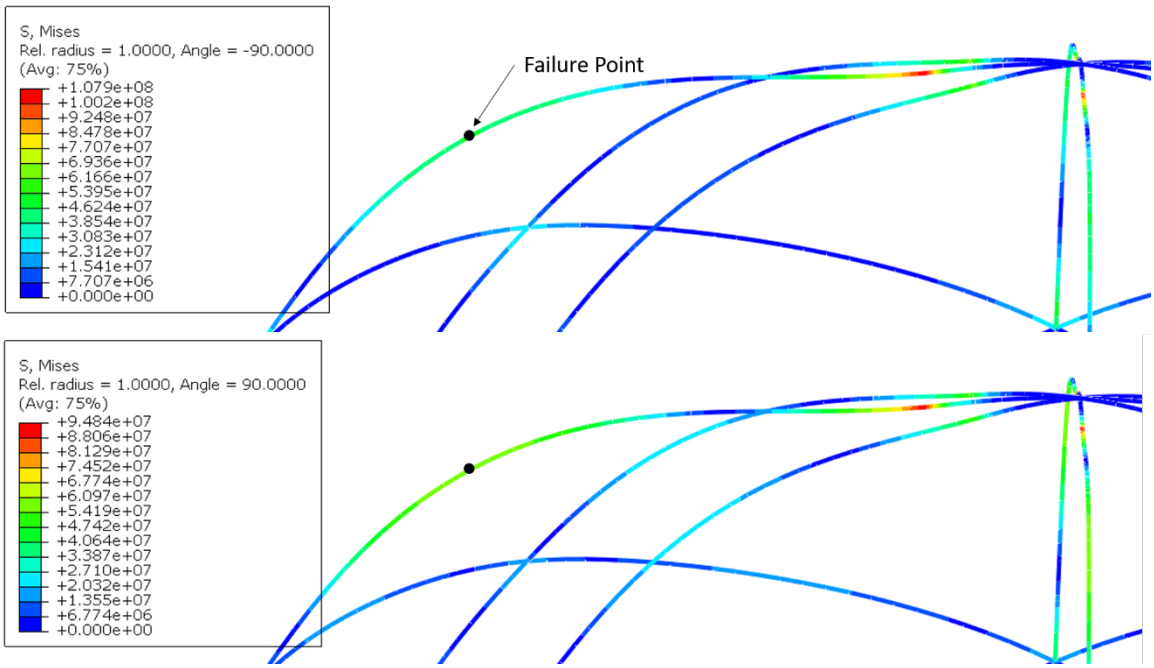

Figure 76: Failure Location for Specimen 1, Top Trace (top) Bottom Trace (bottom)

For specimen 1, the model depicts areas that have a higher stress value than the failure point. This location is near the loading vertex where the failure of specimen 2 occurred. The tensile side of the curve has a stress of 97.8 MPa while the compressive side had a stress of 107.9 MPa. Failure did not occur at this location despite the stress levels above the expected 87 MPa. This could be attributed to two things. This location is near the loading point and could be exhibiting larger stresses than the specimen actually experienced due to the modeling technique. This would mean that the stress observed as the failure stress from the model of specimen 2 was larger than the actual stress level as well. This is beneficial since this would mean that the structure could handle a higher load than the model predicted. The original prediction was almost 100 N lower than the experimental maximum load. This higher load could also mean that the load carrying

capability for this local print orientation is much stronger than anticipated. This is the less likely case since the local print orientation, while close to the YX orientation, is still not as ideal as a perfect YX orientation printed sample. If the load of the model is matched to the load at failure for both specimen, the maximum tensile stress found at the failure location of specimen 1 is 59.5 MPa while the maximum tensile stress was 73.3 MPa at the failure location of specimen 2. The 59.5 MPa correlates closer with the flexural behavior of Motaparti where the flexural yield stress was found to be 64.7 MPa [25]. This analysis highlights how important the failure criteria is when designing such a structure, especially via 3-D printing.

3.5.2. Compression Model with Skin

As alluded to previously, the skin does have an effect on the behavior of the structure may under hydrostatic pressure as observed between the bare frame model and the model with skin which. To further explore the effect of the skin, the skin-on model was placed into compression just like the models representing the experiments. For this case no hydrostatic pressure was applied. The skin used the properties of Mylar with an elastic modulus of 5.001 GPa with a thickness of 0.118 mm. The analysis was run as a dynamic explicit model under displacement control. The displacement rate was chosen to be small such that the total kinetic energy of the model was less than 5% of the total internal, strain, energy. This was determined as a good criteria to consider a dynamic analysis as a quasi-static analysis by Kyongchan Song and John Brewer [26][27][28]. The displacement rate chosen was 5mm/sec to a maximum displacement of 15 mm. The load displacement curve compared to the experimental results is shown in Figure 77. The skin

had a significant effect on both the structure's stiffness and maximum load. The skin allowed the structure to reach a load of 894 N before exhibiting collapse.

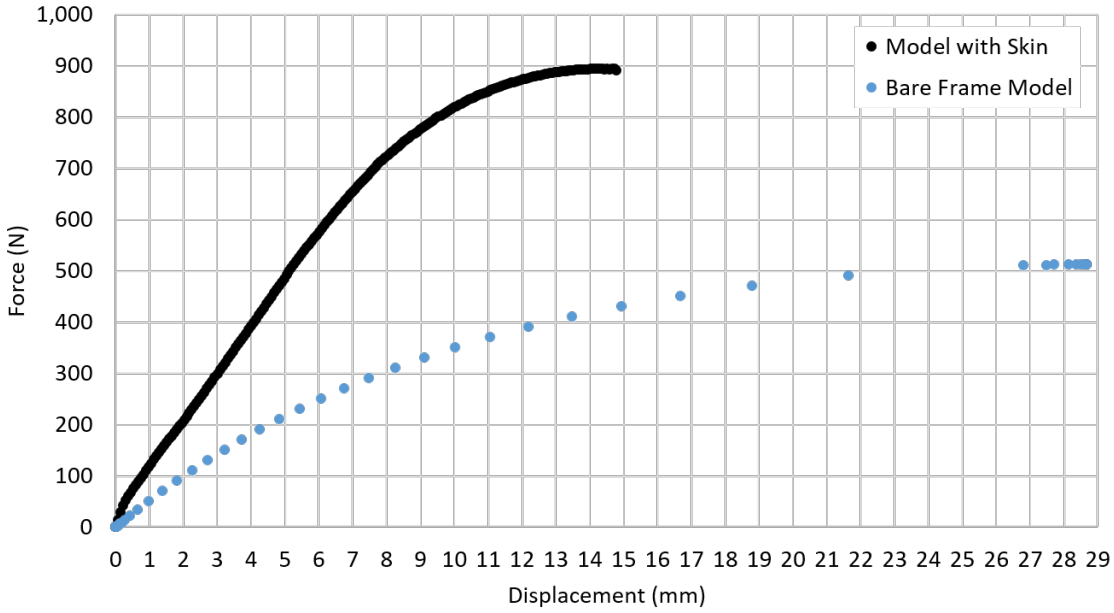

Figure 77: Load Displacement Curve of Frame and Skin, Compressive Loading

The kinetic energy and internal energy are plotted versus displacement in Figure 78. The kinetic energy is always very small compared to the internal energy indicating that the amount of movement compared to the total strain is small indicating a small dynamic response. The largest percentage of the internal energy the kinetic energy ever reaches is 0.34%. This occurs near the end of the analysis when the structure is showing signs of collapse. The parameters selected demonstrate good quasi-static behavior.

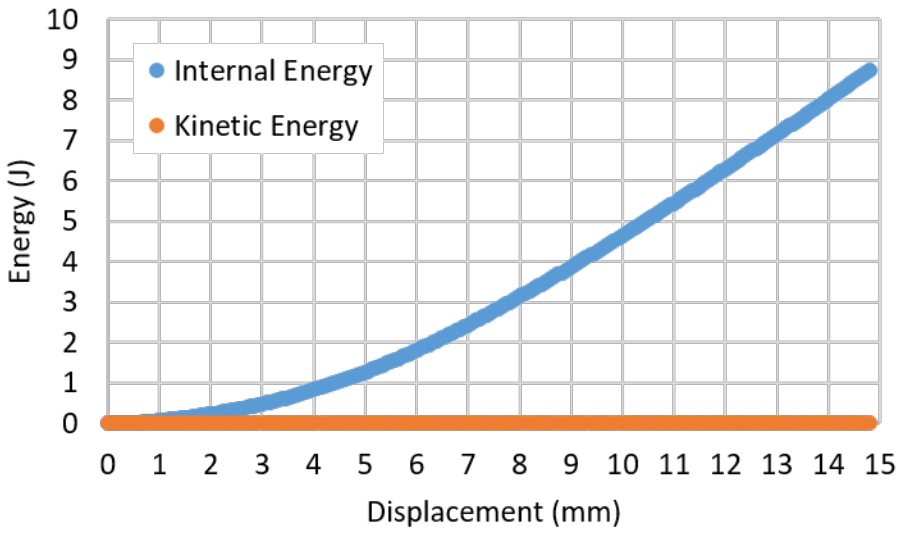

Figure 78: Internal Energy and Kinetic Energy for Quasi-Static Analysis

The stress field at the final step of this analysis is shown in Figure 79 . This result is at a load of 890 N after a displacement of 14.79 mm. The stress field of the frame, shown in the bottom image of Figure 79, represents a top trace of the von Mises stress to capture the tensile side of the bending stress in the midsection of the members where failure occurred in specimen 1. The maximum tensile stress was found to be 35.5 MPa in a B-type segment instead of an A-type segment as previously observed. This stress is well below the ultimate stress limit of 44 MPa [25] for this orientation. The maxium tensil stress near the loading point was found to be 112.4 MPa. This is similar to the 107.9 MPa stress found in this location for bare-frame model under compression representing the load at failure for specimen 1. As discussed in the previous section this stress may be higher than the actual stress due to the loading condition. With that being said the stresses observed in the frame are likely to be supported by the material to this point. The addition of the skin increased the maximum load capability of the structure by

77%. This is likely due to the skin preventing the large bowing behavior of the members in the flexural region of the structure. This resistance is evident by the higher levels of stress in the skin along the midsections of the members in the top portion of the sphere, see Figure 79 top image. Preventing this bowing behavior reduced the bending stresses in the members by transferring the load into the skin.

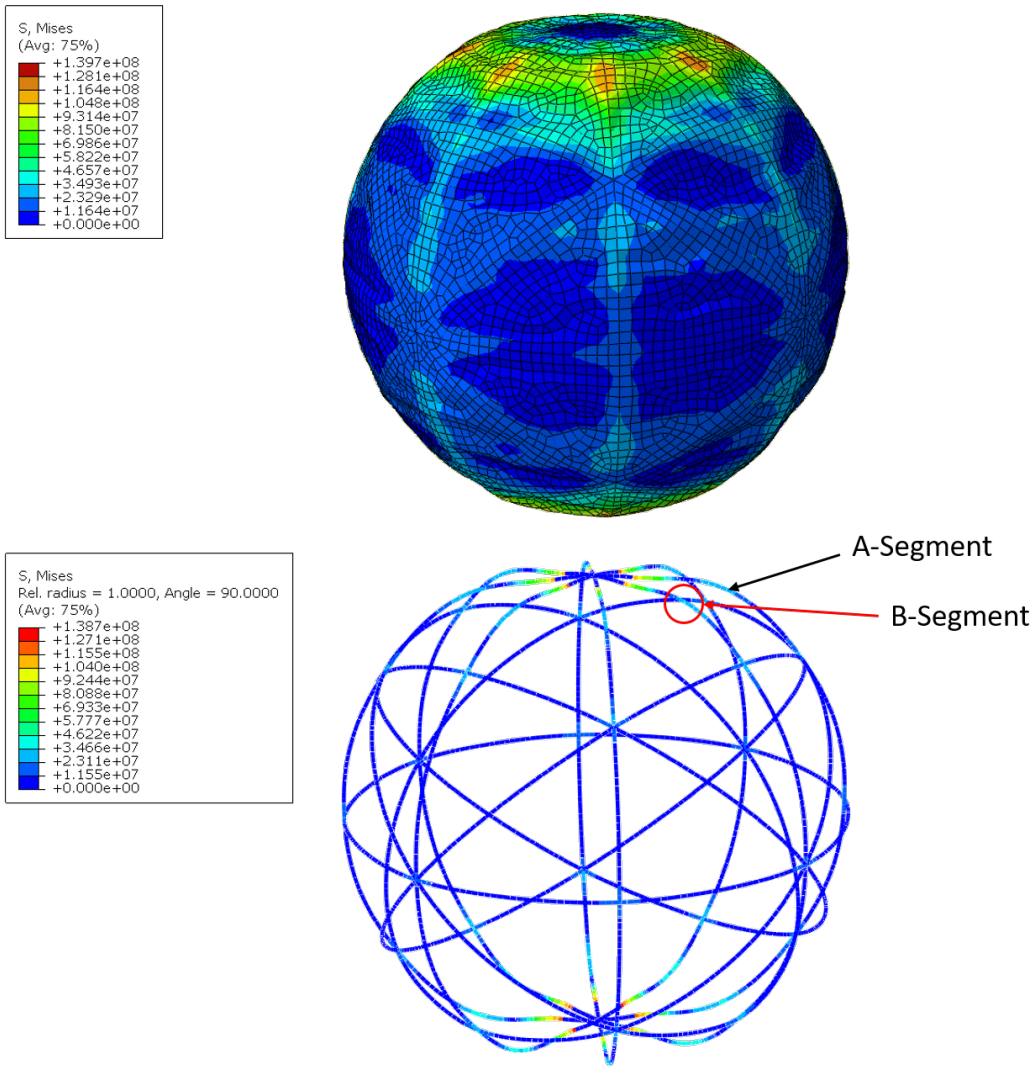

Figure 79: Compression Analysis with Skin, Skin Stress (top) Frame Stress (bot, top trace)

The skin and frame interaction observed for this loading case shows that it is a very important factor to consider. The skin had the effect of reducing the overall frame stresses for this case, but was shown to increase the overall frame stress in the

hydrostatically loaded case. There is no doubt that the presence of the skin affects the behavior of the structure.

3.6. Summary

Several models were analyzed to assess the behavior of the celestial icosahedron under both sea level hydrostatic pressure and vertical compression. The results of the ROM proved to be much lower than bare frame celestial which were also lower than the skin-on celestial model. The ROM was shown to be too stiff with the original boundary conditions. Modifications to the boundary conditions were explored with success in representing the displacement of the member. The lower stress level within the ROM and bare frame celestial could have to do with the missing interaction of the skin which may be playing a significant role in how the celestial behaves. The as-printed material properties were shown to differ significantly from the manufacturer's specifications. The failure criteria used was taken from experiments from other researchers for the same material. Ultimately, the failure stresses in the members undergoing the same deformation mode as the members within the structure is crucial to determining the appropriate failure criteria.

4. Conclusions and Recommendations

4.1. Chapter Overview

This chapter contains the overall findings of the research as they pertain to the goal of developing adequate models to predict the behavior of supporting structure for a VLTAV. The ROM technique that was developed will be discussed; its significance to

future models, and its validity. The conclusions drawn from the experimental testing will also be discussed as it pertains to the complimentary model of the experiment. The future of this project and recommendations for future experimentation will also be discussed.

4.2. Conclusions of Research

It has been shown that the ROM is capable of representing the displacement of the celestial icosahedron members. This process can be repeated for any size celestial with any beam geometry. There still remains a discrepancy between the stress values of the ROM, bare frame celestial model, and the skin-on celestial model, but the values are on the same order of magnitude. Adjustment to the ROM have been demonstrated that this can still be used as a viable option to reduce the analysis effort for designing the celestial members. The load profile used to analyze the individual members is crucial to producing accurate results. Between the methods explored in this research, the best load profile was found using a flexible membrane model of the characteristic triangle. This loading profile produced results that were closest to the skin-on model with a uniformly distributed pressure.

The experimentation has shown that modeling the 3-D printed structure as a homogeneous material can reasonably predict the behavior of the celestial; however, it is crucial that accurate material properties are chosen to represent the behavior of the model. For the load case of vertical compression, a rule of mixtures approach to determine the material's elastic modulus proved effective. The three deformation modes present in the structure were tension, compression, and flexural. Each of these modes was found to dominate the behavior in at least one location within the structure.

4.3. Recommendations for Future Research

Future researchers looking to continue this line of research would find tremendous benefit in experimenting with evacuating the celestial structure. The compression experiments conducted in this experiment highlighted the importance of properly characterizing the material properties and behavior for the given loading scheme. While some information can be taken from the compression experiments and applied to the hydrostatic pressure models, the different loading scheme may cause the structure to behave entirely different. To begin this sort of experimentation a method of applying a membrane over the celestial structure will need to be matured. Next steps would involve searching for available materials and manufacturing methods to get closer to a neutral buoyancy prototype. As the advanced materials such as carbon nanotubes become more and more common, manufacturing methods using these materials may come available that could produce these geodesic shapes.

Appendix A: Vector Summed Nodal Reaction Forces vs Nodal Reaction Force Magnitudes

These plots represent the difference in magnitude of the nodal reaction forces and the portion of that reaction force that is in the radial direction. The force magnitude values are higher than the vector projection values because the original reaction forces are not just in the radial direction and include forces in the tangential direction. The vector projection removes the tangential forces that are assumed to be canceled by symmetrical force from an adjacent face.

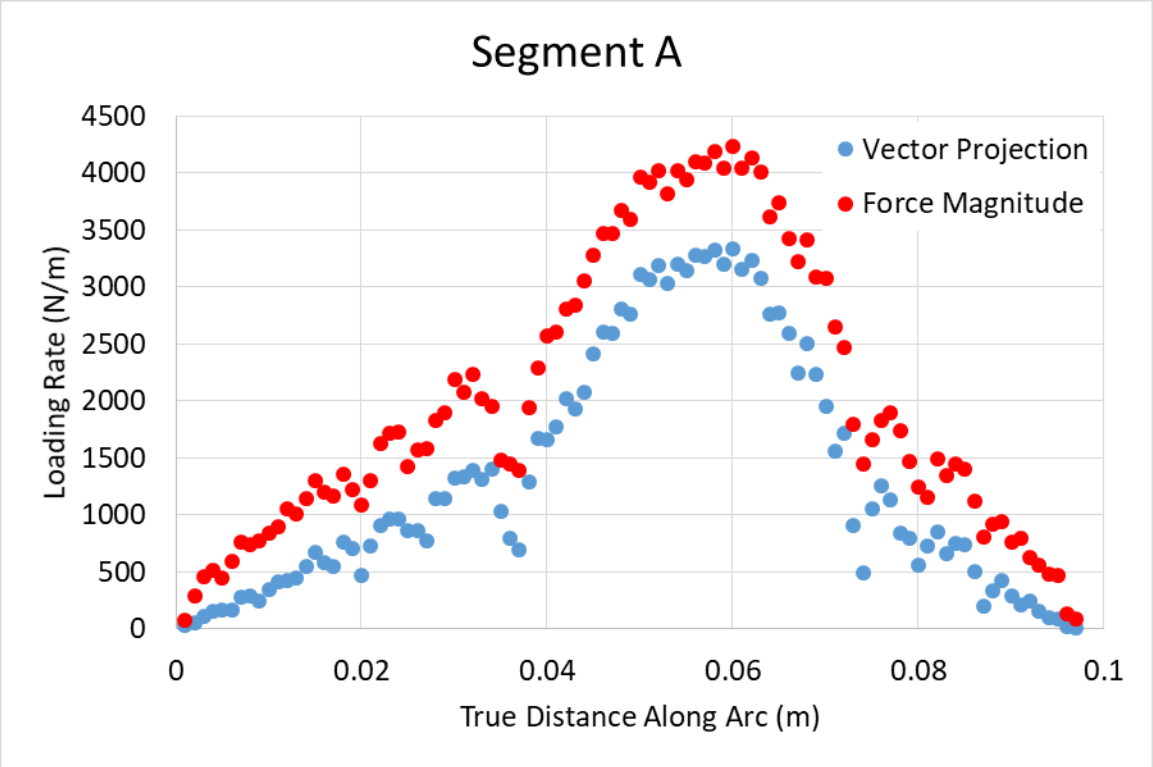

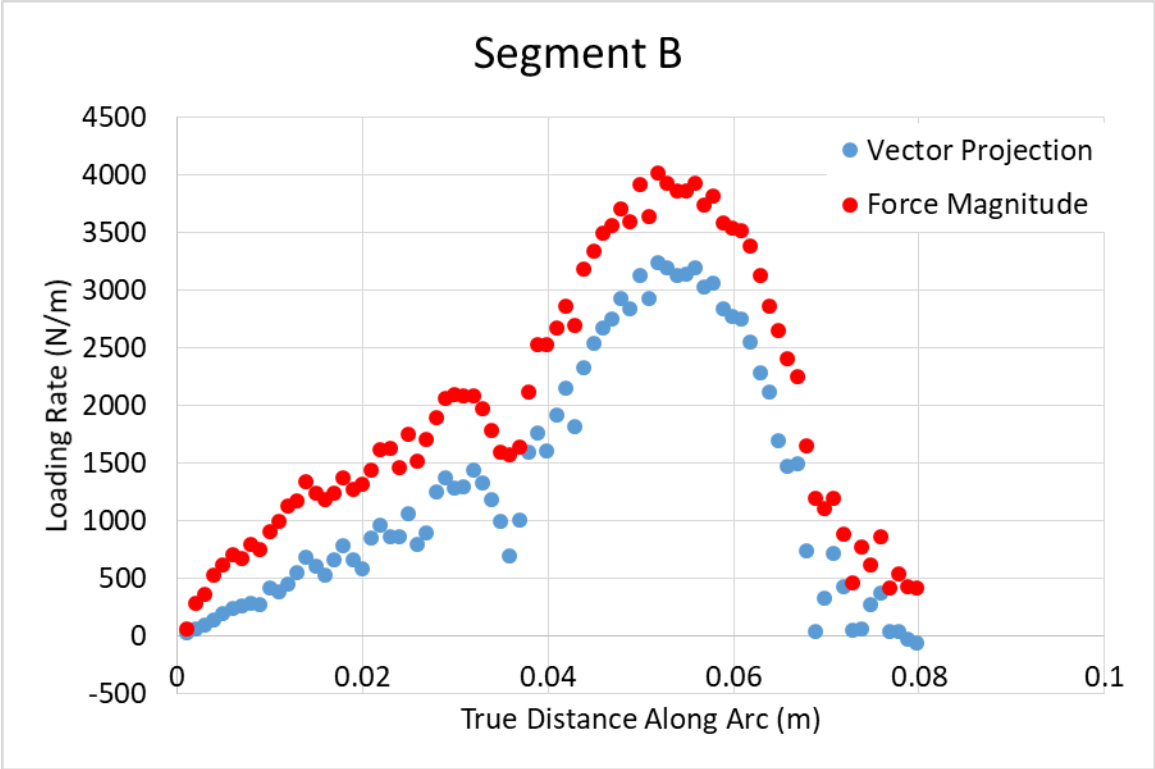
Segment B
Vector Projection
Force Magnitude
Loading Rate (N/m)
True Distance Along Arc (m)
4500
4000
3500
3000
2500
2000
1500
1000
500
0
-500
0
0.02
0.04
0.06
0.08
0.1

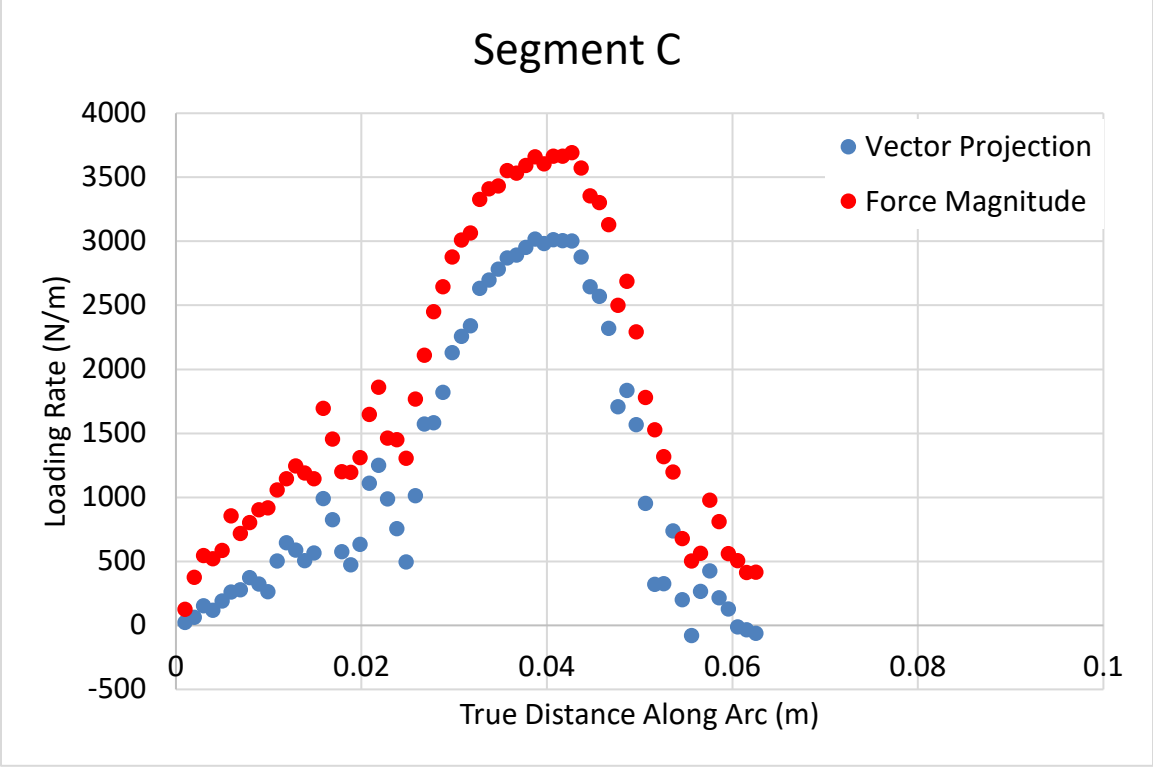
Segment C
Vector Projection
Force Magnitude
Loading Rate (N/m)
True Distance Along Arc (m)
4000
3500
3000
2500
2000
1500
1000
500
0
-500
0
0.02
0.04
0.06
0.08
0.1

Bibliography

1. E. R. Moomey, Technical Feasibility of Loitering Lighter-Than-Air Near-Space Maneuvering Vehicles, Air Force Institute of Technology, 2005.

2. B. C. Cranston. Conceptual Design, Structural Analysis, and Design Space Exploration of a Vacuum Lighter Than Air Vehicle. *AFIT Dissertations*, ENY-16-M, 2016.

3. Helium, 2016 Minerals Yearbook, United States Geological Survey, Feb 2020

4. Helium, Mineral Commodities Summary Annual Publications, United States Geological Survey, 2020

5. D. Noel. Lighter Than Air Craft Using Vacuum. *Correspondence, Speculations in Science and Technology.* Vol 6, No 3, 1983.

6. J. MacDonnell. Francesco Lana-Terzi, S.J."The Father of Aeronautics",[Online]. Available: http://www.faculty.fairfield.edu/jmac/sj/scientists/lana.htm. [Accessed Jan 2021].

7. D. Bushnell, "Buckling of Shells-Pitfall for Designers," AIAA Journal, vol. 19, no. 9, pp. 1183-1226, 1981.

8. A. V. G. Andrey M. Akhmeteli, "Layered Shell Vacuum Balloons". United States of America Patent 11/127,613, 12 May 2005.

9. T. T. Metlen, Design Of A Lighter Than Air Vehicle That Achieves Positive Buoyancy In Air Using A Vacuum, *AFIT Theses,* (ENY-13-J-02), 2013.

10. R. Adorno-Rodriguez, Nonlinear Structural Analysis of an Icosahedron and its Application to Lighter Than Air Vehicles Under Vacuum. *AFIT ,* (ENY-14-M-03), 2014.

11. B. Cranston, M. Alghofaily, and A. Palazotto, Design and Structural Analysis of Unique Structures under an Internal Vacuum. *Aerospace Science and Technology*. Vol 68, pp 68-76, 2017.

12. K. D. Moore, Quasi-Static Nonlinear Analysis of A Celestial Icosahedron Shaped Vacuum Lighter Than Air Vehicle. *AFIT Theses,* (ENY-MS-18-M-280), 2018.

13. D. P. Graves, K. D. Moore, and A. N. Palazotto. Analysis of A Celestial Icosahedron Shaped Vacuum Lighter Than Air Vehicle. *Aerospace Science and Technology.* Vol 95, 2019

14. K. D. Greenoe. Analysis of Additively Manufactured Rings Under Compression Loading for Use in a Vacuum Lighter Than Air Vehicle Structure. *AFIT Theses,* (ENY-MS-20-M-264), 2020.

15. Stratasys. Ultem™ 9085 Resin High-Performance Fused Deposition Modeling Polyetherimide Thermoplastic, 2020. https://www.stratasys.com/materials/search/ultem9085.

16. S. Bhandari and R. Lopez-Anido, Finite Element Analysis of Thermoplastic Polymer Extrusion 3D Printed Material for Mechanical Property Prediction. *Additive Manufacturing.* Vol 22, pp. 187-196, 2018.

17. L.W. Just. Dynamic Response Analysis of an Icosahedron Shaped Lighter Than Air Vehicle. *AFIT Theses,* (216), 2015.

18. Dassault Systems, Abaqus Analysis User's Manual Version 6.6

19. T. J. Ypma. Historical Development of the Newton-Raphson Method. *Society for Industrial Applied Mathematics Review.* Vol 37, No 4, pp. 531-551, Dec 1995.

20. Mylar Polyester Film, Product Information Form, http://usa.dupontteijinfilms.com, Accessed November 2020

21. D. P. Graves. Initial Stage of Fluid-Structure Interaction of a Celestial Icosahedron Shaped Vacuum Lighter Than Air Vehicle. *AFIT Theses*. (ENY-19-M-216), 2019.

22. J. R. Schwemmer, A. Palazotto, and J. Chrissis. Optimal Design of a Hexakis Icosahedron Vacuum-Based Lighter-Than-Air Vehicle. *AIAA Journal*, Vol 56, No. 6, June 2018.

23. W. D. Pilkey, Formulas for Stress, Strain, and Structural Matrices, 2nd ed., Hoboken: John Wiley and Sons, Inc, 2005.

24. T. E. Shelton, Z. A. Willburn, C. R. Hartsfield, G. R. Cobb, J. T. Cerri, and R. A. Kemnitz. Effects of Thermal Process Parameters on Mechanical Interlayer Strength for Additively Manufactured Ultem 9085. *Polymer Testing*, Vol 81, 2020.

25. K. P. Motaparti. Effect of Build Parameters on Mechanical Properties of Ultem 9085 Parts by Fused Deposition Modeling. *Thesis,* Missouri University of S&T, 2016

26. K. Song, F.A. Leone, and C.A. Rose. Analysis of Progressive Damage in Cross-Ply and Quasi-Isotropic Panels Subjected to Quasi-Static Indentation, *Conference Proceeding*, AIAA S&T Forum and Exposition, 8 Jan 2018

27. Abaqus/Explicit: Advanced Topics: Quasi-Static Analyses. 2005

28. J. S. Brewer. Experimental and Computational Analysis of Progressive Failure in Bolted Hybrid Composite Joints, *AFIT Dissertations,* 2020.

REPORT DOCUMENTATION PAGE

Form Approved
OMB No. 0704-0188

1. REPORT DATE *(DD-MM-YYYY)*	2. REPORT TYPE	3. DATES COVERED *(From - To)*
03/25/2021	Master's Thesis	August 2019 - March 2021

4. TITLE AND SUBTITLE
A Reduced Order Model Of The Celestial Icosahedron As The Substructure For A Lighter Than Air Vehicle

5a. CONTRACT NUMBER

5b. GRANT NUMBER

5c. PROGRAM ELEMENT NUMBER

6. AUTHOR(S)
Quick, Torin C., Captain, USAF

5d. PROJECT NUMBER

5e. TASK NUMBER

5f. WORK UNIT NUMBER

7. PERFORMING ORGANIZATION NAME(S) AND ADDRESS(ES)
Air Force Institute of Technology
Graduate School of Engineering and Management (AFIT/EN)
2950 Hobson Way, Building 640
WPAFB OH 45433-7765

8. PERFORMING ORGANIZATION REPORT NUMBER
AFIT-ENY-MS-21-M-314

9. SPONSORING/MONITORING AGENCY NAME(S) AND ADDRESS(ES)
Air Force Office of Scientific Research
875 N Randolph
Ste. 325, Arlington VA
ATTN: Dr. Meir Pachter

10. SPONSOR/MONITOR'S ACRONYM(S)
AFOSR

11. SPONSOR/MONITOR'S REPORT NUMBER(S)

12. DISTRIBUTION/AVAILABILITY STATEMENT
DISTRUBTION STATEMENT A. APPROVED FOR PUBLIC RELEASE; DISTRIBUTION UNLIMITED.

13. SUPPLEMENTARY NOTES
This material is declared a work of the U.S. Government and is not subject to copyright protection in the United States.

14. ABSTRACT
A finite element approach was used to investigate a novel reduced order model to determine the minimum structure dimensionality to support vacuum for a VLTAV. This modeling technique represented the individual segments of the substructure as curved beams with clamped radially-resisted boundary conditions. The full structure was then modeled as a bare structure and structure with skin to validate the results of the reduced order model. The beam geometry for the material Ultem 9085 was determined through this process leading to the 3-D printing of the structure. It was then experimentally tested under uniaxial compression complimented with a FEA model.

15. SUBJECT TERMS
Lighter than air vehicle, vacuum lighter than air vehicle, additive manufacturing, celestial icosahedron

16. SECURITY CLASSIFICATION OF:			17. LIMITATION OF ABSTRACT	18. NUMBER OF PAGES	19a. NAME OF RESPONSIBLE PERSON
a. REPORT	b. ABSTRACT	c. THIS PAGE			Dr. Anthony Palazotto, AFIT/ENY
					19b. TELEPHONE NUMBER *(Include area code)*
U	U	U	UU	145	937-255-6565, ext 4667 anthony.palazotto@afit